



Wissenschaftlich-Technische Berichte
FZR-441 Dezember 2005 ISSN 1437-322X

Anna Lehnert

**Establishment of the Physical and
Technical Prerequisites for the
Determination of the Relative
Biological Effectiveness of
Low-energy Monochromatic X-rays**

Wissenschaftlich-technische Berichte

616

1. Ex.

(2005)441

Z 1666

Zentralbibliothek

04.01.2006 09:11:41

Forschungsberichte

Forschungszentrum Rossendorf / Zentralbibliothek

Eingang:
6/65246



**Forschungszentrum
Rossendorf**

Wissenschaftlich-Technische Berichte
FZR-441
Dezember 2005

Anna Lehnert

**Establishment of the Physical and Technical
Prerequisites for the Determination of the Relative
Biological Effectiveness of Low-energy
Monochromatic X-rays**

Bibliothek FZ Rossendorf



01292268



Forschungszentrum
Rossendorf

**Establishment of the Physical and Technical Prerequisites for the
Determination of the Relative Biological Effectiveness of Low-
energy Monochromatic X-rays**

DISSERTATION

zur Erlangung des akademischen Grades

**Doctor rerum naturalium
(Dr. rer. nat.)**

vorgelegt

**der Fakultät für Mathematik und Naturwissenschaften
der Technischen Universität Dresden**

von

Dipl.-Phys. Anna Lehnert

geboren am 17.01.1975 in Dubna, Russland

Gutachter: Prof. E. Grosse

Prof. W. Dörr

Prof. G. Kraft

Tag der Einreichung: 06.04.2005

Tag der Verteidigung: 24.10.2005

Contents

1 INTRODUCTION	1
2 BASICS.....	3
2.1 INTERACTION OF X-RAYS WITH MATTER AND DOSE DEPOSITION	3
2.2 APPLICATION OF SOFT X-RAYS IN RADIOBIOLOGY AND MEDICINE	4
2.3 POSSIBILITIES OF BUILDING A MONOCHROMATIC PHOTON SOURCE AT ELBE	7
3 A CHANNELING X-RAY SOURCE FOR CELL IRRADIATION	9
3.1 CALCULATION OF ENERGY AND SPATIAL DISTRIBUTION OF CHANNELING RADIATION (CR)	9
3.1.1 Theoretical description of the channeling process	9
3.1.2 Calculation of the relative CR energy and intensity for electron channeling along the (110) plane in diamond.....	12
3.1.3 Population of channeling states.....	14
3.1.4 Consideration of background radiation for electron (110) planar channeling in diamond.....	18
3.2 MONOCHROMATOR DESIGN.....	19
3.3 EXPERIMENTS	24
3.3.1 The experimental setup	24
3.3.2 Measurement of the spectral distribution and intensity of the CR and comparison to the calculation.	27
3.3.3 Extraction of the CR photon flux distribution.....	28
3.3.4 Dose calculation.....	34
4 INVESTIGATION OF A DOSIMETRY SYSTEM FOR EXPERIMENTAL DETERMINATION OF DOSE IN A CELL MONOLAYER.....	37
4.1 PRINCIPLES OF DOSE MEASUREMENT AND APPLICATION TO THIN LAYERS.....	37
4.2 X-RAY DOSE RATE MEASUREMENTS WITH AN IONISATION CHAMBER AND DETERMINATION OF SPECTRAL DOSE DISTRIBUTION	38
4.3 THEORETICAL BASIS OF THERMALLY STIMULATED EXOELECTRON EMISSION (TSEE).....	40
4.4 APPLICATIONS OF TSEE DETECTORS IN DOSIMETRY	41
4.5 EXPERIMENTAL STUDIES	43
4.5.1 Experimental setup and detectors.....	44
4.5.2 Glow curves for the different detector types, reproducibility of detector response and dose range of the TSEE system	47
4.5.3 Dose measurement in a simulated cell environment	54
5 ESTABLISHMENT OF THE BIOLOGICAL ENDPOINTS AND OBJECTS	57
5.1 CELL LINES AND BIOLOGICAL ENDPOINTS	57
5.1.1 Cell culture.....	58
5.1.2 Biological endpoints	59
5.2 PREPARATION FOR IRRADIATION AT THE ELBE X-RAY BEAM	61
5.2.1 Irradiation geometry.....	61
5.2.2 Choice of membrane material	63

5.2.3	Influence of the handling procedure during irradiation on the cell survival and micronucleus test results.....	66
5.3	DESIGN OF THE IRRADIATION SYSTEM AT ELBE.....	69
5.3.1	Cell sample holders	71
5.3.2	A scanning system for irradiation in a non-homogeneous field	72
6	DETERMINATION OF RBE OF SOFT X-RAYS BY X-RAY TUBE IRRADIATION.....	75
6.1	X-RAY TUBES SPECIFICATIONS AND IRRADIATION GEOMETRIES	75
6.2	DETERMINATION OF THE X-RAY SPECTRAL DOSE DISTRIBUTION	76
6.2.1	Measurement of the spectral flux distribution of a soft X-ray tube	76
6.2.2	Calculation of the spectral flux distribution of the reference X-ray tube	79
6.2.3	Spectral dose distributions.....	80
6.3	EXPERIMENTAL RESULTS FOR RBE DETERMINATION	83
6.3.1	Determination of plating efficiency.....	83
6.3.2	Clonogenic survival.....	85
6.3.3	Micronucleus test.....	87
6.4	DISCUSSION	92
7	SUMMARY.....	95
8	APPENDIX	97
9	REFERENCES	99
10	TABLE OF ABBREVIATIONS	107

1 Introduction

A superconducting electron linear accelerator of high brilliance and low emittance (ELBE) is under operation at Forschungszentrum Rossendorf since January 2003. The first stage of ELBE is based on an electron energy of 20 MeV, whereas in the future a 40 MeV beam will be provided. The relativistic electron beam is used to drive various kinds of secondary radiation sources. Among all, X-rays in a wide energy range can be obtained. One method for production of intensive, quasi-monochromatic X-rays in the energy range 10 - 100 keV, tunable in photon energy, is by channeling of relativistic electrons in a perfect crystal. This unconventional photon source with variable time structure will be optimised and used for radiobiological studies. Its first test operation was in October 2003. This thesis is part of the first radiobiological project – the determination of relative biological effectiveness (RBE) of the X-rays in this energy range.

The most important aspects of medical application of low-energy X-rays are imaging and radiation therapy, but they can also be helpful in the study of radiation effects in living matter. However, the RBE depends on the photon energy, dose range, cell line and biological endpoint. Up to now no definitive conclusions can be made about their biological effectiveness due to the large spread of the published data. Therefore, in order to precisely determine the RBE, studies have to be performed at an intensive, tunable photon source, for several practically relevant cell lines and biological endpoints. The possibility of using channeling radiation (CR) for medical applications has been widely discussed in the literature, but building and optimisation of a dedicated source is for the first time performed at the ELBE accelerator.

The presented work is structured in the following way. First, the properties of the X-rays in the context of biomedical applications are described and an overview of their application in radiobiology and medicine is presented (Chapter 2). Then, the CR source has been theoretically characterised in order to estimate its applicability for radiobiological studies (Chapter 3). This includes theoretical calculation of the spectral intensity distribution as well as the spatial distribution of dose over the irradiated cell probe. The results of the comparison of the theoretical predictions with measured data are also presented, together with a method for spectral dose distribution determination. The intrinsic properties of the CR source have led to the conclusion that monochromatisation is necessary. The design and production of the monochromator as well as the results of a simulated spatial distribution after monochromatisation are also described in Chapter 3. The precise determination of dose in a cell monolayer is complicated by the small thickness of the layer and the resulting dose inhomogeneity, especially at low photon energies. Different methods for dose measurement are discussed in Chapter 4. The results of the applicability tests of an unconventional dosimetrical system based on thermally stimulated exoelectron emission (TSEE) are also presented. Due to the RBE dependence on the biological system, careful choice of cell lines and endpoints has to be made. The irradiation at the ELBE accelerator provides specific requirements to the target geometry, radiation shielding and cell environment during irradiation. Experimental tests of cell response to these requirements as well as optimisation of the solutions for the

cell lines and endpoints of choice were performed (Chapter 5). Based on both CR source requirements and the limitations coming from the radiobiological endpoints, a cell irradiation system was designed and constructed, described in Chapter 5. The verification of both the dosimetical and biological methods was performed by X-ray tube irradiations. For the chosen biological endpoints and cell lines, RBE of 10 kV and 25 kV X-rays relative to 200 kV X-rays was determined (Chapter 6). The values obtained show a good agreement with data from other authors and reflect the complex dependence of the effectiveness on photon energy, but also on the cell line and endpoint. Moreover, the results show the importance of further studies of RBE of low-energy photons. In this context, tunable sources of quasi-monochromatic X-rays of medium intensity being more compact and cost-effective than the presently available synchrotron radiation sources are highly desirable.

2 Basics

2.1 Interaction of X-rays with matter and dose deposition

The classification of X-rays depending on their energy is based on their properties and corresponding applications. In order to avoid misunderstanding, the following regions of the X-ray spectrum will be distinguished. As ultrasoft, X-rays in the energy range below 5 keV, with a lower limit given by the ionisation threshold of 10 eV, are specified. This is also the range of high photon absorption, which is not used for medical applications. The range of 5 to 50 keV is referred as soft X-ray range, because of the moderate attenuation in the human body and the corresponding specific application in radiology and radiotherapy. The X-ray range above 50 keV and up to the MeV region will be specified as hard X-ray region. On the other hand, the distinction between X-rays and γ -rays is performed on the base of their origin, because X-rays emerge from the atomic interaction of electrons with matter, whereas γ -radiation originates from nuclear processes, and both cannot be separated due to their energy.

The possible processes of interaction of X-rays with matter include, depending on their energy, scattering (coherent and incoherent), photoeffect, pair production and photonuclear reactions. The last two processes become relevant only at energies higher than about 1 MeV. In low-Z materials (such as water or soft tissue), elastic (coherent) scattering at the atomic shell (Thompson-scattering), plays a role at energies up to about 20 keV. At a higher photon energy, the incoherent (Compton) scattering occurs, resulting in energy transfer to an electron from an outer atomic shell and a change of the photon direction. Another process resulting in energy deposition is the photoeffect, where the photon is absorbed by an inner-shell electron. The vacancy produced in this way is filled by an electron from an outer shell and the resulting energy difference can be emitted as a characteristic photon or induce an Auger cascade. The photoeffect cross section changes with the photon energy as $E^{-7/2}$ and it is, therefore, the main process of energy deposition in the low-energy range. Considering a narrow photon beam of initial flux density φ_0 penetrating a layer of thickness x and density ρ and assuming that the probability of interaction at every point of the layer is equal, the flux density φ after the layer is given by the exponential attenuation law:

$$\varphi = \varphi_0 e^{-\mu_{att}x} \quad (2.1)$$

where μ_{att} is the linear attenuation coefficient, defined as

$$\mu_{att} = \frac{\rho}{Au} \sigma_{tot} \quad (2.2)$$

where σ_{tot} is the total cross section, comprising the probabilities of all interaction processes, A is the relative atomic mass and u is the atomic mass unit. In the practice, the linear mass attenuation coefficient μ_{att}/ρ is used in order to exclude the dependence on the density. In addition, in all processes of photon interaction with matter, it is important to determine the amount of energy actually absorbed. Analogously to the linear mass attenuation coefficient, a mass-energy absorption coefficient μ_{en}/ρ can be introduced:

$$\frac{\mu_{en}}{\rho} = (1 - \eta_{br}) \frac{1}{E\rho} \frac{dE_{kin}}{Ndx} \quad (2.3)$$

where dE_{kin} is the sum of the kinetic energies of all secondary charged particles, E is the energy and N is the number of photons, incident perpendicularly on a layer of thickness dx . For its calculation, the part of energy of the secondary particles, which is lost due to bremsstrahlung η_{br} , has to be known.

For the description of the energy deposition by photon fields, the energy deposition by the secondary charged particles has to be known. An important quantity derived from the mean energy loss dE from all collisions with an energy loss smaller than Δ , which a particle experiences over a track ds , is the linear energy transfer (LET):

$$LET = \left(\frac{dE}{ds} \right)_{\Delta} \quad (2.4)$$

Finally, the energy imparted to a mass element of volume dV and density ρ , is defined as the dose D :

$$D = \frac{1}{\rho} \frac{dE_D}{dV} \quad (2.5)$$

where dE_D is the mean deposited energy in the volume. The biological effect depends not only on the amount of energy, but also on the spatial distribution of the energy released along the track of the ionizing particle. In order to compare radiation qualities, the RBE of a radiation quality x for the effect S has to be introduced:

$$RBE = \frac{D_{ref}}{D_x} \Bigg|_{S_x=S_{ref}} \quad (2.6)$$

where *ref* means reference radiation quality. Usually, as a reference radiation source a heavily filtered high-voltage X-ray tube or a ^{60}Co γ -source is taken.

Generally, the effect of radiation on cell structures increases with increasing LET of the primary or the secondary particles. Moreover, the RBE depends also on the biological system (cells, tissue or organism) and endpoint (e.g. DNA or chromosomal damage, cell kill). Although based on the primary absorption and, therefore, a measurable quantity, the physical dose definition may be insufficient to describe the biological effects.

2.2 Application of soft X-rays in radiobiology and medicine

The investigation of the biological effects of X-rays in the ultrasoft and soft energy range has started before 1930. The importance of X-rays in this energy range in medicine and radiobiology is based on two main aspects: their wide use in clinical practice and their contribution to the understanding of the biological action of ionising radiation. Due to the high attenuation of soft X-rays in the human body, they are used in some special radiology applications, e.g. mammography. Soft X-rays are also used in radiotherapy when the X-ray source can be placed in close vicinity to the tumour. Applications are irradiation of superficial tumours, application of miniature X-ray devices for intravascular irradiation or interstitial radiosurgery, brachytherapy with radioactive seeds and photon activation therapy. Therefore,

the derived information about the biological action of X-rays in this energy range has to be included in the treatment planning calculations in radiotherapy, and, on the other hand, it has to be taken into account for risk estimation in the diagnostic radiology procedures. The importance of ultrasoft and soft X-rays for fundamental radiobiological research is based on the fact, that all ionizing radiations produce a wide spectrum of secondary electrons, mainly responsible for the primary damage at atomic and molecular level to be transformed into an observable radiobiological effect. Ultrasoft X-rays can produce only very low-energy, short range secondary electrons (mainly photo- and Auger-electrons), e.g. the secondary electrons, produced by the characteristic X-rays from carbon (C_K), have an energy of 0.3 keV and ranges in water of less than about 7 nm, comparable to the nucleosome size, which is about 10 nm. This makes the ultrasoft X-rays an useful tool for studying radiobiological models, e.g. the interaction distance between the primary lesions and their connection to the cell structures. On the other hand, based on an analytical model [Bur57] as well as on Monte Carlo calculations [Nik91], it has been shown that a substantial portion of the total dose of any radiation is deposited by the low-energy secondary electrons of the slowing-down spectrum. Electrons of energy from about 0.1 up to 5 keV account for at least one-third of the dose imparted by hard X-rays or γ -rays [Nik87]. Therefore, by variation of the primary soft X-ray energy, a variation in the secondary electron spectra and, correspondingly, in the local energy, is provided.

Up to now, several ways for production of X-rays are known, the oldest and most common being the X-ray tube. Due to the superposition of bremsstrahlung and characteristic X-rays of the bombarded target, a polychromatic photon spectrum is generated, strongly dependent on the anode material. Recently, synchrotron radiation sources have become available, which are also polychromatic, but due to their high brightness, a sufficiently high photon flux is obtained after monochromatisation.

In some cases, the use of a monochromatic soft X-ray source brings reasonable advantages. A specific application of soft X-rays is mammography, which is today the most important diagnostic method for detection of breast cancer at an early stage. The homogeneity of the soft tissue would not produce sufficient contrast if hard X-rays would be applied. A dedicated facility for mammography is a specially designed X-ray tube, operated at 25 - 35 kV with a corresponding beam filtration. Variation of the tube voltage, target material and filtration is necessary to achieve a high ratio of the intensity transmitted through one part of the object to that transmitted through a more absorbing adjacent tissue. This is especially important because of the small differences in the attenuation coefficients of normal and pathologic structures. Most commonly used are X-ray tubes with Mo anode and Mo filter. This allows a rather small energy spread to be obtained due to the Mo characteristic lines (K_α : 17.4 keV, K_β : 19.6 keV), but there are still bremsstrahlung photons of higher energy which contribute to the diffuse coherent and incoherent scattering image background and low-energy X-rays which bring little diagnostic information, but contribute to the absorbed dose. Calculation of the optimal mammographic spectra which could give the highest signal to noise ratio and the lowest dose have been performed [Boo94]. The experiments prove that no universal solution exists, but a substantial reduction of the patient exposure can be achieved by an appropriate target-filter combination, e.g. Mo anode - Mo filter

for thin, W anode - Pd filter for thick breasts [Jen81]. The experiments with synchrotron radiation have confirmed that a monochromatic beam in the energy range 14 - 20 keV results in a higher image quality of the mammographic images [Bur95]. There have been several investigations to produce narrow-band and tunable X-ray beams using Compton backscattering of FEL light [Car90], monochromatisation of an X-ray tube beam via mosaic crystal [Gam95] or multilayer mirrors [Nel87]. An improvement of the image quality is achieved by using digital detectors [Yaf97] or introducing the diffraction-enhanced imaging technique with synchrotron radiation [Pis00] or X-ray tube [Ing98]. However, up to now, there is no monochromatic source available for mammography in the clinical practice.

Another field of soft X-ray application is the digital subtraction imaging. It can be also performed at an X-ray tube, but a tunable monochromatic X-ray source can take advantage of taking two images – one slightly below and one slightly above the K-edge of an element included in the contrast agent, therefore, providing the best possible intrinsic resolution. The usefulness of this technique has been experimentally proven at several synchrotron radiation sources for digital subtraction angiography [Ell00, Ven01] and lung imaging using Xe as a contrast agent [Bay01]. However, the transfer of this technique to the clinical practice seems doubtful until a compact monochromatic source which could be installed in a hospital becomes available.

A quality factor of 1 has been stated for all X-rays independent on their energy in the ICRP Recommendations [ICR91]. However, during the last years, several studies reported an enhanced biological effectiveness after soft X-ray exposure as compared to hard X- or γ -rays.

The biological effects of the ultrasoft X-rays have been studied mainly by using the emitted characteristic X-rays from a target (C_K , Al_K , Ti_K , Cu_L), for which, in various studies, a cold cathode discharge tube has been used [Goo77, Hil98b]. Experiments with monochromatic X-rays at synchrotron facilities [Goo94], as well as studies with Compton backscattered X-rays or laser-plasma X-rays have been performed [Nei89]. In the ultrasoft X-ray energy range, an enhanced biological effectiveness has been observed for C_K , Al_K , and Ti_K ultrasoft X-rays for double-strand breaks (dsb) induction and cell inactivation [Lar01]. For the clonogenic inactivation of various cell lines, as summarised by Goodhead [Goo94], RBE values relative to ^{60}Co γ -rays of up to 5.8 have been obtained. In contrast, RBE values of 1 have been obtained for photons at iso-attenuation energies of 273 and 860 eV, relatively to 250 kVp X-rays [Hil98a]. The difficulty in RBE determination in this energy range lies in the determination of absorbed dose in the cell. Cell morphology, uniformity of the monolayer, intrinsic cellular sensitivity and selective absorption, play a crucial role in the calculation of the attenuation factors.

In the soft X-ray energy range, radiobiological experiments have been performed up to now at X-ray tubes with various targets and filtration as well as at synchrotron radiation sources. Theoretical Monte-Carlo simulations revealed that the RBE of X-rays in the range 1 - 10 keV is in the order of 1.5 for dsb induction in DNA [Mic96], relatively to ^{60}Co γ -rays. Recently, based on primary electron distribution calculations, it was shown that the RBE of mammography X-rays relative to 200 kVp X-rays is not expected to exceed 2 [Kel02]. In various experimental studies on mammalian cells it was shown that soft X-rays have an increased efficiency for clonogenic cell killing [Zei77, Bis86, Hos88, Spa92],

oncogenic transformation [Bre02], micronuclei formation [Ver94] and induction of chromosome aberrations [Vir77, Sas89]. In the study of Zeitz et al., an RBE of 40 kVp X-rays was determined for two different X-ray tubes (Mo target, 0.15 mm Sn filter or W target, the same filter) relative to ^{60}Co γ -rays [Zei77]. For HeLa-S3 cells, the RBE value of 1.3 ± 0.1 was found at 10 % survival level, increasing linearly with decreasing dose rate. In the study of Bistrovic et al. the RBE of 20 kV and 70 kV X-rays with respect to ^{60}Co γ -rays for survival of V79 cells was found to be 1.40 ± 0.07 and 1.19 ± 0.06 respectively, without a significant dose dependence [Bis86]. Spadinger and Palcic reported an RBE of 55 kVp X-rays relative to ^{60}Co γ -rays of 1.0 - 1.4 by using clonogenic survival of V79 and CHO cells as an endpoint [Spa92]. Again, a significantly higher RBE was observed in the low dose range. In a recent study, Frankenberg et al. determined the RBE of 29 kVp X-rays relative to 200 kVp X-rays and obtained for cell kill a value of 1.2 - 2.0 for three cell lines [Fra02]. For micronucleus induction in human lymphocytes by 14 and 50 kVp X-rays relative to ^{60}Co γ -rays, RBE was found to be dose-dependent and the maximum RBE values (RBE_M) of 2.6 ± 0.2 and 1.6 ± 0.2 , respectively, were obtained [Ver94]. Increased efficiency has been also obtained for an encapsulated brachytherapy source ^{125}I (average energy 28.3 keV) [Mar90]. The RBE for survival of human fibroblasts was found to be 1.2 - 1.3 relative to ^{137}Cs -irradiation. In contrast to all X-ray tube irradiations, there have been up to now only two studies of the energy dependence of RBE in this energy range, performed at a synchrotron radiation source. In the study of Sasaki et al. [Sas89], the RBE of monoenergetic X-rays in the range 4.8 - 14.6 keV for dicentric formation in human lymphocytes was found to increase with decreasing photon energy, reaching a maximum at 6.9 keV. This photon energy corresponds to an LET of the photoelectrons and their associated Auger electrons of about $4.21 \text{ keV}/\mu\text{m}$. In this case, the linear component α of the dose-effect curve (see Appendix, Eq. A7) was about 10 times higher compared to ^{60}Co irradiation results. Recently, this photon energy dependence has been confirmed by Krumrey et al. [Kru04] in a study with synchrotron radiation in the range 1.83 to 17.4 keV, who reported for the induction of dicentric chromosomes in human lymphocytes a value of RBE_M at 6.9 keV of 7.70 ± 2.98 .

2.3 Possibilities of building a monochromatic photon source at ELBE

In all radiobiological studies, an important limiting factor is the intensity of the radiation source. The dose range requirement follows from the necessity to reliably distinguish the desired effect above the background and still not enter the saturation region. For most assays, at subcellular up to tissue levels of radiation damage expression, single doses in the range from about 0.1 to about 20 Gy are required. For a reasonable irradiation time in the order of minutes, a dose rate of about 1 Gy/min is required. This states a requirement to the flux of the X-ray source, which for a photon energy of 20 keV at this dose rate, corresponds to a photon flux density of about $10^{10} \text{ ph}/(\text{s cm}^2)$. On the other hand, the wide spread of the data coming from the biological diversity requires a high number of replications and experiment repetitions. Up to now, the most widely used X-ray source providing this dose rate for extensive studies has been the X-ray tube and, in a very small proportion, the synchrotron radiation source. In an X-ray

tube, the photon spectrum consists of polychromatic bremsstrahlung and characteristic lines of the target material. For some radiobiological and medical applications, discussed above, an intensive monochromatic source providing homogeneous irradiation of the target is of advantage. Because of the wide angular spread of the X-ray tube photon flux, the monochromatisation of an X-ray tube would result in either a considerable reduction of the flux or will not be able to provide a homogeneous irradiation. At the synchrotron radiation sources, due to the very high intensity of the beam, after monochromatisation, the photon flux is still sufficient and can be used for homogeneous irradiation of biological probes in the energy range from infrared up to several tens of keV. Although, depending on electron energy, synchrotrons can provide beams with energy of up to about 100 keV, the photon flux decreases strongly with increasing energy and therefore, at energies close to the upper limit they cannot be used as monochromatic sources. Moreover, their use for radiobiological studies is restricted due to cost and logistic reasons.

Another possibility would be the use of naturally quasi-monochromatic X-rays, obtained by channeling of high-energy electrons in an ideal crystal. The spectral width of the CR peak is about 10 %, much larger than the resolution of a standard monochromator. However, the use of a monochromator is always at the cost of intensity loss which is in some radiobiological applications more critical than the spectral resolution. The possible applications of the channeling effect have been widely discussed in the 80-s and 90-s. Its usefulness in medical imaging [Knu94] and in particular for digital subtraction angiography [Gar93] has been considered. The measurements of photon intensity show that such a source can deliver photon flux in the order of 10^{10} ph/(s 10 % bw) for a 5.4 MeV electron channeling in diamond, however, this value depends on the electron current and crystal thickness. Due to the intrinsic collimation and spatial distribution of the channeling radiation, it could be used for homogeneous irradiation of samples of several cm^2 . The improvement of superconducting electron accelerators is directed to the development of an intensive photon source, based on compact “table-top” facilities for extensive use.

3 A channeling X-ray source for cell irradiation

The channeling effect was first discovered in the early nineteen-sixties [Rob62] by computer simulation of ion motion in crystals, although it was predicted already in 1912 by Stark [Sta12]. The basis of the theoretical description was developed by Lindhard [Lin65]. In material research, channeling of ions is a widely used method for defect characterisation in crystals or thin films, but the emitted radiation is usually considered as a side effect and is not characterized. The experimental study of electron and positron channeling was first performed by Uggerhøj [Ugg66]. Channeling radiation (CR) was first observed in an experiment with GeV electrons performed by Frisch et al. [Fri59] and was explained in terms of the coherent bremsstrahlung theory [Dys55, Übe56]. Most experiments on CR from electrons and positrons have been performed in the eighties in several laboratories in the world, in the energy ranges 1 - 10 MeV (University of Aarhus [And83], TU Darmstadt [Gen96]), 10 - 100 MeV (Saclay Linear Accelerator [Gou82], Lawrence Livermore Laboratory [Kle85]), and several hundred MeV up to several GeV (CERN, Kharkov Institute of Physics and Technology, Stanford Linear Accelerator Center, Tomsk Polytechnical Institute, Yerevan Synchrotron), summarized in [Kum89]. The possible applications of the CR have been discussed since its first observation. High current experiments have been performed in Si [Gar90] at a mean current of 9 μA and in diamond at a maximal current of 30 μA [Kle85], showing the feasibility of an intense CR as a continuous source or as a source with picosecond time structure. The theoretical description of the basic theory can be taken from [Bel78]. The study of Gary et al. [Gar91] summarizes the experimental work on various crystals and concludes that diamond, in spite of the low Z , can be considered as an optimal target due to its excellent thermal conductivity and high Debye temperature. Possible areas of application of the CR are in the field of medical imaging for non-invasive digital subtraction angiography [Gar93, Knu94] and mammography [Knu94]. In the presented work, the feasibility of CR for practical application was for the first time theoretically as well as experimentally studied. A source for radiobiological investigations, based on channeling of relativistic electrons in a diamond crystal, has been characterised.

3.1 Calculation of spatial energy and intensity distribution of channeling radiation (CR)

3.1.1 Theoretical description of channeling process

All radiation phenomena are connected to the deflection of a charged particle upon penetration into a target. In the case of random positions of the target atoms, the particle undergoes incoherent multiple scattering and ordinary bremsstrahlung is emitted. The channeling process appears when a charged particle is incident on a single crystal at a very small angle relative to an atomic chain or plane. The interaction potential can be presented as a superposition of the atomic potentials. When the particle velocity component parallel to the atomic strings is relativistic, the crystal appears Lorentz-contracted in the rest frame of the particle. Therefore, the single atoms seem to merge into strings or planes and the potential of the Coulomb interaction with the positively charged atomic lattice may be assumed

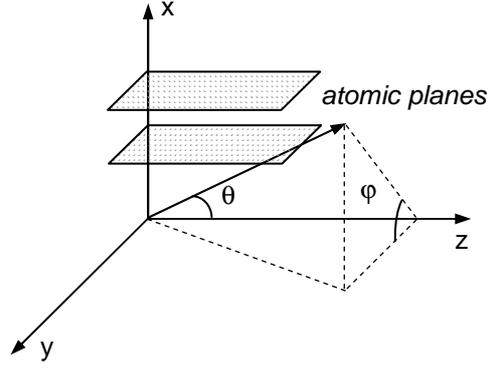


Fig. 3.1 Geometry of the CR in reference to the crystal planes.

to be continuous. Considering the case of planar channeling, where the charged particle is moving along the z direction, the crystal appears as homogeneously charged planes (parallel to the (y, z) plane, see Fig. 3.1), and the potential V depends only on the x -coordinate and is obtained by integration of the atomic potentials V_{atom} of the crystal lattice:

$$V(x) = 2\pi N_v d_p \int_0^{\infty} V_{atom}(\sqrt{r^2 + x^2}) r dr \quad (3.1)$$

where N_v is the atomic density, d_p is the interplanar distance. For the interaction potential between an ion with charge $Z_1 e$ and a nucleus with charge $Z_2 e$ at a distance R , the Lindhard approximation, which accounts for the screening of the nuclear charge by the electrons, can be applied:

$$V_{atom}(R) = \frac{Z_1 Z_2 e^2}{R} \left[1 - \left(1 + (Ca/R)^2 \right)^{-1/2} \right] \quad (3.2)$$

Here $C = \sqrt{3}$ and a is the screening parameter $a = 0.8853 a_0 (Z_1^{1/2} + Z_2^{1/2})^{-2/3}$, a_0 being the Bohr radius equal to 0.529 Å. After integration, the standard plane potential is obtained:

$$V(x) = 2\pi Z_1 Z_2 e^2 N_v d_p \left(\sqrt{x^2 + C^2 a^2} - |x| \right) \quad (3.3)$$

Assuming that the incidence angle is small, the transversal energy is:

$$E_x = \frac{pv\varphi_{in}^2}{2} + V_x(x_{in}) \quad (3.4)$$

where v and p are the particle velocity and momentum, correspondingly. In order to be confined in one channel, the particles need to have a transversal energy that is not higher than the depth of the potential well. From Eq. (3.3), this leads to the following expression for the critical angle for channeling:

$$\varphi_c = \sqrt{\frac{2\pi Z_1 Z_2 e^2 N_v d_p C a}{E_{kin}}} \quad (3.5)$$

where E_{kin} is the kinetic energy of the particle. As an example, the CR properties are calculated for electrons with kinetic energy of 15.0 MeV, channeling along the (110) plane in diamond. In this case the critical angle is 1.7 mrad.

In order to describe the particle motion and radiation production, the applicability of the classical and

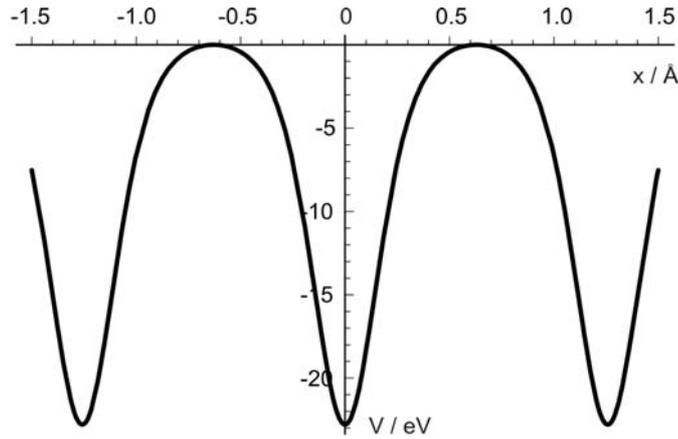


Fig. 3.2 Continuum potential in diamond, (110) plane - the planes are perpendicular both to the page and the abscissa.

quantum-mechanical approaches has to be considered. When high-energy particles are considered, the scattering probability is highly peaked in the forward direction, where the momentum is nearly constant. Therefore, in the case of planar channeling, the motion can be separated into a transverse motion in the (x, y) plane and a longitudinal motion in the z direction. The potential of the closest planes forms a potential well so that for a particle entering the crystal at an angle smaller than φ_c the transverse energy can assume a series of discrete values. If the number of the bound states is much larger than one, a classical description of the particle motion can be used. For the Lindhard potential, this number is [And77]:

$$\xi = 4a_0 \sqrt{N_v d_p \gamma} \quad (3.6)$$

where γ is the Lorentz factor. For the case of channeling of electrons with an energy of 15.0 MeV in diamond along the (110) plane, the number of bound states is about 5. This makes the application of the quantum theory of channeling reasonable in this case. Actually, quantum effects such as the line structure of the emitted radiation for the electron channeling along the main planes in diamond are experimentally observed for energies of up to about 55 MeV [Gou88], although they can be additionally influenced by energy loss and multiple scattering effects. The quantum-mechanical treatment is based on the Bethe theory where, corresponding to the lattice periodicity, the particle wavefunction is considered as a Bloch wave. The crystal potential can be expanded in Fourier series on the reciprocal lattice vector, and the energy states are then calculated in dependence on the Bloch vector. This approach is called many-beam formalism and is useful in understanding the real band structure. However, if the electron energy is higher than about 20 MeV [Wed86], the deep lying transverse energy bands degenerate into levels and the single-well analytical calculations lead to results in good agreement with the observed emission lines. This approach will be used for the further calculations. The wavefunction has to be calculated using the Dirac equation with a three-dimensional periodic potential. In the continuum approximation, the lattice periodicity in the z direction is neglected and the equation can be written separately for the transversal and longitudinal direction. The transverse motion is described by a non-relativistic Schrödinger equation, which in the case of planar channeling is one-dimensional:

$$\left[-\frac{\hbar}{2m\gamma} \frac{d^2}{dx^2} + V(x) \right] \Psi_n(x) = E_{.xn} \Psi_n(x) \quad (3.7)$$

Here n is the number of the bound state in the potential well, with corresponding energy $E_{.xn}$ and wavefunction Ψ_n . This equation is analogous to a non-relativistic case, but the mass m is substituted by the relativistic mass of the electron in the laboratory frame $m\gamma$. One good approximation for the plane potential for electrons, easy to be used in practical calculations, is given by [Kum89]:

$$V(x) = -\frac{U_0}{\cosh^2 bx} \quad (3.8)$$

Here U_0 and b are parameters depending on the crystal. For diamond, $U_0 = -22.8$ eV and $b = 0.215$ Å [Kum89]. The continuum potential in this case is shown in Fig. 3.2. However, for further calculations the simplified approach of a single potential well will be considered, for which the analytical solution of Eq. (3.7) results in the following expression for the energy states:

$$E_{.xn} = -\frac{\hbar^2 b^2}{2m\gamma} \left(-\frac{1}{2} + \sqrt{\frac{1}{4} + \frac{2m\gamma U_0}{\hbar^2 b^2}} - n \right)^2 \quad (3.9)$$

3.1.2 Calculation of the relative CR energy and intensity distribution for electron channeling along the (110) plane in diamond

The emission of radiation by the channeled particle can be calculated using the classical as well as the quantum-mechanical description of the electron motion. The dipole approximation is applicable in the case when the transverse motion in the comoving system remains non-relativistic, or equivalently, when $\varphi_c \gamma \ll 1$ [Bel78]. The distribution of the radiation intensity can be calculated for the transversal oscillatory motion in the rest frame of the electron and then Lorentz-transformed into the laboratory frame. The application of the dipole approximation in the quantum-mechanical treatment of the problem allows to consider only the dipole term of the matrix element. For the case of planar channeling, for the spontaneous radiative transitions from an initial state Ψ_i to the final state Ψ_f , the emitted energy in a solid angle $d\Omega$ and energy interval $d\omega$ is:

$$\frac{d^2 I_{i \rightarrow f}}{d\omega d\Omega} = \frac{e^2}{2\pi c^3} \frac{\omega^2 \omega_{if}^2}{(1 - \beta_{\parallel} \cos \theta)^3} \delta \left(\omega - \frac{\omega_{if}}{1 - \beta_{\parallel} \cos \theta} \right) \left| \langle \Psi_f | x | \Psi_i \rangle \right|^2 \left[(1 - \beta_{\parallel} \cos \theta)^2 - (1 - \beta_{\parallel}^2) \beta_{\parallel} \sin^2 \theta \cos^2 \phi \right] \quad (3.10)$$

where β_{\parallel} is the longitudinal component of the electron velocity v in units of c , θ is the angle between the direction of emission of the photon and the z -axis and ϕ is the polar angle of the photon direction in the (x, y) plane (Fig. 3.1). For the approximated potential of Eq. (3.8), the energy states of the electron in the electron rest frame can be calculated using Eq. (3.9). In this system, the emitted photon energy $\hbar\omega_{if}$ is equal to the difference of the electron energies at the final and initial states. The observed energy of the photon can be obtained from the photon energy in the electron rest frame $\hbar\omega_{if}$ by a transformation into the laboratory frame (Doppler shift):

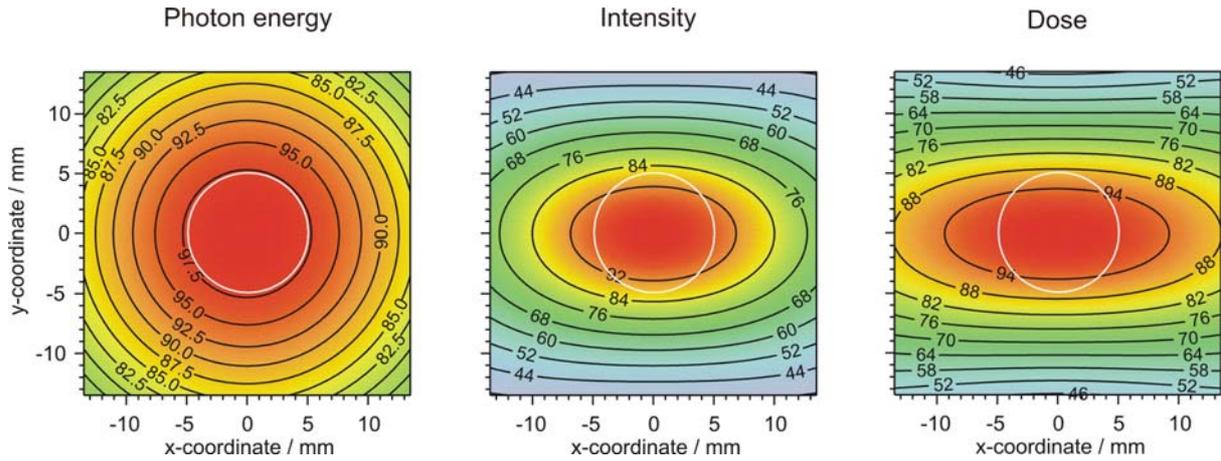


Fig. 3.3 Relative energy, intensity and dose distributions of CR from a 15 MeV electron beam, channeled along the (110) plane in diamond ($1 \rightarrow 0$ transition), at a plane perpendicular to the beam axis, 1 m distance from the source. The white circle of 1 cm diameter represents a reasonable cell target area.

$$E_{if} = \frac{\hbar\omega_{if}}{1 - \beta_{\parallel} \cos \theta} \quad (3.11)$$

The CR parameters, which are important in order to use it as a photon source for radiobiological studies, are the absolute values of the photon intensity and energy, as well as their spatial distribution at the target position. One requirement of the radiobiological assays, which will be discussed in Chapter 5, is the uniform irradiation of the whole target area of several cm^2 . Second, for the investigation of the photon energy dependence of the RBE, an energy spread of less than 10 % over the target area is considered. Diamond was chosen as a source crystal due to the expected high intensity of CR and the appropriate photon energy of 10 - 100 keV from the electron energy range obtainable at ELBE. The spatial relative distributions of energy, calculated according to Eq. (3.11), intensity, calculated according to Eq. (3.10) and the resulting dose in a 10 μm water layer simulating a cell monolayer in the plane perpendicular to the beam axis for 15.0 MeV electrons channeling along the (110) plane in diamond, $1 \rightarrow 0$ transition, are presented in Fig. 3.3. The white circle represents a reasonable target area of 1 cm diameter. As seen from the figure, the intrinsic spatial distributions of CR energy and intensity meet these requirements. In addition, for the discussed radiobiological endpoints, the absolute value of the photon flux and correspondingly, dose rate in the target area, is important. This leads to the necessary estimation of the CR yield. Owing to the symmetry of the potential, the bound states have a defined parity and, therefore, the dipole transitions are allowed only between levels of different parity (the sum of i and f has to be odd). The transitions where $\Delta n = 1$ are the strongest. The matrix elements of the transitions are obtained using the wavefunctions calculated according to Eq. (3.7):

$$\left\langle \Psi_f | x | \Psi_i \right\rangle = \int_{-d_p/2}^{d_p/2} \Psi_f^*(x) x \Psi_i(x) dx \quad (3.12)$$

The wavefunctions of the electron as well as the matrix elements of the transitions have been calculated

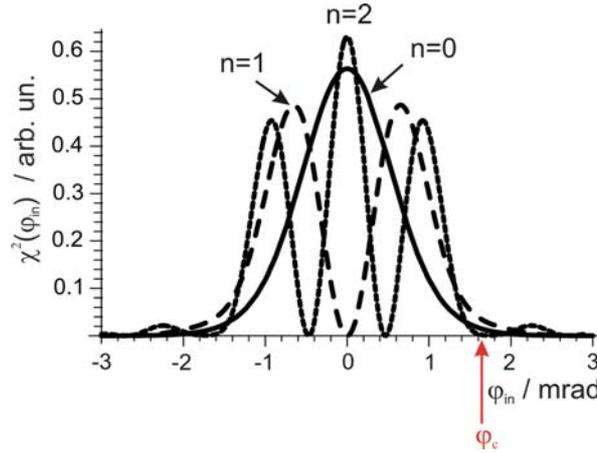


Fig. 3.4 Probability density function for the bound states of the (110) planar potential in diamond at 15.0 MeV electron energy, derived from the momentum distribution. The critical angle for channeling is shown by a red arrow.

numerically using the software Mathematica 4.1 [Wol00]. The δ -distribution in the integration over the frequency ω in Eq. (3.10) results in a simple correspondence between the emitted energy and the intensity at the point of observation, seen also in Fig. 3.3. However, it is only applicable if the instability of the states is neglected. For a more realistic spatial intensity and energy distribution, the finite lifetime of the states has to be considered. It influences the spatial distributions, as well as the absolute CR intensity and, correspondingly, dose, in the cell target. For the discussed radiobiological endpoints, an absorbed dose rate of about 1 Gy/min is desired, which, for a photon energy of 20 keV, corresponds to a photon flux density of about 10^{10} ph/(s cm²). In order to calculate absolute intensities, some assumptions about the population dynamics are necessary.

3.1.3 Population of channeling states

The initial population of the transverse states depends on the entrance angle of the beam and the beam divergence. The probability for an incident electron to be captured into a particular channeling state is proportional to the wavefunction density in the momentum space. The probability density functions $\chi^2(\varphi_{in})$ for the bound states of the (110) planar potential in diamond at electron energy 15.0 MeV have been calculated from the wavefunctions of the states in the momentum representation, and, due to the direct relation of the transversal momentum to the electron incidence angle φ_{in} , are presented in dependence on the incidence angle in Fig. 3.4. The initial population of states depends on the function parity and, moreover, certain states can be selectively populated by controlling the incidence angle. However, this initial population is disturbed already in the first micrometers as the electron propagates into the crystal.

A channeling particle can scatter to a new phase in its original state (intraband scattering), to a new bound state (interband scattering) or to a quasi-free state and thus leave the channel. Whereas the channeling states are formed in the static continuum potential considered up to now, those components of the crystal potential, which fluctuate in space and time, are the reason for the scattering of the

channeling particles. As the longitudinal particle velocity much exceeds the transversal velocity, the scattering can be considered to occur in the transversal plane. However, in the x -direction (see also Fig. 3.1) it takes the form of transitions between the discrete bound states rather than between two states in a continuum. This effect contributes to the redistribution of population in the bands and, therefore, alters the observed transition intensity, but does not change the photon direction or energy. Only the multiple scattering, which is confined to the y -direction, contributes to change in the emitted photon energy due to the Doppler shift.

The incoherent scattering due to thermal displacement of the crystal atoms and the electron scattering can reduce as well as increase the population of a particular bound state. At a penetration depth of several μm into the crystal, the populations of the bound states become equal. A good approximation to the further population of states dependence on the depth d in the crystal is

$$P(d) \propto \exp(-d/l_{occ}) \quad (3.13)$$

where l_{occ} is the distance over which the initial population of the state falls by $1/e$, called occupation length. The occupation length reflects all changes in the channeling regime which result in interband scattering (into other bound or free states). The CR intensity dependence on the crystal thickness d_o for a certain transition becomes

$$I(d_o) \propto 1 - \exp(-d_o/l_{occ}) \quad (3.14)$$

Such a thickness dependence has been experimentally confirmed in the study of Genz et al. [Gen96]. Alternatively, a $d_o^{1/2}$ dependence, resulting from the repopulation of states due to multiple scattering in the crystal, has been assumed by Andersen et al. [And83] and experimentally observed by Reitz for a thick diamond crystal [Rei99]. The multiple scattering of the electron at small angles leads to a repopulation of states and, therefore, influences the intensity of the radiative transitions. A broadening of the emitted CR lines is also observed in this case, increasing with increasing crystal thickness. However, in the study of Kephart et al. [Kep89], no effect of the multiple scattering on the CR spectrum was observed, explained by the fact that the channeling occurs only over the occupation length, which is short enough so that little scattering can occur before the particle is dechanneled. However, in the thickness range below about $100 \mu\text{m}$, the thickness dependence of the occupation length is equally well represented by both models. In order to theoretically estimate the influence of the population dynamics on the CR intensity, one has to know l_{occ} and the initial population of states after reaching the redistribution equilibrium. A scaling law proposed by Andersen et al. [And85] predicts a γ/Z dependence of l_{occ} , which has been proven for diamond in the study of Genz et al. [Gen96], although a weaker dependence has been observed for Si by Kephart et al. [Kep89]. In the present calculations, the occupation length for diamond was extrapolated from the data of Genz et al. [Gen96], assuming a linear dependence of l_{occ} on the electron energy. The initial population of the state $n = 1$ is assumed to be 0.15 which is in agreement with the values calculated by Genz et al. [Gen96]. Under these assumptions, and considering the photon self-absorption in the crystal, the absolute values for the CR photon yield have been calculated according to Eqs. (3.10) and (3.14) for the already discussed potential of Eq. (3.8). A fit

of the calculated γ -dependence of the CR intensity for the $1 \rightarrow 0$ transition at planar channeling along the (110) plane in diamond to a γ^α function resulted in $\alpha = 2.45$. This value is in agreement with the experimental result for the same quantity of Genz et al. [Gen96], who found that the CR intensity scales with the electron energy as $\gamma^{5/2}$. As discussed above, for the approximated potential, the CR energy can be calculated using Eqs. (3.9) and (3.11). The photon energy dependence on γ for the $1 \rightarrow 0$ transition for the electron channeling along (110) plane in diamond has been calculated and interpolated according to the model $E_{ph} = b\gamma^\alpha$, b being a proportionality constant, resulting in a value for the α -parameter of 1.64, close to the value of 1.67, experimentally found by Klein et al. [Kle85] for this transition.

In order to validate the CR intensity and energy calculated using the above model, the available experimental data for the $1 \rightarrow 0$ and $2 \rightarrow 1$ transitions for the (110) electron channeling in diamond are summarised in Table 3.1. The measured energy values for the $1 \rightarrow 0$ and $2 \rightarrow 1$ transitions are shown in the fifth column. The CR energies calculated according to Eqs. (3.9) and (3.11) for the same kinetic electron energies for the corresponding transition are presented in the sixth column. For the CR intensity comparison, the published quantities are given in the seventh column, the corresponding measured values are shown in the eighth column. In order to be able to compare these data to the present calculation, the respective quantity has been derived from Eq. (3.10) and computed for the given energy and transition, under the consideration of population dynamics according to Eq. (3.14) and taking into account photon self-absorption in the crystal. This value is presented in the ninth column. Finally, in order to illustrate the electron energy and transition dependence of the intensity, the differential photon yield per electron and solid angle for a 20 μm crystal has been calculated and shown in the last column. Again, the population dynamics was estimated according to Eq. (3.14) and the self-absorption in the crystal was taken into account. The agreement between the experimentally observed and calculated photon energy is good for the $1 \rightarrow 0$ transition, whereas for the $2 \rightarrow 1$ transition, larger deviations from the experimental values are observed. A possible explanation for this is the shape of the potential, which in the case of higher-order states is not an appropriate approximation because of the band structure. For both transitions, the calculated value of the intensity is larger than the experimental one, probably due to the lack of detailed data for the dynamics of the population of states. After performing the necessary scaling of the presented data, the photon flux for a certain electron current and target position can be obtained. Thus the calculated spatial intensity and energy distribution together with the absolute values completely characterize the CR source. This data can be used in the preparation of the experiments (choice of detectors and detection geometry) and in an estimation of the CR energy and intensity over the entire electron energy range available at ELBE. However, apart from the CR at the target position, the radiation background has to be considered. The various radiation sources contribute to the observed biological effect not only by the absorbed dose, but also according to the biological effectiveness of the radiation quality. This contribution has to be estimated and, if necessary, reduced using a monochromator. For its design, the spatial distributions of CR energy and intensity are also essential.

Table 3.1 Comparison of calculated and published experimental data for electron channeling in diamond (110) for the 1→0 and 2→1 transitions. In the calculated intensity (*) the population dynamics and the self-absorption are considered. Further explanations are given in the text.

Electron energy / MeV	Reference	Crystal thickness / μm	Transition	Observed photon energy / keV	Calculated photon energy / keV	Intensity			Yield (calc.) [*] / ph (sr e ⁻) ⁻¹ for 20 μm
						Quantity	Value (exp.)	Value (calc.) [*]	
5.2	[Gen96]	20	1→0	3.41 ± 0.05	3.04	dN/d Ω / ph (sr e ⁻) ⁻¹	0.0033 ± 0.0003	0.0050	0.0050
9.0	[Gen96]	20	1→0	7.91 ± 0.08	8.12	dN/d Ω / ph (sr e ⁻) ⁻¹	0.0484 ± 0.0057	0.038	0.038
10	[Rei99]	42	1→0	8.95 ± 0.08	9.74	dN/d Ω / ph (sr e ⁻) ⁻¹	0.0224 ± 0.0007	0.084	0.052
16.9	[Kle85]	23	1→0	23.3 ± 0.4	23.7	dN/dt / ph s ⁻¹ 10 % energy interval 100 μA	1.15 x 10 ¹⁰	3.8 x 10 ¹⁰	0.22
			2→1	not observed	12.5	Not observed	-	-	0.11
30.5	[Kle85]	23	1→0	60.1 ± 0.3	62.6	Not reported	-	-	0.94
			2→1	35.3 ± 0.3	42.6	Not reported	-	-	0.85
53.2	[Gou88]	22	1→0	159.0	153.0	dN/(d Ω dz) ₀ / ph (sr μm e ⁻) ⁻¹	0.053	0.17	3.4
			2→1	102.9	118.4		0.037	0.20	4.0
54	[Gou82]	20	1→0	161.8 ± 1.5	156.7	dN/(d Ω dz) ₀ / ph (sr μm e ⁻) ⁻¹	0.037	0.18	3.5
			2→1	104.4 ± 1.5	121.5		0.026	0.22	4.4
54.5	[Kle85]	23	1→0	161.0 ± 0.5	159.0	Not reported	-	-	3.6
			2→1	103.8 ± 0.4	123.5	Not reported	-	-	4.3

Table 3.2 Expected dose in the cell target for radiation from 20 MeV electron channeling along the (110) plane in 100 μm diamond. The cell target is placed at a distance of 1.5 m from the CR source.

Photon energy	Dose / 10^{-16} Gy/e ⁻	
	With 100 μm Be window	With 100 μm Be window and 70 μm Al absorber
1...10 keV background	13.00	0.70
10...100 keV background	1.04	0.86
≥ 100 keV background	0.29	0.29
17 keV CR line (2 \rightarrow 1 transition)	3.23	2.82
29 keV CR line (1 \rightarrow 0 transition)	1.53	1.49

3.1.4 Consideration of background radiation for electron (110) planar channeling in diamond

The unavoidable background radiation in the considered case of high-energy electron channeling at ELBE is mainly bremsstrahlung radiation as well as neutrons produced by (γ , n) reaction in the entire surrounding in the cave. The largest fraction of bremsstrahlung is expected to be produced in the diamond crystal itself and in the beamline elements hit due to the electron scattering in the crystal, as well as in the beam dump. The first part of the bremsstrahlung fraction is unavoidable. In addition, the broad continuum of free-to-bound transitions results in the observation of a wide peak in the spectral distribution at energies higher than the bound-to-bound transitions. The free-to-free transitions (coherent bremsstrahlung) will not be discussed here, since they are mainly observed at large incident angles.

In order to estimate the background dose from the beamline elements after the crystal, Monte Carlo calculations with the packages GEANT and EGS4 were performed [Neu01]. The complete geometry of the beamline was included in the GEANT simulation to obtain a spatial flux distribution of the produced bremsstrahlung photons. This data, together with a detailed irradiation setup, were then used for dose calculation in the target with EGS4, due to the applicability of the code at low photon energies (down to 1 keV) and in thin layers (down to 1 μm). Schematic presentations of the ELBE and the radiation physics (RP) experimental cave are given in Figs. 3.9 and 3.10. The simulation was performed for a 20 MeV collimated electron beam interacting with a 100 μm amorphous carbon target. Energy loss, multiple scattering bremsstrahlung and pair production were considered in all construction materials. Originally, a distance of 123 cm was assumed between the crystal and the centre of the dipole magnet 2 (see Fig. 3.10), which separates the electrons from the X-ray beam. The main contribution to the bremsstrahlung was then found to originate from electrons interacting in the entrance region of the magnet. A reduction of this component down to the level of the unavoidable crystal bremsstrahlung was achieved after reducing this distance to about 80 cm, increasing the beam tube diameter from 40 to

63 mm along with the magnet gap from 60 to 90 mm. The new parameters were then used for the actual beamline construction and for the calculation of the dose in the cell target, positioned 1.5 m away from the CR target. The neutron contribution to the dose in this case was found to be negligible. For the calculation with the EGS4 package of the bremsstrahlung dose in the irradiation setup, the photon beam was assumed first to penetrate a 10 μm cellulose membrane (cell culture dish base), then a 4 μm thick layer with the elemental composition of tissue (the cell monolayer) and finally, a 8 mm thick layer with the elemental composition of tissue (the cell culture medium). The integral doses delivered by the bremsstrahlung background as well as the CR for this setup and electron energy are presented in Table 3.2. The use of an Al absorber in addition to the Be exit window of the beam tube (the situation presented in the right column) results in a significant reduction of the low-energy bremsstrahlung without strongly influencing the CR yield. The absolute values of the CR photon yield have been calculated according to Eq. (3.10), but without consideration of the population dynamics, therefore, the corresponding doses are overestimated. Although the CR intensity in a given energy interval is expected to dominate over the polychromatic background by more than one order of magnitude, the integral dose of bremsstrahlung is comparable to the CR dose. Moreover, the bremsstrahlung produced in the crystal and in the beam tube is emitted in the same direction as CR, which makes simple shielding impossible. For these reasons it was considered necessary to build a monochromator for separation of the desired energy range.

Another source of background radiation in the RP cave is the beam dump. Bremsstrahlung radiation as well as neutrons from (γ , n) reactions are produced as the electron beam is stopped in the material of the beam dump. In order to estimate its contribution to the dose, Monte Carlo simulations with the FLUKA code were performed [Nau02]. For an electron current of 250 μA and an electron energy of 50 MeV, dose rates of 500 Sv/h for photons and 40 Sv/h for neutrons have been calculated at the surface of the beam dump vessel. For consideration of the contribution of the background radiation to the biological effect, additionally the biological effectiveness of the different radiation qualities has to be taken into account. In order to reduce the background equivalent dose rate to a reasonably low contribution of 5 % of the CR, a shielding factor of the order of 10^{-4} - 10^{-3} is necessary at the lowest anticipated dose rate of 0.1 Gy/min. The concrete, conventionally used for shielding, was discarded because a large wall thickness would lead to space problems in the cave. A layered shielding wall of 22 cm Pb and 27 cm polyethylene was designed [Eng03]. The resulting reduction factor of about 10^{-4} for photons and neutrons would bring sufficient background suppression.

3.2 Monochromator design

The standard approach for monochromatisation of X-rays is based on the principle of Bragg reflection in single crystals. This provides a narrow spectral bandwidth of the reflected radiation, however the corresponding narrow angular acceptance yields low integral reflectivity for divergent sources. In order to provide a dose rate high enough for radiobiological studies, the goal was to retain as much as

possible of the CR intensity over the target area. Since a rather large energy spread of up to 10 % is not critical in this case, a mosaic crystal for monochromatisation was chosen. For the energy range of 5 to 30 keV, highly oriented pyrolytic graphite (HOPG) crystals can be used to provide sufficient reflectivity [Bec95]. The bulk material is produced by severe thermal annealing of pyrolytic carbon, and afterwards the HOPG crystals are deposited as thin layers on an appropriate mould surface, which can be planar or bent at any shape. The monochromator geometry was optimised for the Bragg reflection at the (002) plane of the HOPG crystal using a ray-tracing Monte-Carlo software [Bec95]. In the present work, only one monochromator was designed and manufactured. The CR peak from the $1 \rightarrow 0$ transition of the (110) electron planar channeling in diamond was chosen, since it is well separated and has the highest intensity at a given electron energy. For 15.0 MeV electrons, it corresponds to a photon energy of 19.4 keV in the forward direction, which is in the range of interest for the radiobiological research at ELBE. The monochromator geometry, presented in Fig. 3.5, is a result of meeting the Bragg reflection conditions and the requirement of beam focussing at the target position. For the design of the monochromator, knowledge of the CR energy and its spatial distribution is important, together with the spatial distribution of the intensity. The absolute values of the intensity are not necessary for the monochromator geometry calculation. As discussed above, only the multiple scattering could contribute to a change in the angular or spectral distribution of CR, however, this phenomenon has not been studied in detail for channeling particles to be included in the theoretical calculations. An unavoidable source of line broadening is the finite lifetime of the channeling states. It leads to a replacement of the δ -distribution $\delta(\omega - \bar{\omega}_f)$ in Eq. (3.10) by a Lorentzian line shape $\Gamma [2\pi(\omega - \bar{\omega}_f)^2 + \Gamma^2/4]^{-1}$, where Γ is the full width at half maximum (FWHM) of the line. If a finite linewidth is assumed, the unique correspondence between a particular X-ray energy value and spatial coordinates is no longer valid and at every observation point, an X-ray spectral distribution is observed. After substitution of the emission by a Lorentzian line and integration, the spectral distribution is changed, so that the sharp cut-off due to the maximal energy observed in the forward direction is smoothed and photon energy values higher than this cut-off become present in the spectrum. According to [And83a], for the case of a crystal thickness much larger than the coherence length l_{coh} , the following expression for Γ is used:

$$\Gamma = 2\gamma^2 \hbar c / l_{coh} \quad (3.15)$$

where the coherence length reflects only the distance over which the particle is able to radiate undisturbed by scattering (including the intraband scattering where the transversal state is conserved). The coherence length has to be determined for the particular material and channeling regime. In the calculation of the intensity distribution, it was set to $l_{coh} = 1 \mu\text{m}$. This value is in agreement with the value of $0.68 \mu\text{m}$ measured by Genz et al. [Gen96] for the $1 \rightarrow 0$ transition from 9 MeV electron channeling in diamond along the (110) plane and with the stated coherence length of the $n = 1$ state of $4.0 \mu\text{m}$ by Klein et al. [Kle85] at an electron energy of 16.9 MeV. For an electron energy of 15.0 MeV, the intrinsic FWHM becomes $\Gamma = 363 \text{ eV}$. This source of emission line broadening was included in the

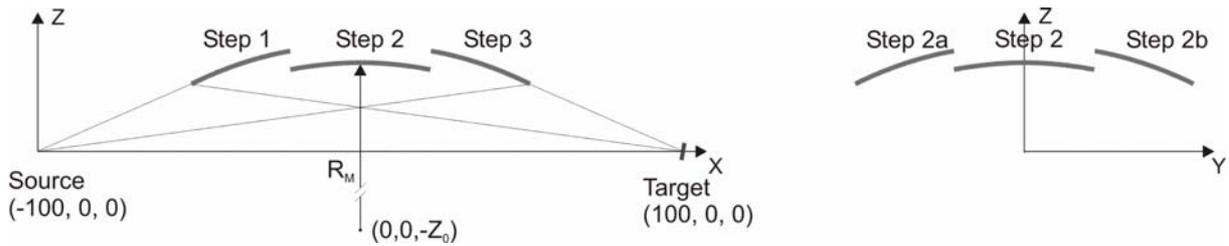


Fig. 3.5 Schematic outline of the monochromator geometry in meridional (left) and sagittal (right) direction.

calculation of the angular distribution of intensity, performed according to Eq. (3.10) and used as input data for the monochromator design.

The major challenge for the monochromator design follows from the spatial distribution of the CR energy. In the electron beam direction, the highest energy is emitted, requiring a smaller Bragg angle than the lower energy values in the outer parts of the CR cone. Additionally, in order to minimize the monochromator surface, it has to be placed at a minimal distance from the CR source. In the RP cave, the minimal possible distance downstream at the electron beam axis after the dipole magnet (see Fig. 3.10) is about 100 cm. Therefore, the setup was designed so that the source is positioned at coordinates (in cm) $x = -100$, $y = 0$, $z = 0$ and the beam axis meets the monochromator at $x = 0$, $y = 0$, $z = R_M - Z_0$, the channeling plane being parallel to the line connecting both points (see Fig. 3.5). The toroidal basic shape obtained by a rotation about an axis through Z_0 , parallel to the x -axis results in an optimal focussing. In the meridional direction, a logarithmic spiral shape fulfils the optimal reflection conditions. In the presented case, due to the big radius of the logarithmic spiral, the shape is approximated by a spherical sector of radius R_M (see Fig. 3.5, left). An optimal design was found to be a monochromator consisting of 15 steps (see Fig. 3.6), cutting out parts of 6 surfaces, finally reducing the number of the steps to be processed to 6. Each step has a corresponding value of R_M (in the range from 955.3 to 1051.0 cm) and Z_0 (in the range from 945.2 to 1041.4 cm), which results in almost planar shapes with height differences in the micrometer range over the step surface. For this geometry with 0.5 mm thick HOPG crystals of 0.8° mosaicity, an integral transmission from the source to the cell target of 21.2 % was calculated. The reflected radiation intensity is not influenced by displacement of the source a few mm along x - or z -axis, however, a 2 mm displacement along the y -axis reduces the total transmission to 18.6 %. The simulated dose distribution at the target position after processing

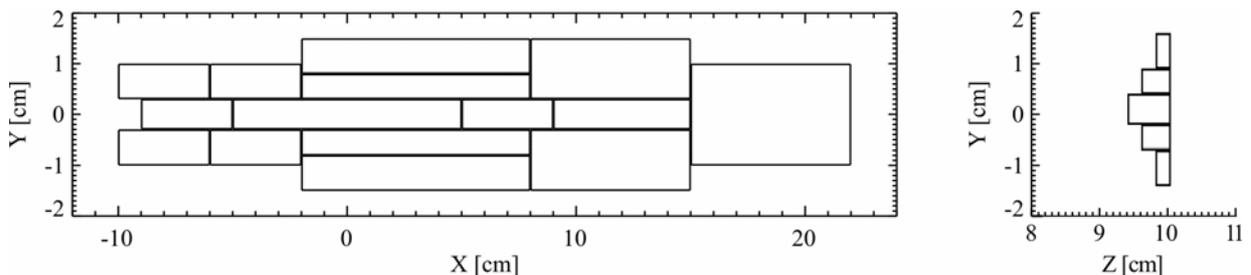


Fig. 3.6 Geometry of the stepped monochromator.

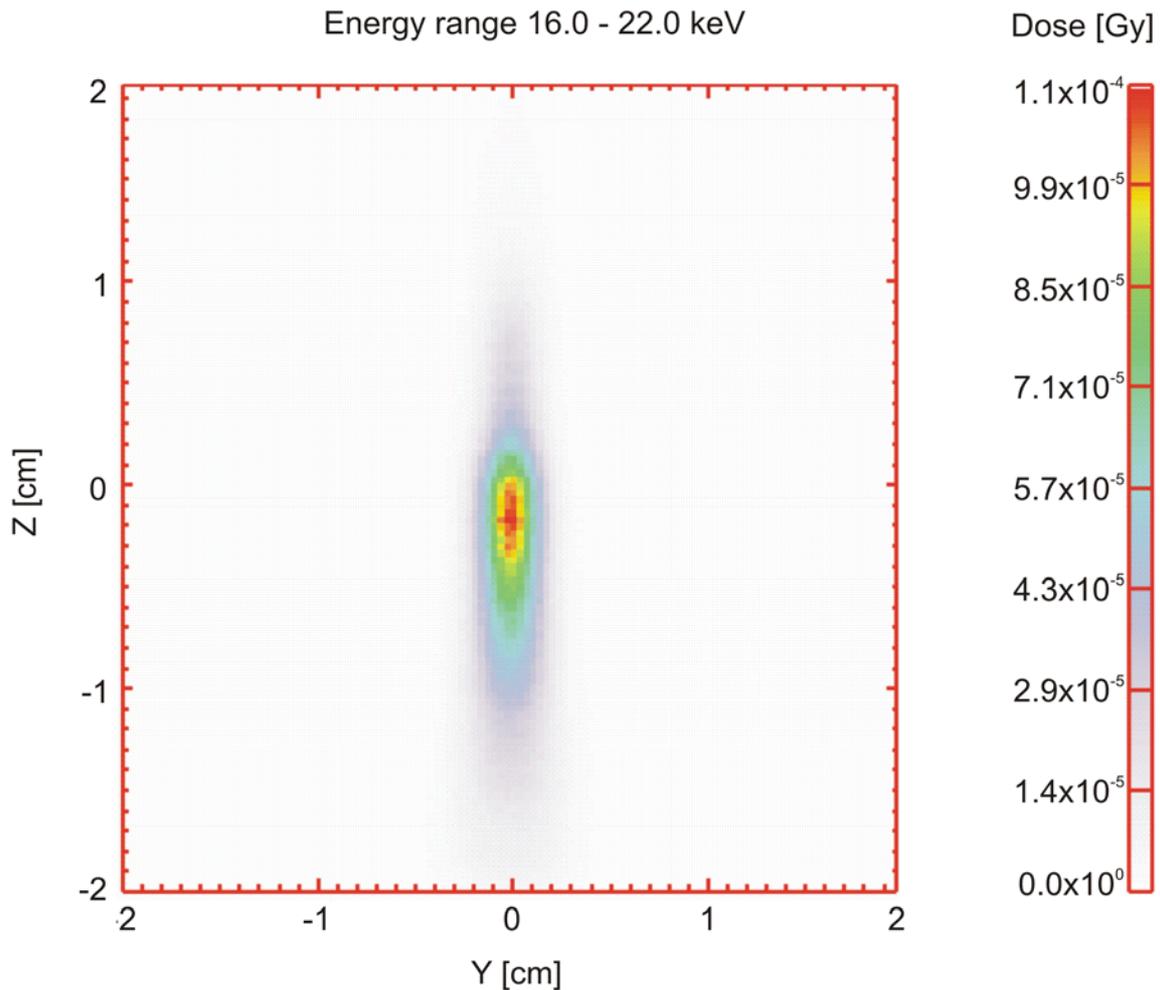


Fig. 3.7 Simulated spatial distribution of the CR photon dose at the cell target position after passing the HOPG monochromator at a distance to the channeling radiation source of 200 cm.

10^6 photons in the energy range from 16.0 to 22.0 keV, emitted from the CR source, is shown in Fig. 3.7. As seen from the figure, for a homogeneous dose delivery over the cell target area of 1 cm diameter (cf. Fig. 3.3), a scanning irradiation along the y -axis is required. However, before concluding about the spatial distribution at the cell target, experimental studies are necessary. A difference between the theoretical calculation and the measurements of the CR distribution as well as a monochromator reflectivity different from the expected one can result in a different intensity distribution at the target position.

The monochromator production was performed in two stages. First, the mould of the required shape and surface quality had to be produced. Then the HOPG layer was deposited on the surface. The choice of the mould material was limited by requirements of (1) radiation hardness, (2) low Z in order to minimize photon scattering, (3) the possibility of processing with high precision in order to obtain the exact geometry and surface quality and (4) reasonable cost. The precision of the mould production together with the quality of the HOPG crystals determine the final reflectivity and focussing properties of the monochromator, therefore, several materials (Zerodur glass ceramics, Sintimid and Tecapeek high performance plastics, PMMA) as well as different surface processing methods (polishing with a diamond suspension, fine sanding, milling with a diamond face cutter) were tested. As a finally

accepted solution, corresponding to the criteria mentioned above, a PMMA mould was produced on a CNC machine with high precision. However, the stepped shape could not be produced in a single run, therefore, each step was cut separately. In the biggest step, which was polished first, a mortise to place the small steps was cut out. The small steps were consecutively positioned inside, fixed and finally polished, the most outsticking one last. The measured surface roughness along the x -axis was only $0.2\ \mu\text{m}$, whereas the roughness along the y -axis was $1.8\ \mu\text{m}$. Direct deposition of the HOPG crystals (Optigraph, Moscow, Russia) was achieved for the biggest part of the surface, however, for covering the steps a minimal amount of liquid fast evaporating glue had to be used. The final shape of the monochromator is shown in Fig. 3.8.

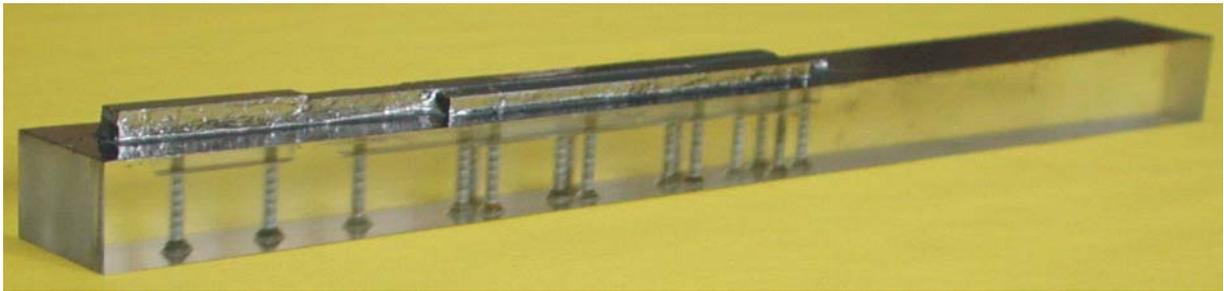


Fig. 3.8 A view of the final HOPG monochromator. The small steps of the PMMA mould, inserted in the biggest one, are fixed with plastic screws. The whole surface facing the CR beam has been then covered with HOPG.

3.3 Experiments

3.3.1 The experimental setup

The spectral distribution of CR was measured at two electron energies at ELBE. A schematic presentation of the ELBE facility with the accelerator hall and the secondary radiation caves is shown in Fig. 3.9. The electron beam, extracted from a thermionic cathode as pulses of 500 ps length, is accelerated electrostatically to 250 keV. The electron bunches are generated by a grid modulated with short high voltage pulses and subsequently compressed down to 10 ps upon injection into the 1.3 GHz accelerating structures. The main accelerator consists of two sections (Linac 1 and Linac 2 in Fig. 3.9), based on superconducting Nb radio frequency cavities. Accelerating field gradients of up to 15 MV/m can be obtained, and 20 MeV maximum energy gain is possible for each section. The average beam current can reach 1 mA. The beam is guided into the RP cave by deflection in a magnetic field. A detailed description of the accelerator can be found in [Gab00]. The accelerator parameters used for the channeling experiments are summarized in Table 3.3. The lower limitation of the electron energy comes from the growth of the emittance, particularly the increase of the energy spread of the beam. Since only the first accelerator module was set in operation up to now, the upper energy limitation was set by the achieved field gradients in the first cavity. The electron beam energy dispersion was determined from the field of the bending magnets. The bunch charge is not critical for the CR production, but since it can be used to optimize the transversal emittance, the lowest possible bunch charge of 0.1 pC was chosen. The discrepancy between the measured and the design values for the transverse emittance arises from the energy spread and the beam tuning into the RP cave, since the values obtained at the accelerator exit were within the expected value of 1 mm mrad.

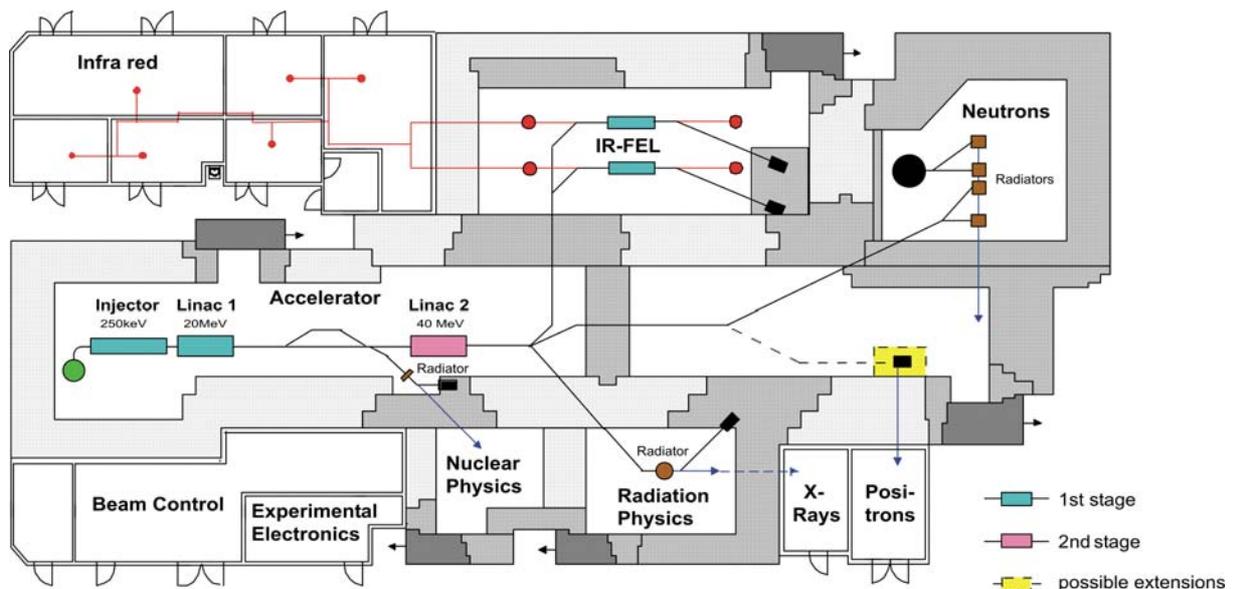


Fig. 3.9 Schematic view of the ELBE accelerator hall.

Table 3.3 *ELBE parameters used in the channeling experiments.*

ELBE electron beam parameters in the RP cave	Project	Experiment
Electron kinetic energy / MeV	12 ... 40	14.1 and 16.5
Energy dispersion / %	0.2 ... 0.9	0.9
Maximal average beam current Average beam current for CR measurement	200 μ A	\leq 100 μ A several nA
Normalized transverse emittance (rms) ϵ_x / mm mrad ϵ_y / mm mrad	\leq 1 \leq 1	4.4 (at 0.1 pC) 7.4 (at 0.1 pC)
Normalized longitudinal emittance (rms) / keV ps	50	37 (at 3 pC)
Time structure: Micropulse duration / ps Micropulse repetition rate / MHz Macropulse duration / ms Macropulse repetition rate / Hz	\approx 2 260 and 13 0.1 ... 40 or cw* 1 ... 25	\approx 2 13/2 ⁿ , n = 0 ... 8 0.1 ... 40 or cw* 25 or cw*

* continuous wave

The experimental set-up in the RP cave is shown in Fig. 3.10. The electron beam enters the cave after passing a switching magnet in the accelerator hall. The quadrupole magnets 1 and 2 provide the necessary focussing. Then the beam is deflected into the target chamber by dipole magnet 1. At the position of the diamond target, a beam viewer for the beam tuning, based on detection of optical transition radiation (OTR) from a 18 μ m thick Al foil, can be placed. In order to orient the diamond crystal, a 3-axes goniometer was used with 2 target positions. In the channeling experiments, the positions were occupied by the diamond crystal and the OTR screen, so no comparison of different diamond crystals or with an amorphous target could be made without opening and venting the goniometer chamber. However, this goniometer is able to function without lubricants, which meets the requirement of a hydrocarbon-free ultra high vacuum within the beamline. In this work, the channeling experiments at ELBE, performed in November 2003 and June 2004, will be described. For the first of the presented experiments, the beam current measurement systems, shown in Fig. 3.10 – the secondary electron monitor and the Faraday cup – were not yet available. The CR produced in the diamond crystal is detected with a semiconductor detector. The same detector systems were used at the ELBE CR beam as well as at an X-ray tube (see Chapter 6.2). For measurements performed in this work, Si PIN photodiodes and a CdZnTe detector were used (all from Amptek, Bedford, USA). Their main parameters are listed in Table 3.4. These detectors require no liquid nitrogen cooling and provide sufficient energy resolution. The detectors, together with the preamplifier and the built-in thermoelectric cooler have a size of about $12 \times 5 \times 3$ cm³. The preamplifier signal is transferred to the amplifier by a 2 m cable. Two systems for signal processing were available: a stand-alone multichannel analyser MCA 166 with a palmtop computer for spectra visualisation (GBS Elektronik,

Großerkmannsdorf, Germany), as well as a CAMAC-based data acquisition system which was controlled and visualised by a home-made software package [Cre03]. The first data acquisition system has the advantage of being extremely compact and easy to operate and was used for the results presented here. In order to protect the data acquisition electronics from the radiation background during beam tuning and measurement, it was placed outside the cave, using a 60 m long impedance matched cable from the detector amplifier. The detector energy calibration was performed using the prominent characteristic X-ray or γ -lines of ^{55}Fe , ^{241}Am , ^{210}Pb and ^{133}Ba sources. Typically, the energy resolution (FWHM) of ^{55}Fe K_{α} line at 5.9 keV for the XR-100CR detector was determined to be (300 ± 2) eV, for XR-100T (231 ± 1) eV and for XR-100T-CZT (411 ± 2) eV. The choice of the detector was according to its spectral sensitivity and resolution and the expected count rate. Since the CR energy and intensity are related to the angle of observation, care has to be taken for the precise detector alignment and collimation. The detector alignment was controlled with a laser positioning system. In order to shield the detector from the scattered radiation, a Pb collimator was used. All detectors were constructed similarly, the detector mounted behind a Be window in the detector finger (with a diameter of about 1.8 cm) and the preamplifier directly placed in the rear part. This allowed to use the same detector shielding and collimators for all detectors. The Pb shielding was a hollow cylinder of 27 cm length, with 14 cm outer diameter and 2.05 cm inner diameter, aligned to the beam axis. Here the detector finger was inserted, so that the detector was facing the crystal, at the same time being sideward entirely shielded. In order to decrease the angular acceptance of the detector, a hollow cylindrical collimator of 14 cm length, 2.0 cm outer and a 0.5 or 0.1 cm inner diameter was placed in the opening in front of the detector. In order to further decrease the solid angle, the detector was placed at the maximum possible distance from the source. However, the long air path resulted in a high attenuation of the low-energy part of the measured spectral distribution. Therefore, an evacuated tube at about 2 mbar was connected to the beamline in front of the collimator. During beam tuning, performed at higher beam current of about $2 \mu\text{A}$, a Pb shutter of 10 cm thickness was placed in front of the detector.

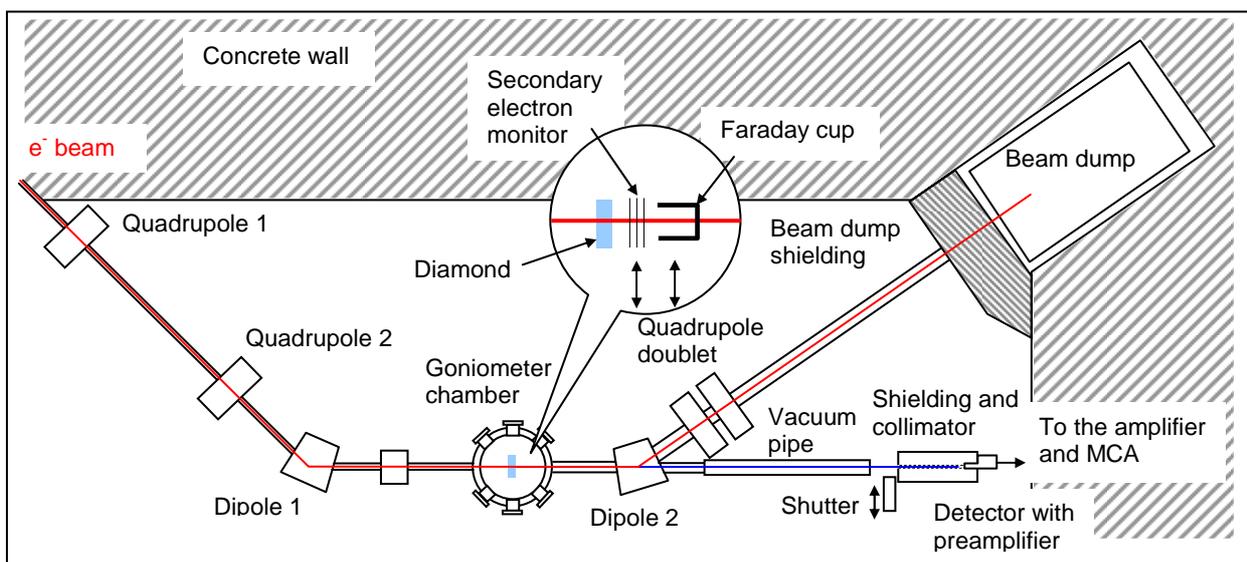


Fig. 3.10 Schematic drawing of the beamline elements in the RP cave.

Table 3.4 Main properties of the used semiconductor detectors.

Detector type		Recommended detection range / keV	Thickness / μm	Size / mm^2	Thickness of Be window / μm	Shaping time / μs
Si PIN	XR-100CR	1.5 - 30	300	3.6×3.6	25	12
	XR-100T	1.5 - 30	300	2.4×2.8	25	12
XR-100T-CZT (CdZnTe)		2 - 400*	2000	3×3	250	3

* Outside this range the detector efficiency is below 3 %

3.3.2 Measurement of the spectral distribution and intensity of the CR and comparison to the calculation

The crystals of natural diamond of different thickness were obtained from Drukker International (The Netherlands). Chosen was type IIa, which corresponds to a concentration of B atoms of 0.25 ppm and a concentration of N atoms below the detection threshold of UV-spectroscopy (less than 10 ppm). The crystals were cut perpendicularly to the [110] axis which is perpendicular to the (110) plane. The crystal which was used in the presented experiments, had a nominal thickness of 35 μm and was measured to be $42.6 \pm 4.0 \mu\text{m}$ thick. The orientation of the crystal had to be checked additionally, since the accuracy of the preliminary orientation was only about ± 3 deg. This can be done in the channeling experiments by varying the crystal tilt angle relative to the electron beam. As the different axes and planes come into

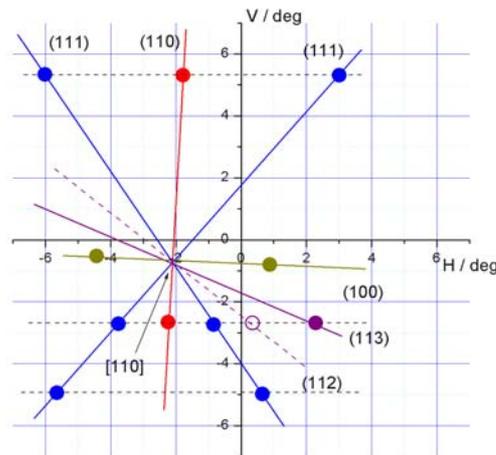


Fig. 3.11 Crystal map of the diamond obtained by CR measurements. The axes represent a relative tilt angle to the initial crystal orientation, presented as goniometer tilting angles. The points represent maxima in the CR peak intensity and therefore, correspond to the positions of axes or planes, which are shown by the lines in the corresponding colour. Perpendicularly to the plane of the paper, the [110] axis is obtained as the intersection line of the shown planes.

the channeling condition, the CR spectrum is changing and the peaks of the corresponding transitions appear. A plot of the intensities versus the tilt angles H and V , measured in two planes perpendicular to each other, results in a crystal map, which is presented in Fig. 3.11. The CR spectral distribution was measured for two electron kinetic energies, 14.1 MeV and 16.5 MeV for the (110) planar channeling. In order to subtract the bremsstrahlung background, reference spectra were measured at the same electron beam setting and detector position, but at a misaligned crystal position where no channeling was observed. In fact, it was difficult to achieve such a position with the used crystal, since many reflections from the neighbouring axes and planes were detectable.

3.3.3. Extraction of the CR photon flux distribution

The CR spectrum at 14.1 MeV electron energy was measured with the XR-100T detector using the collimator of 1 mm diameter, at a distance of 317 cm from the crystal, from which, after the high vacuum path in the beamline and the evacuated tube, 35 cm was air. The CR spectrum at 16.5 MeV was measured with the XR-100T-CZT detector at a distance of 319 cm from the source using the evacuated tube, and the beam path in air was 36 cm. For this measurement, the collimator of 5 mm diameter was used. For both electron energies, a reference bremsstrahlung spectrum at a misaligned crystal position, but for the same crystal thickness, was measured. These spectra were corrected for detector dead time and scaled to the same measurement time as in the CR case. Further, additional correction for electron beam intensity was performed in the case of 14.1 MeV using the current values obtained by the secondary electron monitor. For the measurement at 16.5 MeV, since no monitor was available, it was assumed that the electron beam intensity was the same for the CR as well as bremsstrahlung measurement. The resulting spectral distributions measured under channeling condition together with the corresponding bremsstrahlung spectrum for 14.1 and 16.5 MeV electron energies are presented in Fig. 3.12, a and b. In both cases, the increase of the bremsstrahlung yield in the channeling regime is visible. In order to evaluate the intensity of the CR peaks, the spectra have to be corrected for attenuation in the beam path and detector efficiency, and the enhanced bremsstrahlung background has to be subtracted. The factors determining the energy-dependent detector efficiency are the thickness of the detector Be window for the low energy range and the detector thickness for the high energy range. The detector efficiency was calculated using the photon interaction cross-section, taken from the NIST Physical Reference Data [Nis98] and the density and stoichiometric composition of the detector material. An example of XR-100CR detector efficiency calculated for the corresponding thickness is shown in Fig. 3.13. In the same way, a correction for the attenuation of the photon beam in the Be exit window of the beamline and in the air, was performed. The enhanced bremsstrahlung background was subtracted from the CR spectrum using the measured bremsstrahlung spectrum. For the necessary scaling, a region in the CR spectrum where no peaks from the bound-to-bound or free-to-bound transitions were present, was used. This resulted in the spectral distributions presented in Fig. 3.14. The peak shape of the CR was approximated using a Voigt profile (a convolution of a Lorentz and a Gauss function) by numerical integration using the software Mathematica 4.1 [Wol00]. The wide peaks of the

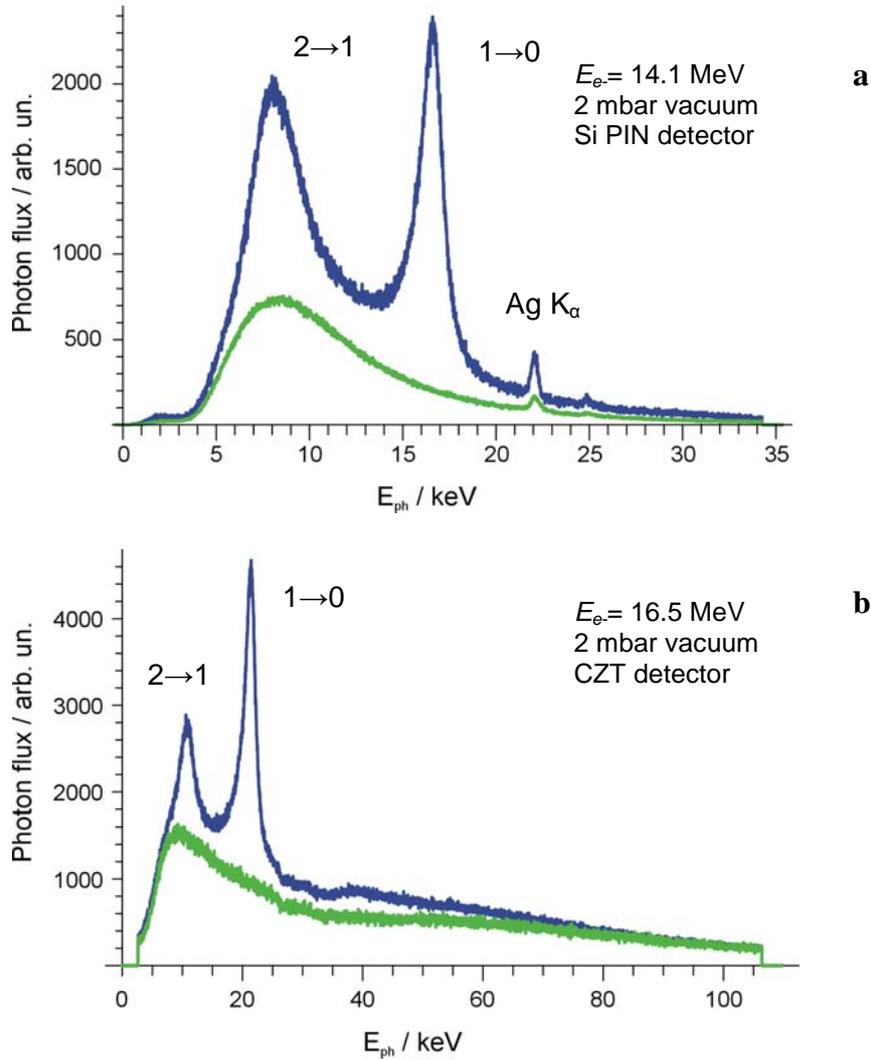


Fig. 3.12 Measured CR spectrum for (110) channeling in a $42.6 \mu\text{m}$ diamond (blue curve) together with the bremsstrahlung spectrum at a misaligned crystal position (green curve). Both curves represent a measurement at the same measurement time and electron current.

a Electron energy 14.1 MeV. The Ag K_α peak is a Si PIN detector artefact.

b Electron energy 16.5 MeV.

free-to-bound transition which are observed for both electron energies at photon energy higher than the highest-energy CR transition, were approximated by a Gaussian. The CR energy and linewidth, obtained from the parameters of the fitted curves, are presented in Table 3.5. The self-absorption in the diamond was not included in the corrections, since it is less than 7 % for the lowest considered CR energy. The error of the measured CR energy was determined by its standard error from the fitting procedure and the error of the energy calibration. For comparison, the theoretical values of the CR energy were obtained according to Eqs. (3.9) and (3.11) and the uncertainty was calculated from the electron energy uncertainty, which is ± 1.5 %. The assumption of a Voigt profile of the measured lines allows to distinguish between the intrinsic Lorentzian line shape and the instrumental broadening due to the finite detector resolution, which has a Gaussian shape. As a CR linewidth, only the FWHM of the Lorentzian is given, together with its standard error obtained from the fitting procedure. The number of

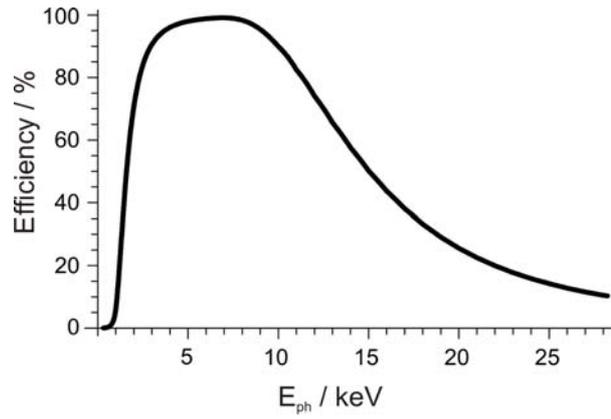


Fig. 3.13 Detector efficiency for a 300 μm thick Si PIN detector with a 25 μm Be window.

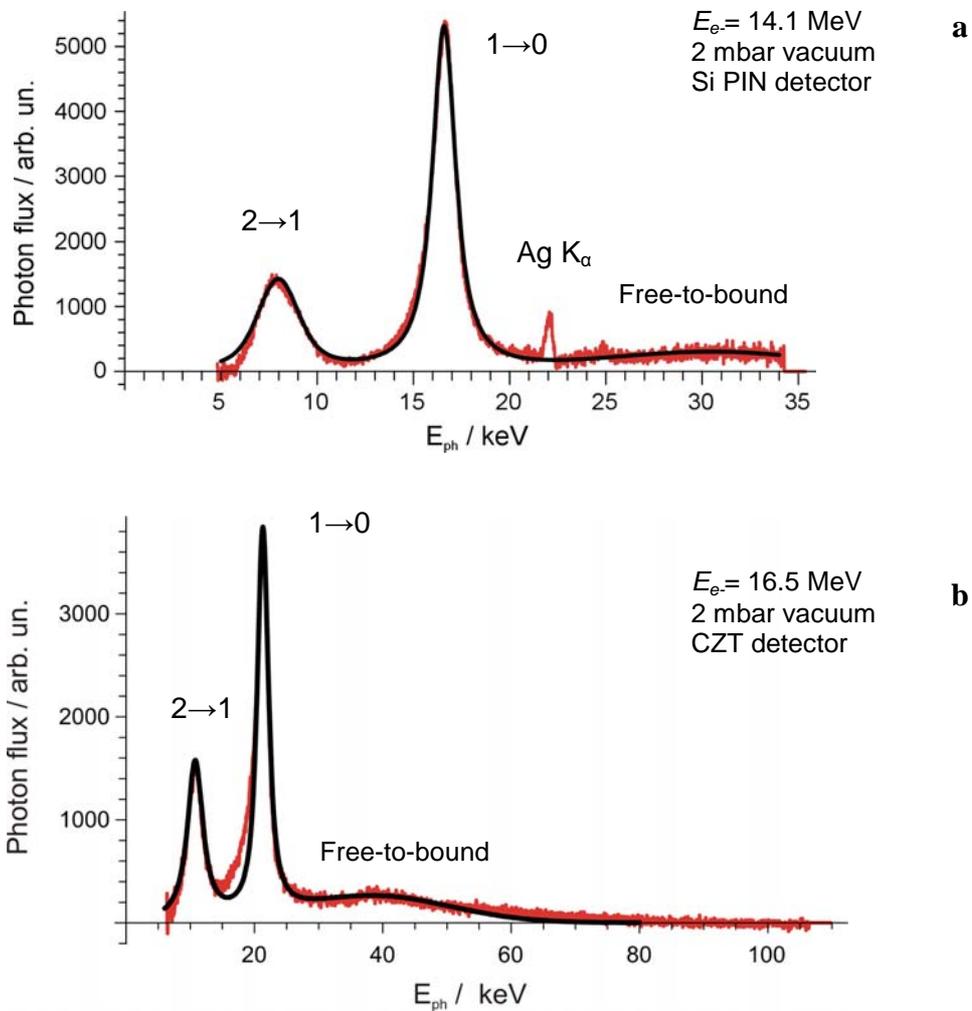


Fig. 3.14 Channeling radiation spectrum from Fig. 3.12 for the (110) channeling in a 42.6 μm thick diamond obtained after subtraction of the bremsstrahlung background. The CR peaks of the 1→0 and 2→1 transitions have been fitted to a Voigt function, and the free-to-bound peak to a Gaussian.

a Electron energy 14.1 MeV

b Electron energy 16.5 MeV.

Table 3.5 Experimental parameters of the CR for the studied planar (110) channeling in diamond. The crystal thickness was 42.6 μm .

Electron energy / MeV	Transition	Photon energy / keV		Linewidth / keV	Photon yield / ph/(sr e ⁻)	
		Observed	Calculated	Observed	Observed	Calculated
14.1	1→0	16.6 ± 0.3	17.5 ± 0.4	1.32 ± 0.02	0.19 ± 0.07	0.24
	2→1	8.0 ± 0.2	8.1 ± 0.2	1.42 ± 0.17	0.06 ± 0.02	0.075
16.5	1→0	21.3 ± 0.4	22.8 ± 0.5	1.70 ± 0.05	0.12 ± 0.04	0.37
	2→1	10.8 ± 0.2	11.8 ± 0.3	2.73 ± 0.10	0.06 ± 0.02	0.17

counts in the CR peak was evaluated from the measured flux distributions after the subtraction of the enhanced bremsstrahlung, where the contribution of the intervening neighbouring peaks was subtracted using their approximated peak shapes. In order to determine the CR photon yield, knowledge of the absolute electron current is necessary. Although in the case of 14.1 MeV, electron current was measured by the secondary electron monitor close to the crystal, electron scattering in the crystal could result in broadening of the CR cone and decrease of the registered flux in the detector due to the small diameter of the used collimator. Therefore, the absolute electron current for the CR production was calculated using a theoretical bremsstrahlung distribution, which for relativistic particles has the following form [Jac83]:

$$\frac{d^3 N_{ph}}{d\Omega dz dE_{ph}} = 1.47 \times 10^{-27} N_v \frac{\gamma^2 Z_2^2}{\beta^2} \ln \left(\frac{233}{Z_2^{1/3}} \right) \frac{1 + \gamma^4 \theta^4}{(1 + \gamma^2 \theta^2)^4} \frac{1}{E_{ph}} \quad (3.16)$$

If the atomic density N_v is expressed in cm^{-3} and the photon energy E_{ph} in keV, the number of bremsstrahlung photons per electron at an angle θ with the electron direction is obtained. However, since this expression is valid for amorphous targets, it cannot be used directly for the description of the background in the CR case, since the enhanced bremsstrahlung or the free-to bound transitions under channeling conditions are not considered. Therefore, the random direction bremsstrahlung spectra were used for both electron energies. They were measured at the same crystal thickness as the CR spectra, corrected for detector dead time and scaled to the same measurement time as in the CR case. Again, in the case of 14.1 MeV, the bremsstrahlung spectrum was scaled to the same electron beam intensity as in the CR measurement, using the current value obtained by the secondary electron monitor. This scaling was not performed in the case of 16.5 MeV. Then, from the ratio of the measured bremsstrahlung yield in a certain energy interval and the calculated according to Eq. (3.16) bremsstrahlung yield, the reduced absolute electron current was determined. It was then used to obtain the absolute CR photon yield, presented in the sixth column of Table 3.5. This procedure of normalisation and correction of the measured CR yield is a source of systematic and statistical errors. In the calculated uncertainty of the

electron current, the largest contributions are the uncertainties of the crystal thickness ($\pm 9\%$) and of the detector solid angle ($\pm 10\%$), whereas the electron energy uncertainty is $\pm 1.5\%$, and the electron energy spread $\pm 0.9\%$. In addition, the uncertainty of the CR spectral flux distribution contains the statistical error from the detector count number and the uncertainty of the detector efficiency correction. For the considered CR spectra, the statistical error of the detector count number is minimal ($\pm 0.1\%$). The uncertainty of the detector efficiency correction derives from the uncertainty of the mass attenuation coefficients for Si and Be, estimated for the used NIST data [Nis98] to be less than 5% in the considered energy range [Hub99], and the uncertainty of the detector and Be window thickness. For both detectors, it was found to be $\pm 8\%$. The calculated CR yield, shown in the last column of Table 3.5, was performed as described in Chapter 3.1.3, taking into account population dynamics and self-absorption in the diamond in order to have a direct comparison to the measured CR yield.

However, in order to compare the absolute values of the experimental results to the theoretically predicted, the processes additionally contributing to the uncertainty have to be discussed. Due to the spatially variant energy distribution of CR, the emitted photon energy and linewidth are connected and influenced by the same factors. The line broadening of the ideal δ -distribution shape due to the finite lifetime of the initial and final state, expressed by the coherence length, has been discussed in Chapter 3.2. This intrinsic linewidth cannot be improved by the experimental procedure and is rather small. Other line broadening sources are (1) Bloch-wave broadening, (2) finite crystal thickness, (3) energy uncertainty and spread of the electron beam, (4) Doppler effect, (5) non-zero beam divergence, (6) finite beam and detector size, (7) misalignment of the beam and/or detector relative to the beamline axis and (8) multiple scattering effects. The Bloch-wave broadening, caused by the dependence of the eigenfunctions on the transverse vector k , results in broadening of the energy states and therefore, of the emitted linewidth. However, it affects only the high-lying states, and from the considered transitions it influences only the $2 \rightarrow 1$ transition. The finite crystal thickness plays a role only for a crystal thickness that compares to the coherence length of the individual states and can, therefore, be neglected in the present case. Both effects influence the CR linewidth, but not the angular CR distribution. The contribution of the electron energy spread to the linewidth is about 1% . All other effects contribute to the line broadening, but additionally they cause a line shift, actually as a result of the Doppler effect. As seen from Eq. (3.11), the detection at any angle $\Delta\theta \neq 0$ results in observation of CR energy lower than in the direction of the electron beam, and therefore, in an energy uncertainty

$$\frac{\Delta E_{ph}}{E_{ph}} = (\gamma \Delta\theta)^2 \quad (3.17)$$

This effect is a source of line asymmetry and shift of the mean CR energy. The influence of the non-zero beam divergence, beam and detector size are independent from each other and can be estimated from the electron beam characteristics and experiment geometry. The resulting shift in the observation angle is about 1.2 mrad in the channeling plane and about 1 mrad in the transversal direction, mainly as a contribution of the electron beam emittance. These effects result in a maximum decrease of 1% in the observed photon energy. On the other hand, the contribution of the electron multiple scattering in the

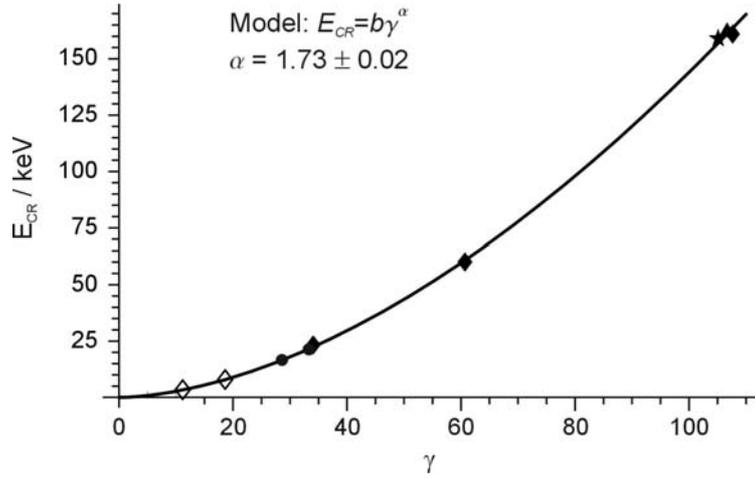


Fig. 3.15 Dependence of the observed photon energy E_{CR} for electron channeling in diamond (110) plane on the electron energy expressed by γ . The solid curve represents a least-squares fit to the following experimental data: \diamond - Genz et al. [Gen96], \bullet - this work, \blacklozenge - Klein et al. [Kle85], \star - Gouanere et al. [Gou88], \blacktriangle - Gouanere et al. [Gou82].

crystal can be given by the following expression for the mean multiple scattering angle [Kle85]:

$$\Delta\theta = \frac{14}{E_{e^-}} \sqrt{\frac{d_0}{L}} \left[1 + \frac{1}{9} \log\left(\frac{d_0}{L}\right) \right] \quad (3.18)$$

where d_0 is the crystal thickness, L is the radiation length (for diamond it is equal to 0.106 m) and E_{e^-} is the electron energy in MeV. However, this expression for the multiple scattering angle has been determined for an amorphous target. For channeling conditions, this effect has not been sufficiently studied and multiplication factors of 0.3 [Cho99] up to less than about 2 [Kep89] have been found. For a factor of 1.0, assumed in the present calculation for diamond, the mean scattering angle is obtained to be about 12.1 mrad at 14.1 MeV and about 10.3 mrad at 16.5 MeV. This contribution leads to a

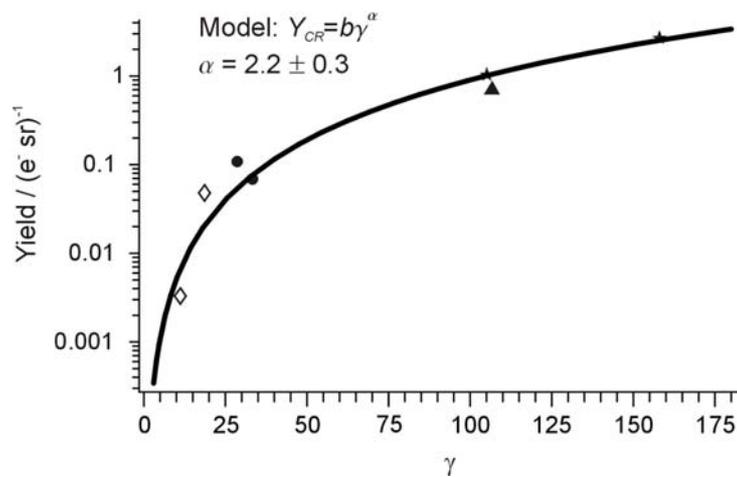


Fig. 3.16 Dependence of the observed photon yield for electron channeling in diamond (110) on the electron energy, scaled for a crystal thickness 20μ : \diamond - Genz et al. [Gen96], \bullet - this work, \star - Gouanere et al. [Gou88], \blacktriangle - Gouanere et al. [Gou82]. The black solid line is a least-squares fit to the data.

broadening of the CR line and to a maximal shift in the emitted photon energy of 12 % for both electron energy values. However, the radiation length is taken for an amorphous target, therefore, it could be quite overestimated in the considered case of channeling conditions. A comparison of the measured and calculated data for the photon energy and yield for both studied electron energies is shown in Table 3.5. In the calculated values for both electron energies, a systematic overestimation of the measured photon energy is observed. As discussed above, the main contribution to the deviation in the measured photon energy comes from the multiple scattering effects. With respect to this, the overestimation of the calculated photon energy is reasonable. A good correspondence to the calculated values of the CR yield for 14.1 MeV is observed, however, for 16.5 MeV, the CR yield is overestimated. The reason for this is probably the inaccuracy of the absolute electron current determination, since, as already mentioned, no secondary electron monitor was available to account for the differences in the electron beam intensity and therefore to allow accurate determination of the enhanced bremsstrahlung yield.

In order to prove the plausibility of the measured photon energy and intensity, a comparison to the available literature data was performed. In Fig. 3.15, the experimentally determined CR photon energy for the $1 \rightarrow 0$ transition for (110) planar channeling in diamond from several authors in the electron energy region 5.2 - 54.5 MeV (see also Table 3.1) together with the present measured values, are shown. The CR energy dependence on the electron energy have been fitted by a least-squares fit to the model $E_{CR} = b\gamma^\alpha$, resulting in an α -value of 1.73 ± 0.02 . This value is higher than the widely assumed $\gamma^{3/2}$ dependence [Gen96], and closer to the value of 1.67, experimentally found by Klein et al. [Kle85] for this transition. In addition, the CR photon yield dependence on the electron energy was studied and compared to the published data. In Fig. 3.16, the experimentally determined photon yield for the $1 \rightarrow 0$ transition for (110) planar channeling in diamond from several authors (see also Table 3.1) together with the present measured values, is shown. The electron energy dependence of the yield has been fitted by a least-squares fit to the model $Y_{CR} = b\gamma^\alpha$, resulting in an α -value of 2.2 ± 0.3 . This value is smaller than the predicted $\gamma^{5/2}$ dependence, also observed by Genz et al. [Gen96], however, for self-absorption corrected CR yield. A better estimation of this dependence and decrease of the uncertainty can be only obtained after performing more measurements.

3.3.4. Dose calculation

In order to prove the feasibility of the measured CR source properties for radiobiological applications, the dose rate delivered by the CR as well as bremsstrahlung to a cell target was calculated from the measured spectral photon flux distributions. The same irradiation setup was assumed as described in Chapter 3.1.4, where the cell target was simulated by a 4 μm thick tissue equivalent layer, placed on a 10 μm culture dish base and covered with 8 mm culture medium (considered tissue-equivalent). The attenuation in a 100 μm Be window was also considered. The measured flux distribution was corrected for detector dead time and efficiency. Afterwards, the spectral distribution of dose rate $\dot{D}(E_{ph})$ was calculated from the spectral flux density distribution using the following expression:

$$\dot{D}(E_{ph}) = \frac{\Phi(E_{ph})E_{ph}\mu_{en}(E_{ph})}{\rho} \quad (3.19)$$

where $\Phi(E_{ph})$ is the photon flux density at the cell target position, $\mu_{en}(E_{ph})$ is the mass-energy absorption coefficient of the target material, and ρ is the density of the cell target. This method of spectral dose rate distribution calculation has been applied for CR as well as for X-ray tube radiation (see Chapter 6). The mass-energy absorption coefficients and the mass attenuation coefficients for the materials used in the calculations were taken from the NIST Physical Reference Data [Nis98].

However, the application of this approach is justified only for energies below about 200 keV, where the secondary electron equilibrium is established already on the surface of the target. This is not the case at higher energies, where the dose first increases with penetration depth up to a distance which approximately corresponds to the range of the secondary electrons in the medium (dose build-up effect). The measurement of the dose in this case is difficult because a dosimeter with a sensitive volume comparable to the cell thickness has to be used. One possibility is to use a dosimeter based on thermally stimulated exoelectron emission (TSEE). The applicability of such a dosimeter has been tested and is described in Chapter 4. Calculation of the dose rate in the high energy range is only possible using a Monte Carlo code considering the irradiation geometry. Therefore, the fluence to dose conversion factors obtained by the simulation described in Chapter 3.1.4 were used to calculate the contribution to the dose due to the bremsstrahlung background. The necessary energy dependent bremsstrahlung flux was calculated by integration of Eq. (3.16) over the detector solid angle and crystal thickness. This theoretical spectrum was scaled to the corresponding CR spectrum and extrapolated to the high energy limit. The obtained values for the spectral dose distribution are presented in Tables 3.6 and 3.7 for the electron energies 14.1 and 16.5 MeV, respectively. A comparison with the simulation data, presented in Table 3.2, reveals a difference in the absolute values of the dose in all energy ranges. Since in the simulation, a thicker crystal and a smaller distance to the source were assumed and the contribution of

Table 3.6 Dose in the cell target from 14.1 MeV electron channeling along the (110) plane in a 42.6 μm diamond crystal, at a distance of 3.17 m from the CR source.

Photon energy range / keV	Dose / 10^{-18} Gy/e ⁻			
	With 100 μm Be window		With 100 μm Be window and 70 μm Al absorber	
	Bremsstrahlung	CR	Bremsstrahlung	CR
1 - 10	98.0	-	5.4	-
10 - 100	8.4	-	6.9	-
100 - 1.41×10^4	2.5	-	2.5	-
7 - 9 (2 \rightarrow 1)	6.9	5.1	2.5	1.9
15 - 18.5 (1 \rightarrow 0)	1.2	4.0	1.1	3.6

Table 3.7 Dose in the cell target from 16.5 MeV electron channeling along the (110) plane in a 42.6 μm diamond crystal, at a distance of 3.19 m from the CR source.

Photon energy range / keV	Dose / 10^{-18} Gy/e $^{-}$			
	With 100 μm Be window		With 100 μm Be window and 70 μm Al absorber	
	Bremsstrahlung	CR	Bremsstrahlung	CR
1 - 10	96.9	-	5.3	-
10 - 100	8.3	-	6.8	-
100 - 1.65×10^4	2.5	-	2.5	-
9.5 - 12 (2 \rightarrow 1)	3.5	2.1	2.3	1.4
19 - 23 (1 \rightarrow 0)	0.7	1.4	0.6	1.3

all sources of primary as well as secondary scattered bremsstrahlung were included, such a result is reasonable. The dose rate from the bremsstrahlung in the CR lines region is calculated to be comparable to the CR itself. However, this is a useful contribution, since it results in intensity increase in the desired energy region. As shown in Tables 3.6 and 3.7, the low-energy bremsstrahlung contribution is easily decreased using an attenuation plate (see also Table 3.2), while for separating off the rest of the background radiation, the monochromator will be used. After scaling the dose rate in the CR line region to a current of 100 μA , crystal thickness of 100 μm and a reduced distance of 1.5 m from the source, dose rate values in the range 0.6 - 2.3 Gy/min for both electron energies are obtained, which are reasonable for radiobiological experiments. Possibilities to further increase the dose rate by increasing the CR yield are increasing the crystal thickness or electron current. However, the increase in the thickness results in an increase of the multiple scattering, and the second possibility has to be experimentally tested in order to prove the thermal resistance of the diamond crystal. Additionally, the dose rate is decreased after the monochromatisation.

The first experimental results prove the applicability of the CR source for the chosen radiobiological studies, showing the reasonable agreement with the calculated photon energy and intensity as well as their dependence on the electron energy. The dose rate at the target position is sufficient for cell irradiation, which shows the feasibility of such a quasi-monochromatic, tunable X-ray source for radiobiological studies. However, the calculated monochromator reflectivity has still to be experimentally proved, and, based on the presented prototype, monochromators for a large number of energies have to be produced. Extension of these first encouraging experiments to high electron currents and a larger electron energy range (12 - 40 MeV) are desirable.

4 Investigation of a dosimetry system for experimental determination of dose in a cell monolayer

4.1 Principles of dose measurement in tissue and application to thin layers

The RBE determination on the cellular level requires precise knowing of the doses applied by the two compared radiation qualities. Since no direct measurement of the imparted energy in the cell volume is possible, the dosimetric principles for measurement of absorbed dose in a probe have to be applied, based on dose measurement in a substitute probe and subsequent correction for the cell specific properties [Dör92]. For this purpose, one approach is to fulfil the condition of secondary particle equilibrium, where the energy brought into the probe by the secondary charged particles is equal to the energy taken by them out of the probe. In the case of low-energy photon fields, this condition is simplified to the requirement that the secondary electrons have to be produced and to lose their kinetic energy completely in the sensitive volume. This results in the requirement for the sensitive volume to be larger than the maximal range of the secondary electrons, but smaller than the primary photon range. Additionally, the walls have to be thick enough for absorbing the secondary particles emerging outside the chamber and thin enough not to attenuate the primary radiation. In the ideal case, according to Fano's theorem, the sensitive volume and the walls of the chamber have to be of the same atomic composition, but not necessarily of the same density. A good approximation of this principle is an air-filled ionisation chamber placed in air, with walls made of air-equivalent material. It allows absolute dose determination with high precision and is most widely used in practice due to its simple construction. Under the above conditions, the dose in a certain medium, e.g. the dose in the cell D_c , can be obtained from the measured dose in the air-chamber D_a using the mass-energy absorption coefficients of the medium and air:

$$D_c = \frac{(\mu_{en} / \rho)_c}{(\mu_{en} / \rho)_a} D_a \quad (4.1)$$

In high-energy photon dosimetry the secondary particle equilibrium cannot be fulfilled, therefore, the Bragg-Gray principle is applied, where the requirement to the dose in the probe is that it is entirely due to the secondary electrons. Again, an ionisation chamber calibrated for the certain radiation quality with appropriate geometry can be placed at the cell position and the dose in the cell can be obtained from the measured dose in air:

$$D_c = \frac{(S / \rho)_c}{(S / \rho)_a} D_a \quad (4.2)$$

where S is the stopping power for the corresponding radiation quality. These two standard methods for photon dosimetry can be used to perform absolute dose measurements with a calibrated ionisation chamber in the energy range from several keV up to several MeV. The application of the basic dosimetry principles can be complicated in the case of thin layers, when low-penetrating radiation is attenuated over the layer thickness, and in the case of dose inhomogeneity due to the presence of high-Z

materials or in the build-up region of high-energy photon beams. In the radiobiological studies, cultured cells are irradiated either as a cell suspension, or as a monolayer attached to a substrate. The second method was used in the present work. Therefore, care has to be taken to measure the dose at the cell monolayer position and at the same distribution of secondary particles. The determination of dose in a living cell is additionally complicated because of the natural liquid environment, and in practice, both the cell material and the environment have to be approximated by materials with similar properties. For the absolute dose and dose inhomogeneity determination, a cell-equivalent (in thickness of the sensitive volume and atomic composition) dosimeter is desirable, whereas for the daily monitoring of the absorbed dose it is more important to have an easy to handle calibrated dosimeter with small sensitive volume and stable response.

4.2 X-ray dose rate measurements with an ionisation chamber and determination of spectral dose distribution

In the case of absolute dose measurements in the soft and hard X-ray range, the most widely used system is the air-filled ionisation chamber and an electrometer. The absolute dose in water D_w , measured by an open-air chamber is determined by

$$D_w = k_Q N_w k_p Q \quad (4.3)$$

where k_Q is the radiation quality correction factor, N_w is the calibration factor of the ionisation chamber, k_p is the correction factor for air density, and Q is the measured charge. The factor k_Q represents the energy dependence of the chamber response and has to be determined individually for each chamber and measured radiation quality. The calibration factor N_w represents the dose in water per charge unit for the used electrometer. The air density correction factor compensates for the difference in the air pressure and temperature during calibration and during measurement. Since the use of each ionisation chamber is restricted to a certain photon energy, dose and dose rate range, several ionisation chambers were used for dose rate measurements in this work. Commercially available chambers are well optimised and have stable response and they can be used for absolute dose determination as well as for dose monitoring during irradiation procedure.

The following chambers were used in the soft and hard X-ray energy range: a flat soft X-ray ionisation chamber, a thimble chamber and a Farmer chamber. Together with an universal dosimeter Unidos, three measurement systems could be built. In addition, all systems were doubled to assure the possibility of measurements in parallel at two different setups – the ELBE soft X-ray beam in the RP cave and an X-ray tube operated in another room in the ELBE building. All dosimetric devices were purchased from PTW, Freiburg, Germany. The properties of the used chambers are listed in Table 4.1. The possible modes of measurement with the dosimeter were measurement of dose rate (current) or dose (accumulated charge). This allowed to expand the dose range, measuring very low dose rates.

Table 4.1 Properties of the ionisation chambers. The energy range is presented as an X-ray tube voltage, stated by the producer PTW.

Name	PTW Type	Volume / cm ³	Nominal energy range		D_{\min} / μGy	\dot{D}_{\max}^* / Gy/min
			photons	electrons		
Soft X-ray chamber	23342	0.02	7.5 - 70 kV	not suitable	3000	10500
Thimble chamber	23332	0.3	140 kV - 50 MV	(6 - 50) MeV	200	3200
Farmer chamber	30001	0.6	30 keV - 50 MeV	according to a dosimetry protocol	100	300

* at 99.5 % response saturation

The dose rate uncertainty is obtained from the uncertainty of the correction factors (therefore, including the uncertainty of the temperature and pressure measurements) and the calibration factor of the chamber, stated by the producer to be 2 - 5 %. The soft X-ray chamber was calibrated for 15 kV, 30 kV, 50 kV and for 70 kV with Al filtration of 0.05 mm, 0.55 mm, 1.05 mm and 4.04 mm, correspondingly. The other ionisation chambers were calibrated with a ⁶⁰Co γ-source. In addition to the stability and simplicity of the ionisation chambers, another advantage is that some of them can be built for use in a liquid environment. However, they have several disadvantages. First, they cannot provide energy-discriminated dose information. Second, the photon flux is integrated over the sensitive volume of the chamber, the smallest possible volume being in the order of several mm³ (with the exception of the extrapolation chamber with a variable sensitive volume). Therefore, in the case of inhomogeneous fields or if the object of interest is very small like in the case of the cell, deviations from the real dose can occur.

One possibility for spectral dose distribution determination is based on measurement of the spectral flux distribution by a semiconductor detector. The detectors and methods used for this purpose in the presented work are described in Chapter 3.3.1. In the case of sources which have a wide spectral distribution, like the X-ray tube, the spectral dose distribution can provide information on the contribution to the total dose of a certain photon energy region. This is of large interest for determination of energy-dependent RBE.

On the other hand, a system which unlike the ionisation chamber, can be used for dose determination in a very small sensitive volume, is based on the thermally stimulated exoelectron emission (TSEE) detectors. Such a system is not available commercially, but could be an alternative for dose determination in the cell. It can be used for absolute dosimetry if the detector has been calibrated for the corresponding radiation quality and geometry. The solid state detectors have additionally the advantage that they can be irradiated in water or other liquids. The simulation of the real living cell environment (the cell carrier, medium) can be also possible.

4.3 Theoretical basis of thermally stimulated exoelectron emission (TSEE)

The effect of electron emission from a material surface after exposure to ionising radiation is known as exoelectron emission, or Kramer effect. This emission can be stimulated by heating or light and can be used for estimation of the radiation exposure. The theoretical description of the effect is based on the band model of solids (Fig. 4.1). In the case of ion crystals, the radiation exposure results in a transfer of electrons from the valence band into the conduction band. If neutral defects which can accept electrons (acceptors) are present in the crystal structure and are energetically situated in the forbidden band close to the conduction band, they can accept these electrons and act as traps. The excitation presents the first stage of the two-step process of detection of radiation with solid-state detectors. The second step is the stimulation of electrons for leaving the traps. As a result, the electrons have enough energy to reach the conduction band. The presence of deep situated defects (activators) allows the electron recombination causing light emission (luminescence). On the other hand, the high energy electrons may overcome the work function and leave the crystal surface (exoelectron emission). The stimulation can be thermal, and hence the processes are called thermoluminescence (TL), or correspondingly, thermally stimulated exoelectron emission – TSEE. The optically stimulated luminescence is called photoluminescence, and correspondingly, there exists optically stimulated exoelectron emission. The thermal stimulation of the exoelectron emission is much more efficient [Les85], because, although the exoelectrons are in both cases emitted from the detector surface, the thermal stimulation can bring in motion also electrons from the depth of the material. At increasing temperature, it results in maxima of the electron emission at distinct temperatures, which are characteristic for the investigated material (glow curve). The use of TSEE detectors in dosimetry is based on the relation between radiation dose and the glow curve. The mathematical description [Hol68] of the exoelectron current in the frame of the Randall and Wilkins model is based on the following assumptions:

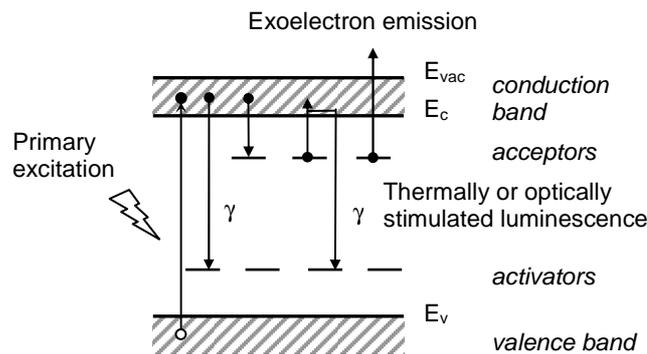


Fig. 4.1 Schematic presentation of the energy band structure of a semiconductor.

(a) The electrons in the traps have a Maxwellian distribution of thermal energies and therefore, the probability p of an electron escaping from a trap of depth E_{th} at temperature T is

$$p = S \exp\left(-\frac{E_{th}}{kT}\right) \quad (4.5)$$

Here S is called frequency factor, or pre-exponential factor, and k is the Boltzmann constant.

(b) If the re-trapping is negligible, the number of emitted electrons can be described by

$$\frac{dn}{dt} = -n(t)S \exp\left(-\frac{E_{th}}{kT}\right) \quad (4.6)$$

where n is the number of electrons in the traps at time t .

(c) When the electrons are released in the conduction band, all the electrons find their way to the vacuum level (which is very small or can be even negative); the efficiency of collecting the electrons is temperature independent and there is no accumulation of charge in the conduction band. In this case the number of exoelectron counts I is proportional to the rate of supply of electrons by the constant c :

$$I(t) = -c \frac{dn}{dt} = cSn(t) \exp\left(-\frac{E_{th}}{kT}\right) \quad (4.7)$$

The maximum of this function corresponds to the temperature T_m . If the temperature is changed linearly with time, $q = \frac{dT}{dt} = const$, by measurement at two different heating rates q_1 and q_2 , and using the temperature at the maximum of the glow curves T_{max_1} and T_{max_2} , one can easily determine the escape energy E_{th} :

$$E_{th} = k \frac{T_{max_1} T_{max_2}}{T_{max_2} - T_{max_1}} \ln \frac{q_2 T_{max_1}^2}{q_1 T_{max_2}^2} \quad (4.8)$$

On the other hand, the shape of the glow curve is obtained by solving Eq. (4.6) with the condition of a linearly changing temperature, where T_0 is the initial temperature, n_0 is the initial number of electrons in the traps and q is the heating rate:

$$I(T) = cSn_0 \exp\left(-\frac{E_{th}}{kT}\right) \exp\left(-\frac{S}{q} \int_{T_0}^T \exp\left(-\frac{E_{th}}{kT'}\right) dT'\right) \quad (4.9)$$

This expression will be used for numerical calculation of the glow curve parameters.

4.4 Applications of TSEE detectors in dosimetry

The most common materials used for TSEE dosimetry are metals or ionic crystals such as alkali halides or oxides. The ionic crystal properties can be highly improved by adding a thermal and electrical material to prevent the buildup of local charge on the emitting surface which interferes with the emitting process. One widely used detector material is BeO, because of its physical stability, thermal conductivity and insolubility in water. Its low atomic number of about 7.2 approximates the mean atomic number of tissue, making BeO especially suitable for application in personal dosimetry. A method introduced by Kramer, based on mixing of BeO with a sufficient amount of graphite powder to improve conductivity, results in a linear dose response of the detector over 6 orders of magnitude [Kra66]. This method has been further developed and improved to obtain optimal detector properties [Cra72, Hol68].

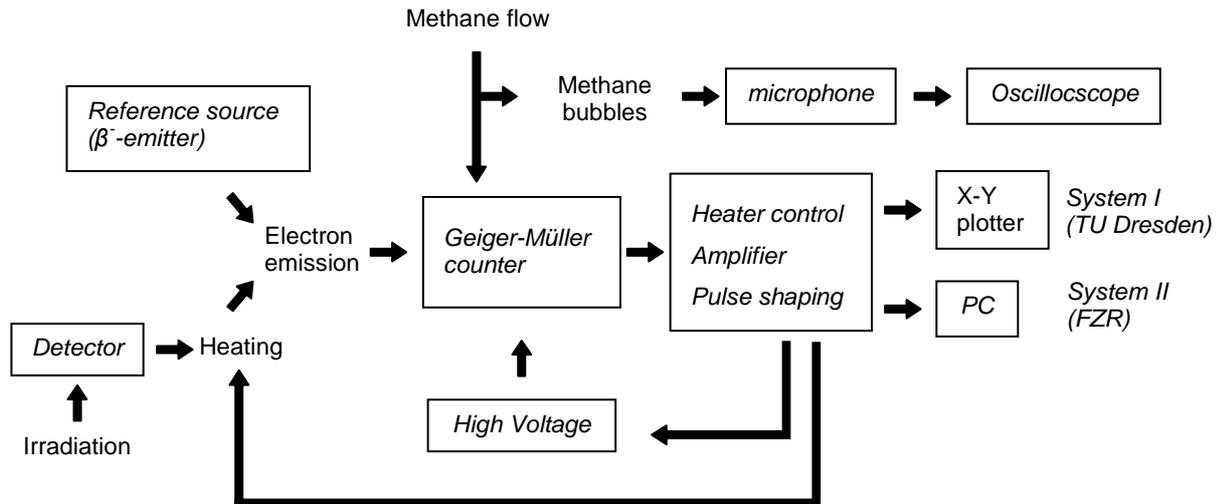


Fig. 4.2 Design of the experimental system.

The experimental investigations with BeO have proved its applicability for γ - and β -dosimetry, showing a low dependence on photon [Kri93] or electron energy [Kri86] and linearity of dose response over a large dose range [Dur91]. These are additional advantages when compared with the widespread thermoluminescent detectors (TLD). Since the exoelectrons have an escape depth of less than 10 nm [Kri86], the emission can be considered as a surface phenomenon, therefore, thin films of the emitting material are sufficient as dosimeters. This makes them very useful in cases where the small thickness of the sensitive layer is of importance, such as detection of low-penetrating β -radiation or low-energy (and therefore, highly attenuated) X-rays as well as for studying highly inhomogeneous radiation fields in the dose build-up region of high-energy photon beams or at the interface of different materials [Reg83,

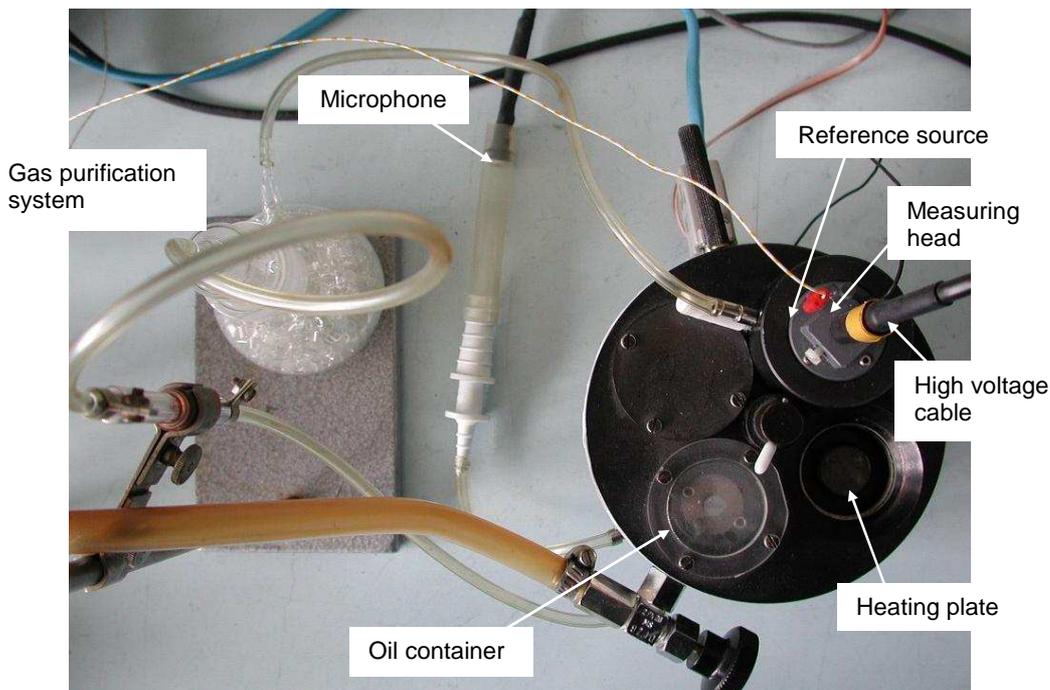


Fig. 4.3 View of the experimental setup.

Ros99]. In the study of Regulla and Leischner [Reg83], the extrapolation chamber response was compared to the response of a standard soft X-ray chamber, thick and thin TLDs and a TSEE dosimeter for an X-ray tube dose measurement at the interface between a metal and a tissue-equivalent material. It proved that the standard TLD or the soft X-ray chamber are not capable of detecting dose inhomogeneities, leaving the TSEE dosimeter to be the only alternative to the extrapolation chamber for this particular case. However, the extrapolation chambers are not easy to handle and cannot be used to measure dose in a liquid environment. Due to the advantages of the BeO TSEE detectors for assessment of dose in thin layers and in living cells, the properties of several types of detectors have been studied within this work.

4.5 Experimental studies

4.5.1 Experimental setup and detectors

In order to use the exoelectron detectors as dosimeters, the following requirements to the material must be fulfilled: (1) the induced defects have to be stable over the time; (2) the range of sensitivity must be wide, starting from a sufficiently low level; (3) the detector response has to depend on the deposited energy in the crystal in a reproducible way; (4) the response must be independent of time and conditions of storage – temperature, humidity, pressure, etc.

In this study, five types of BeO detectors were tested. The reproducibility, long-time stability of response, dose-response range as well as applicability for simulation of the cell culture environment were studied for these detectors. The components of the experimental detector system are shown in Fig. 4.2. A picture of the setup is shown in Fig. 4.3. The main part is the open gas-flow counter, which is an ionisation chamber operated in the avalanche (Geiger-Müller) voltage region, with a point anode and a working gas methane of better than 99.5 % purity. Methane was chosen due to its high counting efficiency. The gas flow is kept constant by an oil-bubble system, where the gas flows through an oil container and produces bubbles with a certain frequency. A microphone connected by a pipe to the oil container registers the sound signal from the bubbles. The amplitude and the duration of the pulses are observed on an oscilloscope. The measuring head has two positions (see Fig. 4.3), either above a β source used as a reference or above a heating plate. In the first case, electrons emitted by the source are registered, whereas in the second case the exoelectrons are emitted during the heating of the detector sample on the heating plate. The heating rate is controlled by a thermocouple. A gas purification system prevents oil drops from entering the measuring head. The detector sample, being the emitting cathode, is placed behind a circular aperture which defines the effective emission area. The point anode consists of a gold sphere of 0.27 mm diameter, located at the end of a short gold wire of 0.1 mm diameter. The emitted exoelectrons are accelerated in the high voltage of up to +5 kV applied to the anode and produce an electron avalanche. Two systems differing in pulse collection and data acquisition have been tested (both from Dr. Holzapfel Messgerätelabor, Teltow, Germany). For system I, the signal, extracted from the high voltage, is applied to a plotter and the glow curve is plotted during acquisition. This

system was available from the beginning of the experiments, and due to promising results, later system II was introduced. The electronic hardware in this case consists of an interface (comprising the high voltage unit, power supply for the heater, amplifier) and plug-in cards for controlling and data acquisition with a PC. With the help of dedicated software, the heating rate and high voltage could be changed and the data stored in ASCII-format. For system II, a guard ring serves as an electrode to pick up and transmit the counting pulses.

Table 4.2 Structure and geometry of the tested TSEE detectors.

Detector type	Structure	Shape of the substrate	Effective detector size / mm ²
I	BeO-Au-C	round	43
II	BeO-C Al holder	rectangular	144
III	BeO - C	rectangular	144
IV	BeO - C	round	79
V	BeO - C	rectangular	140

The tested five detector types differed in their structure and the method of production. The common material for all types of detectors is the exoelectron emitter BeO, as well as the graphite substrate, serving as an electrical conductor. The production methods have been developed and all detectors (except detectors type IV) were produced by Dr. Holzapfel Messgerätelabor, Teltow, Germany.

Detectors type I: First, graphite pellets (1.5 mm thick discs of about 12.5 mm outer diameter, with an inner concentric deepening of 0.5 mm and radius of about 4.3 mm) are covered with an Au layer of approximately 300 nm thickness by vapour deposition. The gold layer serves for electrical and mechanical stabilisation of the BeO layer. The Be layer of about 120 nm thickness is vapour deposited and subsequently oxidised. For highest sensitivity of the detectors, the optimal conditions are oxidation in air at 1 mbar pressure and a temperature of 1450 °C. Additional increase of the sensitivity is obtained by the reduction procedure in methane atmosphere at 5 mbar pressure and a temperature of 800 °C [Hol03].

Detectors type II: The dimensions of the graphite substrate are 12.0 × 12.0 × 0.5 mm³. The detectors are produced by the upper procedure, but without the Au layer. For mechanical stability of the detectors, they are mounted in a round Al holder.

Detectors Type III: They are basically identical with the detectors type II, but without the Al holder. Therefore, special care for handling is necessary.

Detectors type IV: The graphite pellets are 1.0 mm thick discs of 17 mm outer diameter, with an inner concentric deepening of 0.5 mm and a radius of 5.0 mm. The BeO is brought on the surface in the form of water suspension with defined concentration and the water is evaporated by heating at about 50 °C without any further treatment.

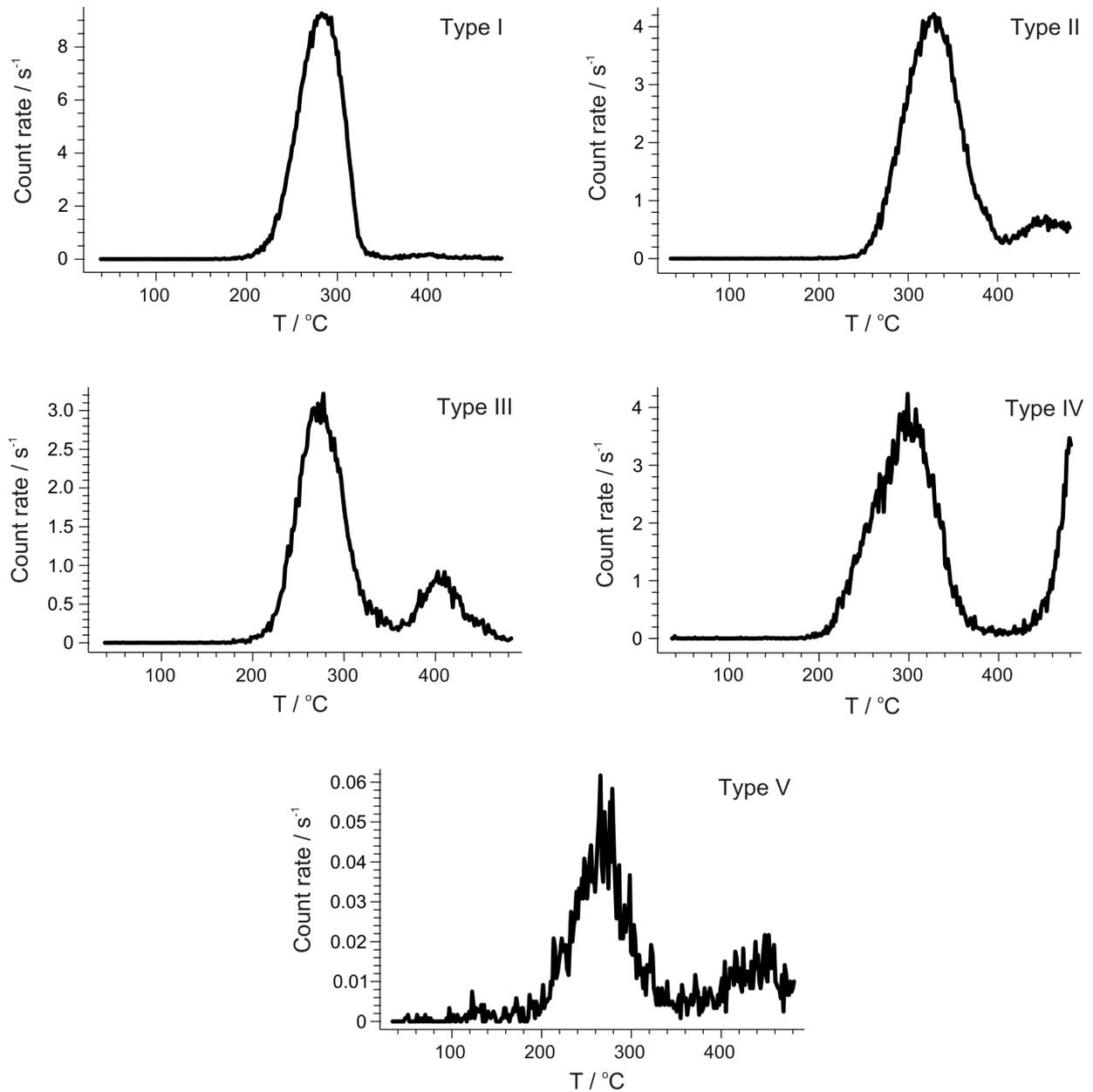


Fig. 4.4 Glow curves of all tested detector types.

Detectors type V: The graphite substrate (about $11 \times 11 \text{ mm}^2$, thickness 0.5 or 1 mm) is covered with a Be suspension in alcohol (spiritus) of a defined concentration. After evaporation, the layer is oxidised at 1400 - 1500 °C.

An overview of detector structure is shown in Table 4.2. Due to the different structure and method of production, the detectors were found out to differ in mechanical stability and handling convenience, sensitivity and reproducibility of response. This results in a difference in their applicability for absolute dose determination and dose monitoring. For example, although the electrical properties of detector type I are improved by the Au layer, the presence of a high-Z material alters the secondary electron distribution and makes absolute dose determination in cells questionable. However, due to its stability of response, after calibration in the corresponding radiation field, the detector could be used for dose monitoring. On the other hand, the simple composition and preparation procedure of detector type IV makes it attractive for absolute dose determination in cells, but an extra fragility of the BeO layer can be

also expected. The detectors type V could be expected to combine the advantages of detectors type I to III, due to the stability of the BeO layer, and on the other hand to show variable sensitivity, like detectors type IV. A difference in the glow curves can be also observed as a result of the difference in the production method. The glow curves of all detector types are presented in Fig. 4.4. They were obtained at the same heating rate of 3 K/s. The irradiation was performed with the same ^{90}Sr source and the response is normalised to 1 minute irradiation. The source-detector distance was optimised by the reader count rate and a reasonable irradiation time and was about 7 mm, varying by less than 0.5 mm for the different detector thickness. Therefore, the big difference in sensitivity observed in some detectors is mainly due to the intrinsic properties of the BeO layer. The number and the position of the peaks depend on the detector structure and production method, but most often there is one main peak in the range 200 - 400 °C, which makes dosimetric application convenient. Since both the number of counts in the peak range of the glow curve and the total number of counts are proportional to the dose, they both can be used as a dosimetric signal. The properties of the detectors were studied after irradiation with γ and β^- sources of different energy and activity, presented in Table 4.3.

Table 4.3 Sources used for the study of TSEE properties.

	Nuclides	Radiation	Energy / keV	$T_{1/2}$ / a	Activity on 15.01.2001
External sources	^{90}Sr	β^-	≤ 546	28.78	410 kBq
					20.3 MBq
	^{55}Fe	γ	5.9	2.73	130 kBq (nominal)
					37 MBq (nominal)
	^{22}Na	γ	511, 1275	2.604	58 kBq
					57 kBq
^{137}Cs	γ	662	30.07	0.1 mGy/min in water at 53.7 cm source-detector distance	
Reference sources	^{14}C (system I)	β^-	≤ 157	5715	~ 3 kBq
	^{63}Ni (system II)	β^-	≤ 66.9	100	~ 2483 Bq

The exoelectrons emitted from the surface of the detector have energy of less than 5 eV [Eic83]. Therefore, the field potential of the counter has to be high enough, so that the movement of the initial electron towards the anode produces an ionisation avalanche in the gas spreading to the cathode. The amount of the ionisation is in this case determined by the type of gas, voltage, physical dimensions and other characteristics of the chamber, but not on the ionisation of the primary electron. The determination of the working point in the Geiger-Müller region was performed for both systems I and II. The high voltage dependence of the count rate is shown in Fig. 4.5. For both counters (operated with the same methane flow rate), the working point was set to be 4.0 kV. For system II, the increase of the high voltage is connected with a change in the pulse height distribution, presented in Fig. 4.6. A peak in

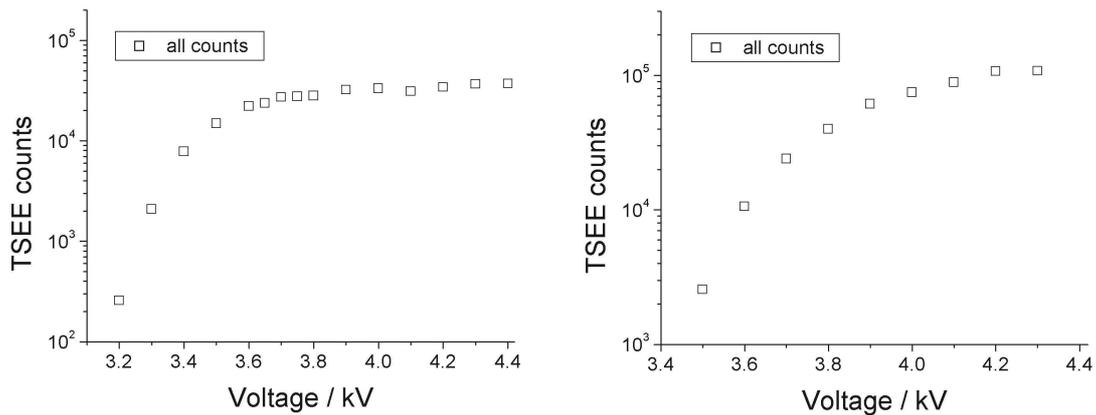


Fig 4.5 High voltage dependence of the count rate for system I (left) and system II (right). In both cases, irradiation with the same ^{90}Sr and the same detector (type I) was performed.

the distribution (called “noise peak”) was observed at channel number about 224, corresponding to about 4.4 V (the pulses in the range 0.4 - 5 V were registered). Its height was found to increase with increasing high voltage and to deteriorate the counter performance at voltage higher than about 4.1 kV. Since it was found to be at the same position even after exchange of the anode, the reason for it was probably in the electronics of the data acquisition system. Since a check of the pulse height distribution could not be performed with system I, this could not be proved. However, as presented further, the noise peak was only one of the factors influencing the whole system performance and its contribution could be neglected. It was not excluded in any of the further evaluations. As seen from Fig. 4.5 (right) and Fig. 4.6, at the working point of choice 4.0 kV, the Geiger-Müller region is reached, but the influence of the noise peak is negligible.

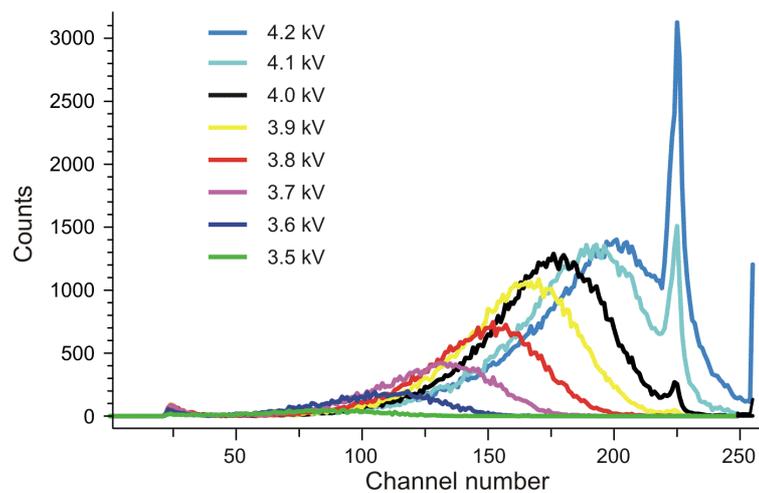


Fig. 4.6 High voltage dependence of the pulse height distribution of system II.

4.5.2 Glow curves for the different detector types, reproducibility of detector response and dose range of the TSEE system

The sample glow curves, presented in Fig. 4.4, can be used to prove the applicability of the Randall-Wilkins theory to the studied detectors. Numerical evaluation of glow curves according to Eq. (4.9) was performed, and the obtained values of E_{th} , and S are presented in Table 4.4. Mostly, this simplified theory has been proved applicable to calculation of TLD glow curves [Sun99]. The escape energy E_{th} is the energetic distance from the trap levels to the bottom of the conductivity band. The obtained values for all the detectors are in the realistic range 0.5 - 1.2 eV, whereas the frequency factor S varies from 10^5 to 10^{10} . Its physical meaning is unclear. The possible correspondence to the collision frequency of trapped electrons and the surrounding lattice atoms [Hol69], would lead to a value about one order of magnitude less than the vibrational frequency of the crystal, namely about 10^{12} s^{-1} , and is not validated in the presented case. Values lower by several orders of magnitude have been also reported for the evaluation of TL glow curves [Kin95].

The reproducibility of detector response depends, on one hand, on the system parameters, such as the stability of the high voltage, temperature and gas flow rate, and on the other hand, on the detector intrinsic properties, on the reproducibility of the irradiation parameters and the read-out geometry. Since the measurements were performed at a source-detector distance of several mm, careful detector positioning was necessary. For each system, the detectors were placed in the same source holder and irradiated so that the position and orientation of the detector surface to the source was always the same to exclude the influence of the inhomogeneity of the BeO layer. The uncertainty of the irradiation time measurement was $\pm 1 \text{ s}$.

Table 4.4 Glow curve parameters according to the Randall-Wilkins model for all detector types. The mean values from 5 experiments at different heating rates are presented together with the standard error of the mean (SEM).

Detector type	E_{th} / eV	S / s^{-1}
I	1.20 ± 0.02	$1.2 \times 10^{10} \pm 6 \times 10^9$
II	0.83 ± 0.02	$1.0 \times 10^6 \pm 5 \times 10^5$
III	1.02 ± 0.05	$9 \times 10^8 \pm 8 \times 10^8$
IV	0.81 ± 0.03	$1.6 \times 10^6 \pm 7 \times 10^5$
V	0.815 ± 0.006	$8 \times 10^5 \pm 1 \times 10^5$

For system II, the influence of the duration of operation of the system could be observed in the pulse height distribution. Although, after each TSEE measurement, a cooling block over the heater was used to prevent the whole system from heating, and the subsequent measurements were started at less than $30 \text{ }^\circ\text{C}$, after several hours of repeated read-outs the temperature of the whole system increased. This behaviour is presented in Fig. 4.7, left, where the pulse-height distribution is shown for irradiations with

the reference source over several hours of continuous operation. The steady increase of the "noise peak" at about channel number 220 and the shift of the pulse height distribution maximum to a higher voltage are not reflected by the temperature, measured at the heating plate, but only by the time of operation. Since the counter temperature was only estimated from the temperature of the heater, care was taken that temperature equilibrium was achieved.

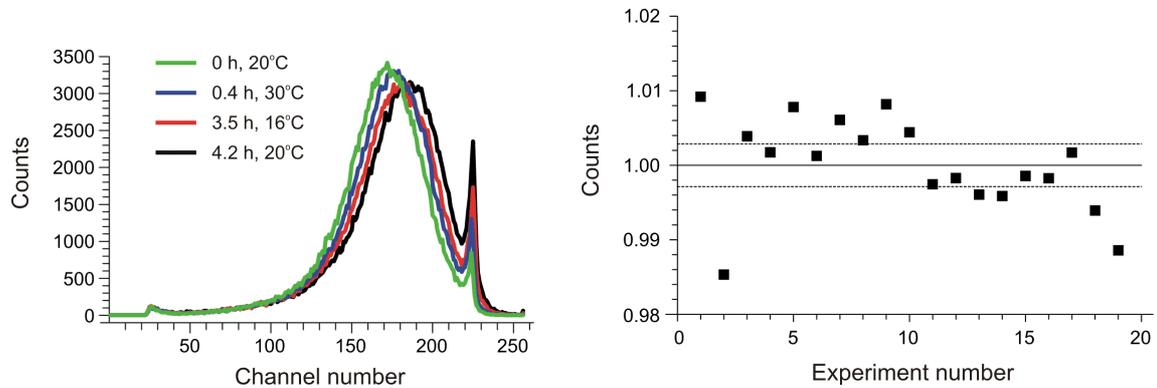


Fig. 4.7 Reproducibility of system II response, presented by the reference source irradiations. Left: temperature and operation time dependence of the pulse height distribution. Right: reproducibility of response. The solid line represents the mean value of the number of counts, the dashed lines represent the 95 % confidence interval (CI).

Another parameter which could influence the stability of the system response is the gas flow rate. It was studied for system II. A decrease in the counting efficiency with increasing gas flow rate was observed for irradiation with the reference source, whereas for the TSEE count rate, an opposite dependence was observed (Fig. 4.8). The reason for this may be the difference in the energy of the registered electrons. Whereas the maximal energy of the electrons emitted by the reference source is 67 keV, the exoelectrons have energies of several eV, so it is possible that an increase of the gas flow results in an opposite effect on the effectiveness of electron counting. However, due to insufficient information about the geometry and electronics of this prototype system, the effect cannot be explained in detail. Due to the strong gas flow dependence of the countrate, the gas flow was kept constant and controlled regularly during experiment series.

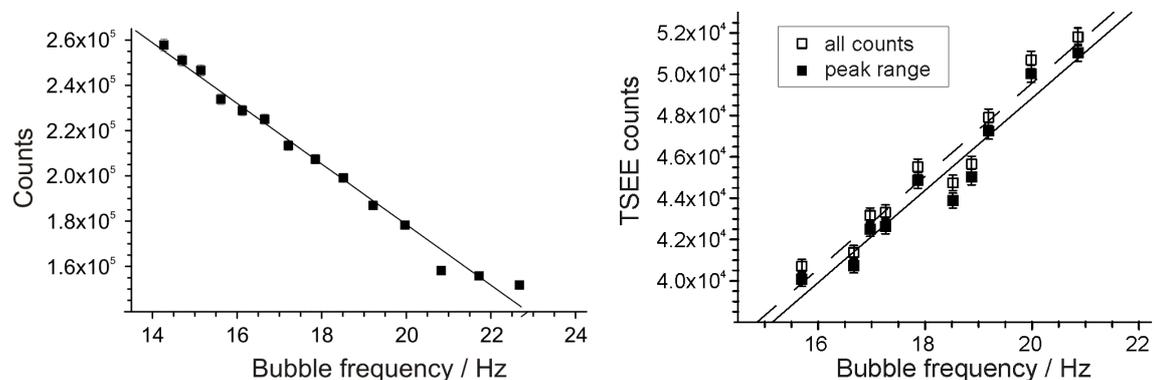


Fig. 4.8 Gas flow dependence of reference source (left) and TSEE detector type I (right) response.

The reproducibility of the reference source irradiation, measured over about 4.5 h, is presented in Fig. 4.7, right. Thus the intrinsic reproducibility of the readout system (at constant temperature and gas flow rate) was proved to be better than 0.5 % (see also Table 4.5, average deviation from the mean). The reproducibility of all detector types is presented in Fig. 4.9 and Table 4.5. The measurement and subsequent cooling was repeated at least 10 times in a row, and the total number of exoelectron counts as well as in the region of the glow curve peak were evaluated. From the average deviation from the mean, obtained as the mean of the absolute deviations, it can be seen that the reproducibility of response for the reference source alone is better than that of any of the TSEE detectors, because, as expected, it reflects only the readout system properties.

The comparison of both used systems, performed for detector type I, shows the better stability of system II properties, due to the improved high voltage stability and temperature control. The best reproducibility of response was observed for detector type I, which corresponds to the expected behaviour due to the presence of a mechanically and electrically stabilising Au layer. The worst reproducibility (more than 10 % average deviation) was observed for detectors type IV, which can be attributed to the method of production by simple sedimentation of BeO. However, these measurements do not reflect the fluctuation of the system response during routine work over weeks or months. Variations of up to 20 % were found within one week by reference source measurements, without any change of the setup or environmental conditions.

Table 4.5 Reproducibility of response for reference source and TSEE detector irradiation. The average deviation from the mean, obtained as the mean of the deviations from the average (absolute values).

Detector type	System	Number of experiments	Average deviation from the mean (peak counts) / %	Average deviation from the mean (total counts) / %
None (reference source)	II	19	-	0.50
I	I	25	0.97	0.94
	II	12	0.77	0.78
II	II	13	2.05	2.03
III	II	12	1.92	1.80
IV	II	10	9.22	10.5
V	II	10	4.72	4.47

The dependence of the number of TSEE counts on the time of irradiation, or, respectively, dose, has been studied for both systems and different sources. In Fig. 4.10, the detector response in dependence on irradiation time for system I and two different sources is shown. As seen from the figure, the

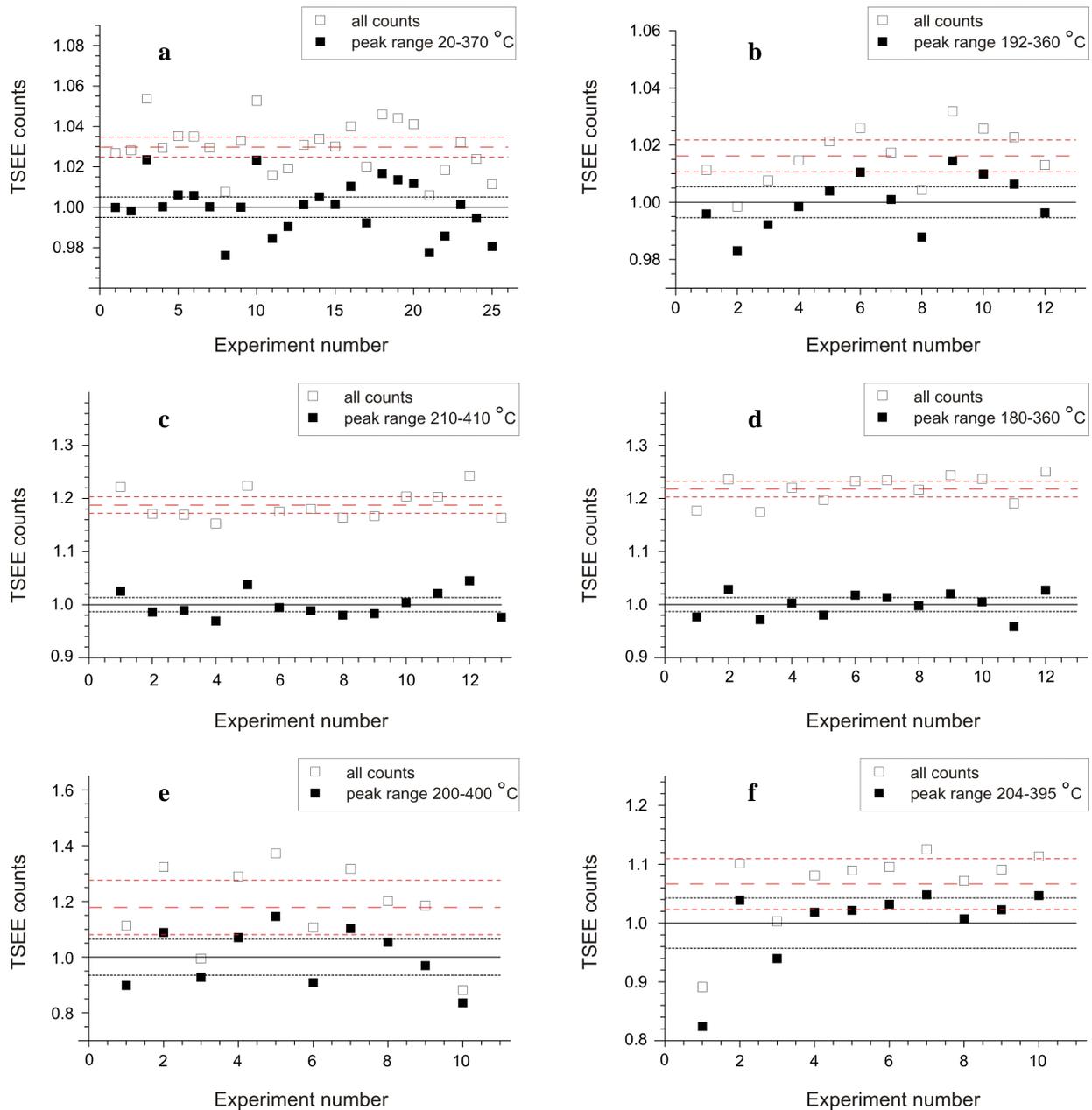


Fig. 4.9 *Reproducibility of detector response to repeated irradiations with a ^{90}Sr source. a: detector type I, system I, b: detector type I, system II, c: detector type II, system II, d: detector III, system II, e: detector type IV, system II, f: detector type V, system II. The number of TSEE counts in the peak range as well as the total number of counts are normalized to the mean number of counts. The corresponding 95 % CI for each graph are shown by a set of two lines, whereas the black lines represent the peak range, and the red lines represent the total counts.*

linearity of response is held for soft X-rays as well as for β -rays. It was observed also after irradiation with the ^{137}Cs source and other types of detectors. This makes calibrated detectors useful for dose determination. However, after longer irradiation times, a saturation in the count number was observed for detectors type I, II and III for both systems, which could show either saturation of the detector response, or result from the limited pulse rate resolution of the counter. This was proved by comparing

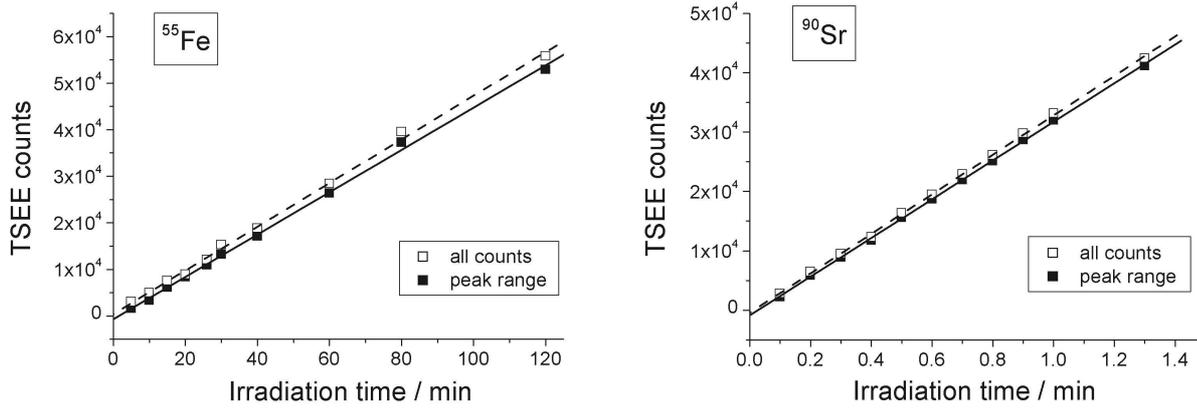


Fig. 4.10 Dose response of detector type I, system I. The solid squares represent the peak range (20 - 370 °C) with the corresponding linear fit (solid line). The open squares represent the whole range (20 - 520 °C) with the corresponding linear fit (dash line). Left: ^{55}Fe irradiation. Right: ^{90}Sr irradiation.

the response of two different detectors after irradiation with the same source and the same irradiation geometry. The results of irradiation with a ^{90}Sr source for system I, detectors type I, are presented in Fig. 4.11, left. Although both detectors have different sensitivity, reproduced by the different slopes of the linear range of the curves, the saturation of response is achieved at the same count number, about 5×10^5 total number of counts. Saturation at a similar number of counts was also observed for system II. Therefore, saturation due to the counter resolution was concluded.

In order to determine the dose range, corresponding to the count rate of the TSEE systems, a ^{137}Cs source was used. It was calibrated to dose rate in water of 0.1 mGy/min at a 53.7 cm distance from the source, the minimal possible distance being about 6 cm. The determination of the sensitivity region for

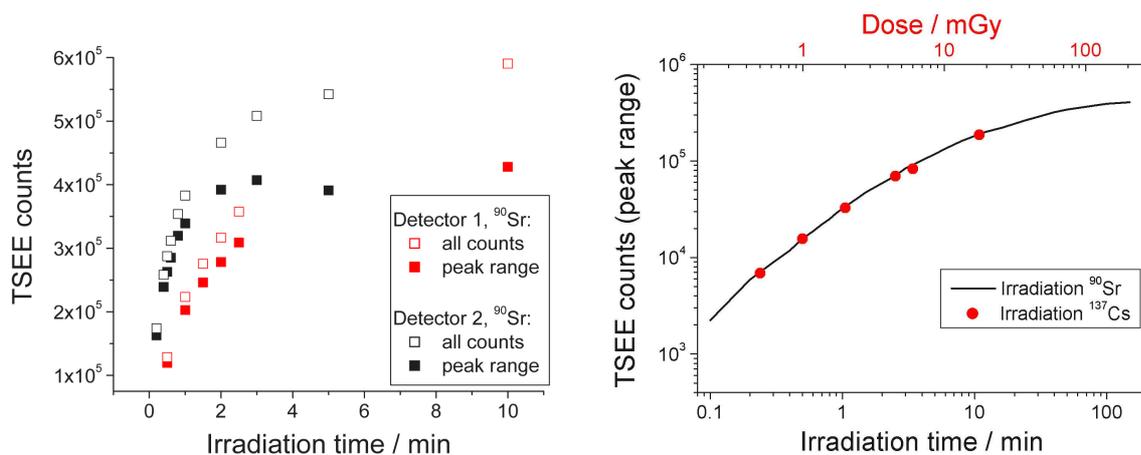


Fig. 4.11 Left: saturation of system I response, measured for detectors type I after irradiation with ^{90}Sr . Right: dose response curve of detector type I, system I. The response after irradiation with ^{90}Sr is shown by the solid black line. The red circles represent the response after irradiation of the same detector with a calibrated ^{137}Cs source.

detector type I and system I is shown in Fig. 4.11, right. In order to present the saturation region, which is limited by the counter resolution, the response after irradiation with the ^{90}Sr source was scaled to fit the response curve after ^{137}Cs irradiation for the same number of counts. This procedure is not equal to a “calibration” of the ^{90}Sr source, since the difference in detector response to both radiation qualities is unknown. From the figure, the dose range of system I is obtained to be 2 orders of magnitude, where the upper limit is defined by the counter saturation, being about 10 mGy, and the lower limit is defined by the statistical error of the count number. The upper value is far from the reported saturation limit of the detectors of up to 10 Gy [Kri86], and the entire sensitivity range is far from the dose range necessary for cell irradiation, which is usually 0.1 - 10 Gy. However, this is important only for dose monitoring, because dose inhomogeneity does not depend on the used dose range and the measurement is also possible using low-dose irradiations. A shift in the TSEE system sensitivity could be achieved by manipulation of the read-out system (counter geometry, gas flow), which however would result in a rather small increase of the upper response limit. A decrease of the detector sensitivity by orders of magnitude can be reached by decreasing detector size, but since a tenfold decrease of the detector radius, resulting in 100 times sensitivity decrease, would result in a detector size less than 1 mm^2 , it would lead to difficulties in the production and handling of such detectors. Another possibility would be to decrease the size of the irradiated detector area. This method was tested using a grid over the detector, but it resulted in decreased stability of response. Therefore, another method of detector production was used and detectors type IV and V, produced by sedimentation, were tested.

Although detectors type IV can be produced in very simple laboratory conditions by sedimentation of BeO water suspension on a graphite substrate, their testing proved that no big variation in sensitivity could be achieved. A fading effect was observed, expressed in several orders of magnitude drop of the response to irradiation on the first days after production (Fig. 4.12). The detector response was evaluated immediately after irradiation with a ^{90}Sr source, and the procedure was repeated on several consecutive days. After response stabilization, the reproducibility was proved to be about 10 % (see Table 4.5). Such changes in response were not observed for any other detector type. For detectors type V, which were produced in a similar way, several orders of magnitude difference in sensitivity was achieved by variation of the BeO amount during production, and the sensitivity was proved to be stable with time. The dose ranges possible to be measured with the tested TSEE detector types are presented in Table 4.6. For detector types II - V, since no measurement with the calibrated ^{137}Cs source was performed, the dose range was obtained under the assumption that the response ratio of all detectors to the γ -irradiation with the ^{137}Cs and the ^{90}Sr source is identical. In order to obtain the upper dose limit, a saturation of the counting system was assumed to occur at 5×10^5 counts. As seen from Table 4.6, the variation in sensitivity for detector type V is sufficient to achieve upper dose limits reasonable for cell irradiations.

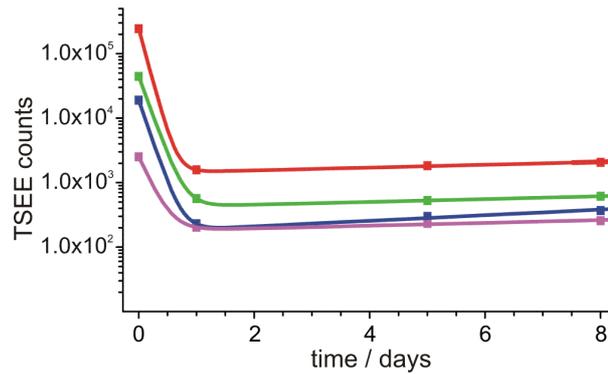


Fig. 4.12 Fading effect for detector type IV (a single detector response is represented by closed symbols, fitted by a two-parameter exponential model for better presentation).

Table 4.6 Sensitivity of all studied detector types. Detector types II - V have been studied only with system II.

Detector type	TSEE system	Sensitivity / counts mGy ⁻¹	Upper dose limit / mGy
I	I	14250	35
	II	7595	66
II	II	4883	102
III	II	6247	80
IV	II	5548	90
V (low)	II	48	1.0 × 10 ⁴
V (medium)	II	6246	80
V (high)	II	29870	17

4.5.3 Dose measurement in a simulated cell environment

The irradiation of living cells is complicated by the requirement of optimal environmental conditions, and especially by the presence of appropriate liquid (e.g. cell culture medium) covering the cells. Therefore, the application of TSEE detectors for dose sampling in the conditions of real cell environment and the study of interface effects would require irradiation in the presence of liquid. All studied detector types were tested for applicability for this purpose. The tested liquids were water, propanol and cell medium. Water and propanol were chosen for their simplicity of chemical composition, propanol being expected to be closer to the cell medium. The irradiation in water resulted in big and inconsistent variations of the detector response. The irradiation in cell culture medium resulted in a complete change of the glow curve and inadequate detector response, caused probably by the influence of the organic constituents on the electric properties of the irradiated surface, however, no irreversible change of the detector behaviour was observed. Finally, propanol was chosen as a working medium due to its low atomic number and fast evaporation which allows immediate evaluation of the

glow curve. The summary of the detector performance for system II is presented in Table 4.7. First, a well known problem for detectors based on surface excitations is the tribo-effect, expressed in detection of a signal after a contact of the surface with any material without irradiation. In addition, the presence of the liquid could affect the electrical properties of the BeO layer and lead to a change of the signal. The induction of the tribo-effect was checked by wetting the detector, drying and subsequent irradiation. No change of the detector response, which would point at a tribo effect, was observed after contact of the detector surface with propanol (see Table 4.7, column 2). As a second step, the study of the influence of the liquid on detector response was performed using the setup presented in Fig. 4.13. The source was placed directly on the detector only if it was not coming in contact with the sensitive layer of the detector, otherwise a holder was used. The thickness of the liquid layer was 1 - 3 mm. The reproducibility of response of all detector types was proved to be worse compared to irradiation in air (cf. Table 4.5). The consistence of detector response for irradiation in propanol was checked with a ^{22}Na source. The positron decay of ^{22}Na leads to annihilation radiation at 511 keV in addition to the decay γ -line at 1275 keV, therefore, for the distances used in the experimental setup, a decrease in photon intensity due to attenuation and scattering in the liquid layer of 1 - 2 % is expected. A ^{55}Fe soft X-ray source was used for comparison, and in this case the change in response was expected to depend only on detector geometry and follow the attenuation of the soft X-rays in the propanol layer. The results for the ^{22}Na irradiation, presented in Table 4.7, column 3, show that for all detector types except detector type I the ratio of the response after irradiation in air and propanol is higher than expected, probably due to influence of the liquid on the surface properties. The response ratio after irradiation in air and propanol with the ^{55}Fe source is expected to be, estimated from the source and detector geometry, in the range from 48 to 97. As seen from column 6 in Table 4.7, the response ratio for all detectors is close to the expected one, taken into account the large uncertainty resulting from the detector positioning, homogeneity of the sensitive layer and detector to source distance.

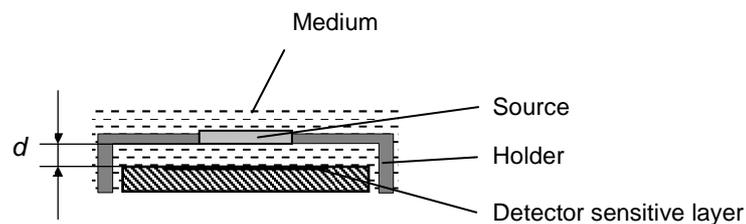


Fig. 4.13 Setup for TSEE detectors irradiation in liquid.

The studied TSEE detector systems clarify the potential of TSEE detectors for determination of dose in complicated cases. The obtained results show that the detector response depends on the structure and method of production, however, a stable response in laboratory conditions can be easily achieved. This makes them suitable for measurement of dose in thin layers as well as of dose inhomogeneity at material interfaces. Since the best reproducibility of less than about 2 % was obtained for detectors type I - III, they can be used in cases, when such precision is necessary. The dose range, in which the

Table 4.7 Influence of the irradiation medium on TSEE detectors response. The mean values for the TSEE peak from 3 - 12 experiments are shown together with the corresponding 95 % CI.

Detector type	Response ratio after and before propanol wetting (^{90}Sr)	Reproducibility* in propanol / % (^{22}Na)	Response ratio air to propanol (^{22}Na)	Spacing d / mm (^{55}Fe)	Response ratio air to propanol (^{55}Fe)
I	1.00 ± 0.05	10.8	0.92 ± 0.08	2.3	32 ± 2
II	1.02 ± 0.07	8.8	1.18 ± 0.09	2.4	59 ± 9
III	-	16.0	1.26 ± 0.19	2.8	131 ± 11
IV	-	13.8	1.6 ± 0.2	-	-
V	-	15.3	1.4 ± 0.3	-	-

*Deviation from the mean, presented as the average deviation from the mean for the TSEE peak range

studied TSEE system can be used, was found to be limited by the counter resolution, but by a variation of detector sensitivity, the whole dose range of interest for radiobiological experiments can be covered. This makes the system suitable for absolute dose measurement with calibrated detectors during routine irradiation, however, the system performance is limited by the variation in the system response for time periods longer than several hours. The irradiation in a simulated cell environment was successful only for detectors type I. This type, however, is least tissue-equivalent, which makes the comparison to dose distribution in a cell difficult. Although the TSEE detectors could be of big interest for dosimetry at the ELBE X-ray source, it requires improvement to become suitable for precise dose determination. At the first stage of measurements at the ELBE X-ray beam, the studied TSEE system was not used.

5 Establishment of the biological objects and endpoints

5.1 Cell lines and biological endpoints

The experimental object and the biological endpoint used in a radiobiological study have to correspond to the area of application of the results and to be suitable for extensive studies. Since the RBE depends on the cell line and the endpoint used, more than one cell line-endpoint combination is necessary. In the frame of a joint DFG project [DFG99] together with the Medical Faculty of Dresden University of Technology, experimental studies with several human and rodent cell lines were performed [Slo03, Pan03]. These were human fibroblasts HFIB and neonatal keratinocytes HEK_n, as well as mouse fibroblasts NIH/3T3 and Chinese hamster fibroblasts V79. For these cell lines, the RBE of 25 kV X-rays was determined relatively to 200 kV X-rays, for cell survival [Pan03] and micronuclei induction [Slo03]. The clonogenic assay is a standard endpoint, reflecting the clonogenic cell death, whereas the micronucleus test allows to assess chromosomal damage. Two of the cell lines were found to be inappropriate for both assays, due to high sensitivity to the substances used in the micronucleus test (V79) or inability for clonogenic growth (HFIB). Another cell line, HEK_n, was found too difficult in handling to be appropriate for extensive long-term experiments. Therefore, in order to establish these radiobiological endpoints at ELBE and to continue the studies, only one of the previously used cell lines, the widely used mouse fibroblasts NIH/3T3, was taken. In addition, due to the possible implementation of the RBE values of soft X-rays for risk determination of mammography, human breast epithelial cells MCF-12A have been used. These established cell lines are suitable for long-term culture and turned out to be relatively robust. For both cell lines, the conditions for the two radiobiological assays have been optimised. Since they are transformed, but not tumourigenic in immunosuppressed mice, the experimental results can clarify the response of normal tissues to radiotherapy when X-rays of the corresponding energy range are applied.

In order to reduce the influence of stress factors during a long transport way, a cell culture laboratory in the accelerator building and in immediate vicinity of the ELBE X-ray beam and the reference X-ray tube has been established. It is suited for all kind of cell culture procedures which require sterile conditions and controlled environment and therefore cannot be performed in a usual laboratory. For cell growth in the presence of oxygen as well as under hypoxic conditions, two incubators Binder CB-150 (Binder, Tuttlingen, Germany) have been installed, with a possibility of connection to CO₂, O₂ or N₂. For cell processing under sterile conditions, a laminar-flow bench Herasafe HSP 12 (Kendro, Hanau, Germany) is provided. An inverted microscope Axiovert S 100 (Carl Zeiss, Göttingen, Germany) for brightfield, phase contrast and fluorescence light is used for observation of living as well as fixed cells. All these devices are necessary to prepare the probes, as well as to process them immediately after irradiation, whereas all following steps of damage evaluation on fixed cells can be performed more conveniently outside, also in one of the well-equipped biological laboratories in FZR.

5.1.1 Cell culture

Both cell lines were purchased from ATCC (Manassas, USA). The mouse fibroblasts NIH/3T3 (Cat. No. CRL-1658) were taken earliest at passage 126, for the human mammary epithelial cell line MCF-12A (Cat. No. CRL-10782) the starting passage was unknown.

The mammary gland epithelial cell line MCF-12A is a non-tumourigenic epithelial cell line established from a patient with fibrocystic breast disease that contained focal areas of intraductal hyperplasia. The line was produced by long-term culture in serum free medium with low Ca^{++} concentration. The cells exhibit typical luminal epithelial morphology. MCF-12A was derived from adherent cells in the population, by a transformation resulting from a 72 h exposure to 45 °C [Pai92]. The cells were incubated at 37 °C in humidified atmosphere containing 5 % CO_2 , in a one to one mixture (Cat. No. FG4815) of Dulbecco's modified Eagle's medium (DMEM) and Ham's F12 medium, supplemented with 5 % horse serum (Cat. No. S9135) (all from Biochrom, Berlin, Germany), 500 ng/ml hydrocortisone (Cat. No. H0135, Sigma, Saint Louis, USA), 0.01 mg/ml insulin (Cat. No. I1882, Sigma), 100 ng/ml cholera toxin (Cat. No. 227035, Calbiochem, San Diego, USA) and 20 ng/ml epidermal growth factor (Cat. No. 354010, Becton Dickinson, Franklin Lakes, USA). Passages 6 to 20 after initiating the culture were used in the experiments. For detaching of MCF-12A a solution of 0.25 % trypsin (Cat. No. L2103) and 0.03 % ethylenediaminetetraacetic acid (EDTA) (Cat. No. L2113) in phosphate buffered saline (PBS) (Cat. No. L1825) was applied for 10 min at 37 °C (reagents from Biochrom). Afterwards, the cells were centrifuged at 1000 rpm and 4 °C for 10 min, and seeded at a density of about 6000 cells/cm².

The mouse fibroblast cell line is a continuous cell line of highly contact-inhibited cells. It was established from the NIH Swiss mouse embryo cultures. The established NIH/3T3 line was subjected to more than 5 serial cycles of subcloning in order to develop a subclone with morphologic characteristics best suited for transformation assays [Jai69]. The cells were cultured at 37 °C in humidified atmosphere at 5 % CO_2 and 95 % air in DMEM (Cat. No. FG0435) supplemented with 10 % fetal calf serum (Cat. No. S0115), 1 mM sodium pyruvate (Cat. No. L0473), 1 % v/v non-essential aminoacids (Cat. No. K0293), 20 mM 4-(2-hydroxyethyl)-1-Piperazineethanesulfonic acid (HEPES buffer) (Cat. No. L1613), 100 U/ml penicillin, 100 µg/ml streptomycin (Cat. No. A2213) (all reagents from Biochrom). Subculturing of the cells was performed with a trypsin/EDTA solution 0.0125 % / 0.001 % in PBS (Cat. No. L2163, Biochrom) at 37 °C for 4 min. After resuspending, the cells were centrifuged at 800 rpm and 4 °C for 5 min and seeded at a density of about 8000 cells/cm². Passages 7 to 26 after initiating the culture were used in the assays.

The cells were grown in culture flasks with a base area of 25 cm² (Nunc, Wiesbaden, Germany, or Greiner, Frickenhausen, Germany), containing 5 ml of cell line specific medium. For both cell lines, media were changed every 2 - 3 days, and the cells were subcultured before they reached 70 % confluence.

5.1.2 Biological endpoints

The clonogenic survival assay [Puc56] is a well established technique for determination of cell proliferation capability. It is widely applied in radiotherapy for determination of clonogenic cell survival since it is sensitive in the dose range applied in radiotherapy, about 2 Gy being the standard dose per fraction. However, this assay is insensitive to transformation in the surviving cells, which is the problem of interest in the cancer risk estimation. In the present experiments, cells were seeded in the culture dishes where the irradiation was to be performed and were incubated for several days. The monolayer culture was irradiated in the exponential growth phase, before reaching 70 % confluence. Immediately after irradiation, cells were trypsinized and seeded as single cells at low density in Petri dishes, with 6 - 10 replications per dose point. After an incubation time of 12 days (MCF-12A) or 12 - 14 days (NIH/3T3) the colonies were fixed with ethanol and stained with crystal violet. Colonies of more than 50 cells were scored as survivors. For continuous cell lines, the plating efficiency is not decreasing with the passage number. However, it can strongly vary in dependence on the growth medium components and the culturing conditions. One very important factor is the serum, which has undefined composition and different results can be obtained from different charge numbers even if it is purchased from the same company. Usually, several batches of serum are tested and the one providing the highest plating efficiency is taken. The investigations of plating efficiency results for both cell lines will be presented in Chapter 6. The total number of cells needed for this assay depends on the expected plating efficiency and radiosensitivity of the cells. The numbers are optimised so that about 100 colonies per dish are scored in all dishes. Thus, for an expected survival of 1 % at the highest dose and at a plating efficiency of 50 %, for 6 replications at least 1.2×10^5 cells have to be present in the irradiation dish at this dose. At the confluence of about 70 %, at which the clonogenic assay is performed, the cell density is about 4×10^4 cells/cm² for NIH/3T3 and 2×10^4 cells/cm² for MCF-12A, which corresponds to a reasonable dish diameter of 2 cm for NIH/3T3 and 3 cm for MCF-12A. However, if a lower plating efficiency is expected or if there are losses at trypsinisation, the number of dishes at the higher doses have to be increased. These values have to be taken into account when choosing an irradiation dish, since a compromise has to be made between the required dose rate (and correspondingly the time of irradiation), dose homogeneity and number of probes to be irradiated.

Micronucleus (MN) formation as a result of irradiation is a well-known effect, first used for verification of radiation damage in the 1960-s. The doses applied in radiation diagnostics are usually in the mGy range, which is beyond the sensitivity of most radiobiological assays. The DNA damage formed as a result of the ionising particle passing the cell is translated into structural chromosomal aberrations. The micronuclei are formed from chromosome fragments or even whole chromosomes as a result of chromosome breakage or dysfunction of the mitotic apparatus. During the cell division, some of them are excluded from the daughter nuclei and form small extra nuclei, either on their own, or in conjunction with other fragments. They are formed within the cytoplasm of either one, or both, daughter cells. Therefore, cell division is a necessary condition for their production, and the MN

frequency will be expected to increase with time after irradiation as more and more aberration-bearing cells pass through mitosis. Depending on the origin of the excluded fragment, both, or only one daughter cell will suffer genetic loss. The fate of cells with micronuclei is still unknown, although it has been suggested that the micronuclei can be eliminated from the cells, included in the nucleus in mitosis or lead to cell death. Therefore, if the daughter cell continues to proliferate, the observed frequency will not correspond to the primary damage. In order to distinguish the generations, the cell cycle has to be exactly observed. The MN scoring has been successfully applied in human lymphocytes due to the spontaneous synchronisation of these cells in culture. However, in order to apply it for other cells, a modification of the assay was necessary to distinguish between the cell generations. A bromodeoxyuridine staining protocol [Pin84] as well as an autoradiographic technique have been suggested [Fen85], but finally a simple treatment with cytochalasin B was the method of choice [Fen85]. The cytokinesis-blocking agent cytochalasin B does not affect karyokinesis (the separation of the daughter nuclei) and as a result, binucleated cells (BNC) appear, so that it is then easy to distinguish the cells that have passed exactly one division (see also Fig. 5.1). This method has been successfully applied to human lymphocyte as well as fibroblast cultures. For the present work of evaluation of radiation damage, all cells (irradiated and non-irradiated) were fixed at the same time, therefore, in order to evaluate a possibly high number of heavily damaged cells and at the same time to harvest the weakly damaged cells before they continue into the next mitosis, the incubation time with cytochalasin B was optimised for each cell line. Furthermore, a concentration below the limit of cell toxicity had to be also found for each cell line.

Table 5.1 Micronucleus test parameters for the two cell lines used in this work.

Cell line	Seeding density / cells cm ⁻²	Cytochalasin B concentration / µg ml ⁻¹	Incubation time / h
NIH/3T3	5000	1.5	24
MCF-12A	2500	1.5	48

The optimised parameters for the micronucleus test for both cell lines are shown in Table 5.1. In the presented experiments, the cells were seeded in Petri dishes at 3 replications per dose point and incubated at 37 °C for 24 h. This allows good attachment and prevents interference of the trypsinisation treatment with the irradiation effect. Immediately after irradiation, the medium was changed to one containing cytochalasin B and the cells were returned into the incubator for 24 - 48 h. After incubation, the cells were washed with 0.9 % NaCl and fixed with ice cold methanol. The staining was performed with Giemsa solution in water. The cells were observed under a light microscope and the fraction of BNC, as well as the fraction of BNC with MN, the number of MN per BNC and the number of MN per MN-containing BNC were determined. For the identification of the micronuclei, the criteria of Fenech [Fen93] were used: (1) the MN have a diameter between 1/16 and 1/3 that of the main nuclei, (2) MN

are non-refractile, (3) they are not linked to the main nuclei via a nucleoplasmic bridge, and (4) MN may sometimes overlap the boundaries of the main nuclei. In addition, the scored cells were satisfying the following criteria [Fen93]: (1) the cell cytoplasm is intact (2) the cell has two nuclei of approximately equal size, which could overlap slightly or touch each other over the edges and be attached by a fine nucleoplasmic bridge, (3) the cell has no more than 6 MN. In this assay, the total number of cells needed is limited from the doses applied and expected fraction of BNC at the highest dose. For each dish, a total number of 200 BNC is evaluated, which at a BNC fraction of 20 % at the highest dose means at least 1000 cells. However, in order to fulfil the conditions for MN scoring, some cells have to be excluded, so an additional factor of about 2 has to be taken into account. In order to have well separated single cells in the dish, NIH/3T3 and MCF-12A are seeded at a concentration of 5×10^3 cells/cm² and 2.5×10^3 cells/cm², respectively, which corresponds to a reasonable dish diameter of 0.7 cm for NIH/3T3 and 1.4 cm for MCF-12A for this assay.

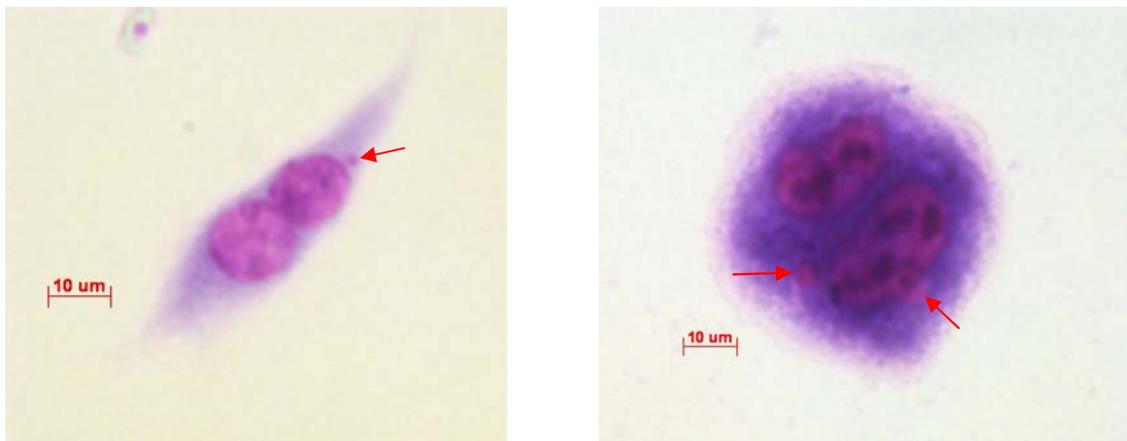


Fig. 5.1 Microphotographs of a binucleated cell with micronuclei (shown by the red arrows). Left: NIH/3T3 mouse fibroblast, right: MCF-12A human mammary epithelial cell.

5.2 Preparation for irradiation at the ELBE X-ray beam

In the radiobiological studies, mostly the irradiation is performed using a radioactive source or an X-ray tube. For attached cells, a vertical beam and irradiation in a culture flask or Petri dish are the most appropriate. However, the geometry and spectral characteristics of the source do not always allow such conditions, and alternative solutions have to be found.

5.2.1 Irradiation geometry

The irradiation at the ELBE X-ray beam has some peculiarities, coming, on the one hand, from the irradiation conditions, and on the other, from the cell culture conditions. First, the horizontal X-ray beam requires a vertical position of the cell layer. In order to avoid cell drying and therefore, death, the cells have to be placed in a dish filled with culture medium. Additionally, the culture dish has to be filled and sealed under sterile conditions and to be kept sterile until the final step of cell fixation (for the

clonogenic assay, this is about 2 weeks after irradiation). Therefore, great care has to be taken not to compromise the sterility of the medium. Another limitation comes from the X-ray energy region which is studied. The cross section for photoeffect, which is the main interaction process in the soft X-ray range, increases strongly with decreasing X-ray energy (see Chapter 2). Therefore, in order to minimise the attenuation, the cells have to be grown and irradiated on a thin membrane. The size of the target area is also limited by the X-ray beam properties. As outlined in Chapter 3, there exists a relation between CR energy and spatial intensity distribution at the target position, limiting the size of the irradiation dish. As already discussed, the irradiation dish size is depending also on the endpoint and the cell type. In order to fulfil as far as possible all requirements, the following setup has been chosen for the cell irradiation (Fig. 5.2). Small vessels are commercially available with polystyrene walls and a bottom made of thin foil – these are tissue culture inserts, used for organotypic cell culture or co-culture. Sealing is performed with Parafilm M (Merck, Darmstadt, Germany).

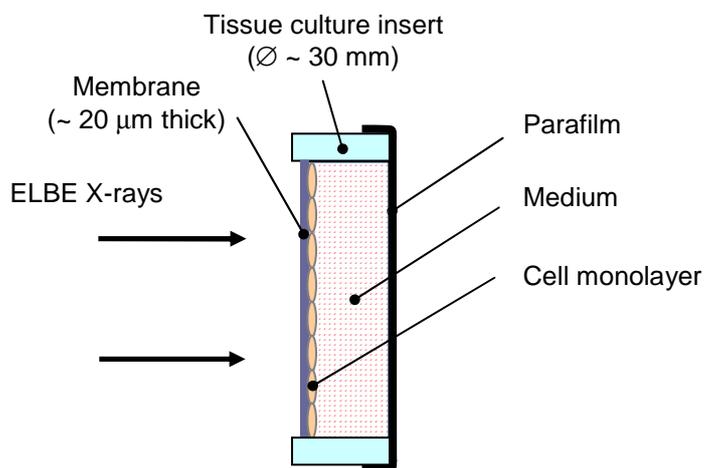


Fig. 5.2 Schematic presentation of the cell culture vessel positioned for irradiation in the ELBE X-ray beam.

5.2.2 Choice of membrane material

Several membrane materials have been tested as possible substrate materials. First of all, the membrane has to meet the requirements of the cell culture, but also to be stable and impermeable for culture medium. Each cell line has to be tested for good attachment, for undisturbed cell growth and lack of influence on the control parameters of the performed tests. The optical properties of the membranes are important since it is helpful to observe the cells during their growth under a phase-contrast microscope. On the other hand, while the survival test requires no staining of cells directly on the membrane surface, for the micronucleus test, in order to minimise the stress on the irradiated cells, they are fixed, stained and observed under the microscope directly in the dish where they were irradiated. Therefore, this test requires very good transparency of the membrane.

The tested membrane materials and their main physical properties are presented in Table 5.2. All tested

tissue culture inserts had polystyrene housing, a diameter in the range 12 - 30 mm and height from 6 to 12 mm. No difference in the handling was found. As the first tested parameter for the choice of the tissue culture insert, the growth of the cells as monolayer on the membrane base was used. The NIH/3T3 cells were used for this test. As shown in Table 5.2, only 3 of the tested membrane bases provided good growth of NIH/3T3. However, the tissue culture inserts produced by Iwaki were not permanently available, so no further tests were possible, despite of the promising first results. Due to the encouraging result for cell growth, obtained with the tissue culture insert based on the Isopore membrane, additional procedures to still improve the cell spread were applied.

Table 5.2 Membrane properties of some tissue culture inserts. The growth of NIH/3T3 was determined as: bad (no attachment of the cells), good (cells attached, but forming aggregates larger than 100 μm), very good (the aggregates are smaller than 100 μm) or excellent (a homogeneous monolayer is formed).

Producer	Membrane material	Pore size / μm	Membrane thickness / μm	Optical properties	Growth of NIH/3T3 cells as monolayer
Nunc	Anopore	0.02	45	transparent when wet	bad
Nunc	Anopore	0.2	45	transparent when wet	bad
Nunc	polycarbonate	0.4	20	not transparent	bad
Nunc	polycarbonate	3	17	half-transparent	bad
Iwaki	polycarbonate	0.4	no data	not transparent	good
Iwaki	PTFE	0.4	no data	transparent when wet	bad
Millipore	PTFE	0.4	no data	transparent when wet	bad
Millipore	Isopore	0.4	6 - 10	not transparent	bad
Millipore	Isopore, tissue-culture treated	0.4	6 - 10	not transparent	good / very good*
Sartorius	Biofolie	no pores	25	glassy	excellent

**additional treatment for better cell adhesion: poly-L-lysine or collagen*

The best obtained results of NIH/3T3 cells growing on membranes are shown in Fig. 5.3, where Isopore and Biofolie are compared to the standard polystyrene culture flask. Since the Isopore membrane was not transparent enough to allow observation of living cells with a phase contrast microscope, all probes were stained with crystal violet. In Fig. 5.3a, a cell monolayer grown on Isopore without pre-treatment is presented. In Fig. 5.3b, the result after an overnight pre-treatment of the Isopore membrane with collagen (rat tail collagen I, Cat. No. Z17C03-B, Cell Concepts, Umkirch, Germany, final concentration 36 $\mu\text{g}/\text{cm}^2$) is presented. In Fig. 5.3c, the NIH/3T3 cells growth on poly-L-lysine pretreated tissue culture inserts is presented (the poly-L-lysine solution, purchased from Biochrom, was applied at a final concentration of 20 $\mu\text{g}/\text{cm}^2$ overnight). The cell growth on both treated surfaces is reg-

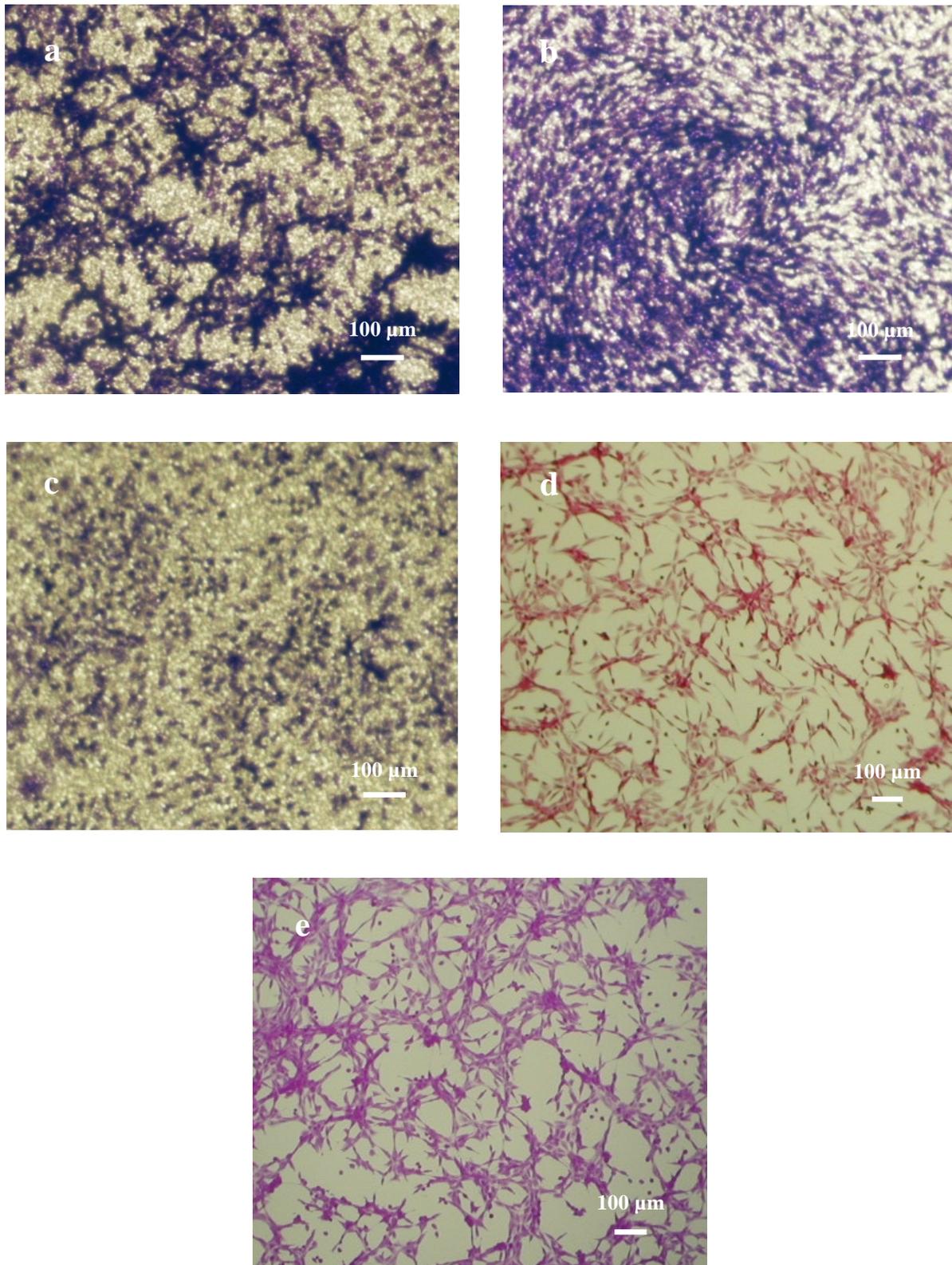


Fig. 5.3 Microphotographs of growth of NIH/3T3 as monolayer on different material. The cells are fixed and stained with crystal violet. *a, b, c:* Isopore, tissue-culture treated, pore size $0.4\ \mu\text{m}$, seeded $12000\ \text{cells}/\text{cm}^2$, 72 h incubation, where *a:* no additional treatment, *b:* coated with collagen, *c:* coated with poly-L-lysine. *d:* growth on Biofolie, no additional treatment, seeded $40000\ \text{cells}/\text{cm}^2$, 72 h incubation. *e:* growth on the surface of a polystyrene tissue culture flask (Nunc) seeded $6000\ \text{cells}/\text{cm}^2$, 72 h incubation.

ular and shows a good homogeneity. For further investigation of this membrane, the treatment protocol with poly-L-lysine was preferred because it is a synthetic protein, whereas collagen is extracted from tissue and therefore, can be producer- and lot-dependent. In Fig. 5.3d, the growth of NIH/3T3 on the Biofolie is shown. No necessity of additional treatment was found, due to the excellent growth of the cells as monolayer. For comparison, the NIH/3T3 growth on the surface of a standard polystyrene tissue culture flask is shown (Fig. 5.3e). As seen from the figure, the homogeneity of the monolayer is very good in the cases of growth on a poly-L-lysine treated Isopore membrane, Biofolie and polystyrene.

The aim of the further tests was to prove whether the cell growth on a membrane surface according to the chosen protocol induces cellular or chromosomal damage, expressed in a change of the plating efficiency or the background level of the micronuclei. The cells were seeded at the same concentration parallelly in culture flasks and the tested tissue culture inserts. After an incubation time allowing the cells to reach about 70 % confluence, both flasks and tissue culture inserts were trypsinised by the procedure described in Chapter 5.1.1. Afterwards, the standard clonogenic test was performed. Both the poly-L-lysine treated Isopore membrane and Biofolie were tested and no difference in the plating efficiency of NIH/3T3 was found in comparison to the growth on a polystyrene surface (data for Isopore are not shown). Due to the bad optical properties of Isopore, the MN test could be performed only for cells grown on Biofolie membrane. The background level of micronuclei was found to be not different after growth on Biofolie or the surface of a polystyrene flask (see Table 5.3). Therefore, the tissue culture insert with Biofolie membrane was chosen for further tests because of the possibility of cell observation during growth as well as the possibility of direct micronuclei scoring.

Table 5.3 Comparison of the control level of the PE and MN parameters after growth on Biofolie and polystyrene. The plating efficiency has been determined from one experiment (for NIH/3T3, the mean of 8 replications \pm SEM is presented, for MCF-12A, the mean of 10 replications \pm SEM is presented). The micronucleus test parameters mean values have been determined in 3 experiments for both cell lines.

Cell line	Cell substrate	Plating efficiency [%]	BNC [%]	BNC+MN [%]	MN/ BNC+MN
NIH/3T3	Biofolie	35.9 \pm 2.3	76.3 \pm 1.2	1.55 \pm 0.15	0.016 \pm 0.002
	Polystyrene	36.1 \pm 1.7	75.0 \pm 2.2	1.22 \pm 0.15	0.013 \pm 0.002
MCF-12A	Biofolie	79.3 \pm 4.5	48.1 \pm 6.6	2.78 \pm 0.68	0.029 \pm 0.008
	Polystyrene	72.3 \pm 5.1	45.9 \pm 4.8	3.06 \pm 0.58	0.032 \pm 0.006

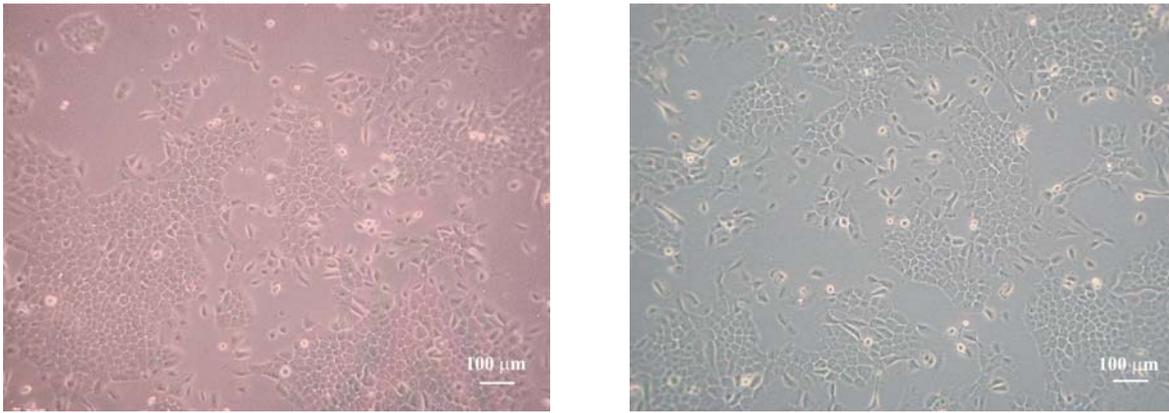


Fig. 5.4 Microphotographs of growth of MCF-12A as monolayer on Biofolie, no additional treatment, seeded at 13000 cells/cm², 77 h incubation (left), and on the surface of a polystyrene tissue culture flask (Nunc), seeded at 6700 cells/cm², 77 h incubation (right).

For the other cell line in use, the membrane that had proved to be best suitable for NIH/3T3, the Biofolie, was tested by the same criteria. In Fig. 5.4, the comparison of MCF-12A growth on the surface of a polystyrene culture flask and on Biofolie is shown. The excellent optical properties of Biofolie allow observation of living cells with a phase contrast microscope. In addition, the plating efficiency of MCF-12A and the background level of micronuclei also proved to be not different from the control after growing conventionally on polystyrene (see Table 5.3).

5.2.3 Influence of the handling procedure during irradiation on the cell survival and micronucleus test results

Other factors to be taken into account are the environmental conditions during the irradiation procedure. The optimal environmental conditions for cultured cells are sterility, humidified air at 37 °C and a stable pH value which is controlled by the fraction of CO₂ in the incubator air. Depending on the time scale of the irradiation, non-optimal environment can cause additional stress to the cells that may bias the irradiation results. For the planned experiments at ELBE, such an influence is highly possible due to the time-consuming irradiation procedure. First, the probes (and the controls) are prepared at optimal sterile conditions in the ELBE cell-laboratory and brought to the radiation physics cave just before irradiation. Then, after the radiation protection door is closed, the samples have to remain in the cave until the last one is irradiated. Afterwards, due to the radiation safety requirements, a complete exchange of the air in the cave has to be performed before the doors can be opened again. A calculation of the required time, based on the number of probes used for conventional X-ray tube irradiation, shows that, at the expected dose rate of 1 Gy/min, a minimal irradiation time of about 35 min (if a handling time of about 2 min for automatic probe change is assumed) for the cell survival and about 80 min for the micronucleus test are required. After taking into account the time necessary for adjustment before irradiation, for switching on and controlling the ELBE beam, and the time after completing the irradiation procedure, a minimal total time of approximately 2 hours is expected before the cells can be returned to the cell laboratory and further processed. Since the cells have to be outside the optimal

conditions during this time, which results in an increase of pH value and in a decrease of temperature, additional stress reactions, resulting in increased cell kill or chromosomal damage, can be expected. These possibilities were tested by the clonogenic assay as well as the micronucleus test. On the other hand, the repair of radiation damage could interfere with the primary damage and result in a reduction of the irradiation effect, or, the non-optimal conditions could compromise the repair processes, resulting in a damage higher than expected. The influence of the handling procedure on the repair outcome was tested using the micronucleus test for both cell lines.

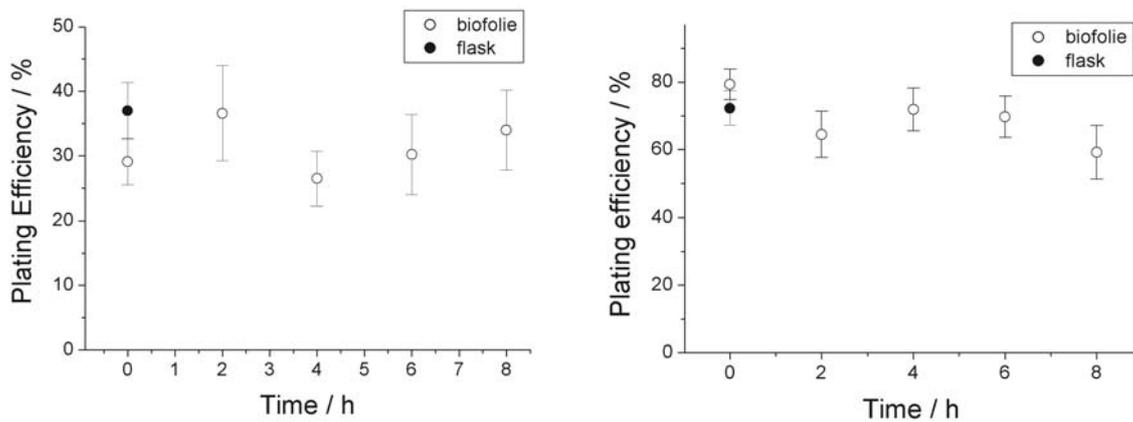


Fig. 5.5 Influence of the handling procedure on the plating efficiency for NIH/3T3 (left) and MCF-12A (right). The mean value from one experiment together with the standard error are shown.

For the experiments on cell survival, dishes with Biofolie membrane base were used. The cells were seeded in the cell culture dishes and parallelly in a cell culture flask (for reference) and incubated until reaching about 70 % confluence. For the experiment, the culture dishes were filled with medium and sealed. Since the X-ray beam at ELBE is horizontal, the cell dishes were kept in a vertical position for 0, 2, 4, 6 or 8 hours, at a temperature of 20 °C and room environment simulating the irradiation procedure. Afterwards, the cells were trypsinized and the standard clonogenic assay was performed. The dependence of the plating efficiency on the simulation time, during which the cells were kept in a vertical position, is shown in Fig. 5.5 for the cell line NIH/3T3 (left) and for MCF-12A (right). No significant change in plating efficiency due to the handling in non-optimal conditions is observed. A possible monotonic correlation between the time interval and the plating efficiency was checked using the Spearman rank correlation coefficient. At the 95 % confidence level, no correlation was proved for both NIH/3T3 and MCF-12A. Therefore, it can be concluded, that the plating efficiency is not sensitive to the handling procedure.

For the investigation of the influence of the handling procedure on the outcome of the MN test, the cells were irradiated in the ELBE radiation physics cave with an X-ray tube. The tungsten anode tube with 0.5 mm Cu filter was operated at 200 kV and 20 mA and the dose rate at the focal spot

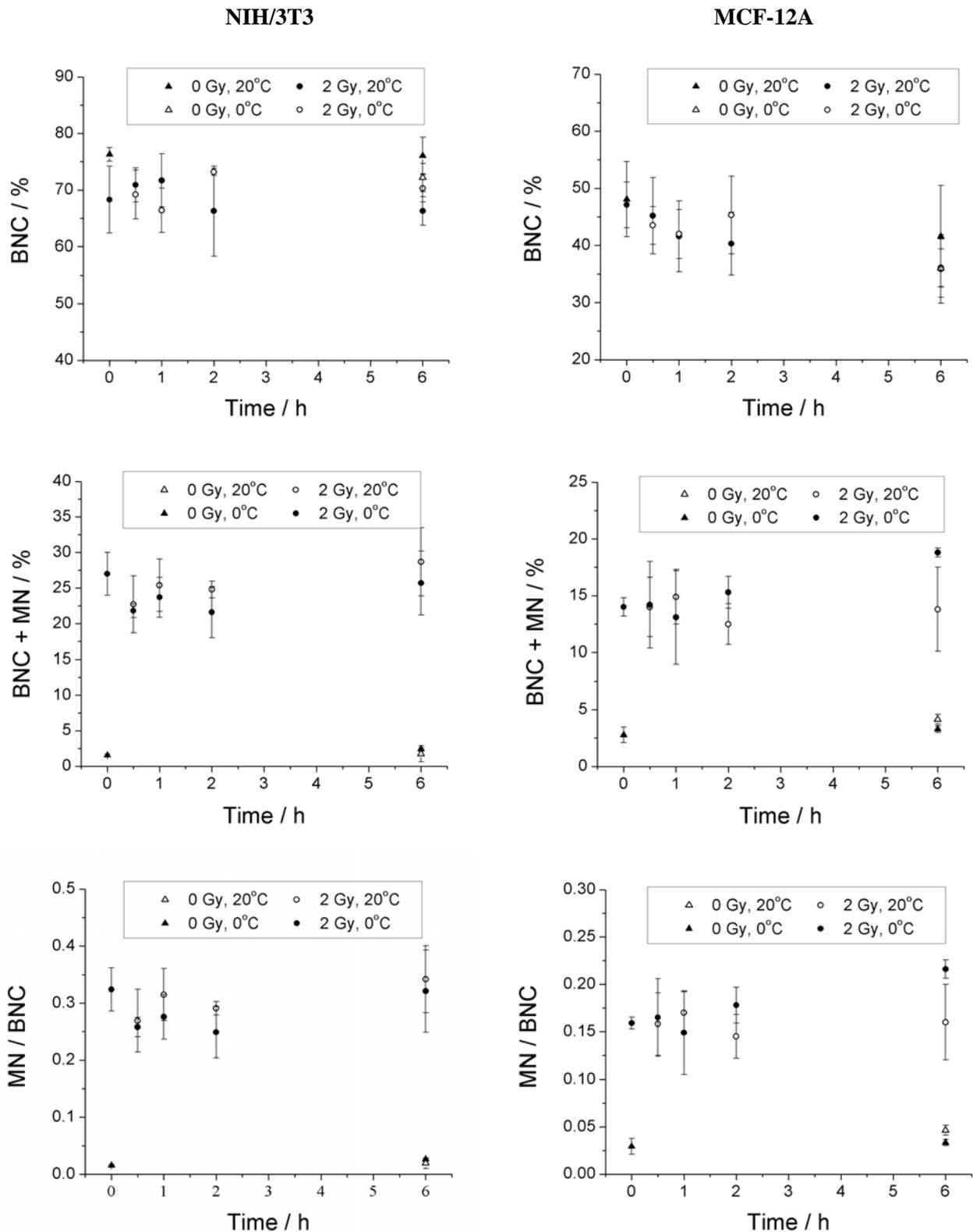


Fig. 5.6 Influence of the handling procedure on the X-ray-induced damage repair for the NIH/3T3 (left) and the MCF-12A cells (right) determined by the micronucleus test. The dependence of the fraction of BNC, fraction of BNC with MN and the number of MN per BNC on time of simulation of the irradiation procedure are shown for both cell lines. The radiation dose of 2 Gy was delivered by a 200 kV, 20 mA X-ray tube with 0.5 mm Cu filtration. The mean values and the SEM of the mean from 3 experiments for both cell lines are shown.

to cell target distance of 50 cm was measured to be 0.932 ± 0.010 Gy/min with the thimble ionisation chamber described in Chapter 4.2 [Mik04]. Three dishes were irradiated simultaneously. The irradiation dose of 2 Gy was adjusted in order to produce detectable damage and was constant for all irradiated probes. Since at lower temperature the cell metabolism is slowed, incubation on ice was expected to slow down the repair processes. The dishes were left for up to 6 hours at 20 °C or on ice to simulate the maintaining of the dishes at the irradiation site before they can be processed. Afterwards, the standard micronucleus test was performed. The resulting dependence of BNC, fraction of BNC with MN and number of MN per binucleated cell on the handling time is presented in Fig. 5.6. The results for NIH/3T3 in the left panel show that the time interval of up to 6 h is not influencing the test result (keeping the cells on ice or at room temperature). The fraction of BNC (upper plot) is not significantly different (at the 95 % confidence level) after 0.5, 1, 2 or 6 h from the BNC fraction at 0 h (immediately processed after irradiation). The same effect was observed for the fraction of BNC with MN (middle plot) and the number of MN per BNC (lower plot). The results for the MCF-12A line are shown in Fig. 5.6, right. The apparent BNC fraction decrease with increasing time is not significant (at the 95 % confidence level) due to the large spread of the data. Again, the fraction of BNC and the fraction of BNC with MN were not significantly different from the 0 h probe after 0.5, 1, or 2 h. No influence of the incubation temperature (20 °C or on ice) on the BNC fraction or the fraction of BNC with MN was observed for these handling times. However, the probe incubated 6 h on ice showed significantly higher level of irradiation damage than the 0 h probe. Therefore, as concluded from the results for the micronucleus test for the MCF-12A cell line, if a handling time longer than 2 h is expected, the probes should be kept at room temperature.

Although these experiments have been performed for the reference radiation quality, the irradiation with soft X-rays is expected to result in no faster repair of damage, therefore, the results can be used for the RBE determination, provided the same environmental conditions for all irradiations.

5.3 Design of the irradiation system at ELBE

For the determination of RBE of soft X-rays at ELBE, apart from the CR source, irradiation with a reference source is necessary to be performed. For this purpose, a high voltage X-ray unit Isovolt 320/13 (Röntgen Seifert, Ahrensburg, Germany) was installed. The maximal output power of the tube is 4.2 kW, the current at the maximal voltage of 320 kV being limited to 13 mA. An X-ray laboratory was built in the neighbouring space to the RP cave. This provides a possibility to use later the ELBE X-ray beam also outside the cave (see Fig. 3.9). Since the X-ray tube is placed free in the room, additional Pb shielding was brought inside the steel walls and ceiling of the X-ray laboratory. In addition to the radiobiological measurements, the X-ray tube has another important application. Extensive use of a photon beam independent on the ELBE beam time provides a possibility for testing and calibration of the dosimetrical systems, performing spectroscopic measurements and testing the irradiation setup. Moreover, since the construction of the X-ray tube is almost identical to the tube used as a reference source at the Medical Department of TU Dresden, the spectral distributions of both tubes

can be considered to be the same and data obtained at both tubes can be easily compared. For the RBE measurements, some of the requirements to the reference source are similar to the requirements for the soft X-ray source. Application of doses in the range 0.1 - 10 Gy to a large number of probes, dose monitoring during irradiation as well as dose homogeneity over the irradiated probe have to be provided. On the other hand, the irradiation of cells at the CR source provides some specific requirements to the irradiation setup. This includes the vertical position during irradiation, the size and geometry of the irradiated vessel, and the handling times. The irradiation vessel and the irradiation procedure at ELBE were described in Chapter 5.2.1. A membrane-base cell culture dish was chosen, providing minimal attenuation of the soft X-ray beam and good cell growth. The handling time for the probes, together with the time necessary for air exchange after irradiation, can last several hours. In order to be able to compare the results from both radiation qualities, the same environment conditions for the cells have to be maintained. Finally, a system which fulfils the demands of the ELBE CR beam and at the same time can be used at the reference radiation source, has been designed and constructed. In the irradiation system design, the limitations of the ELBE CR beam were considered at first place. The system should fit to the spatial conditions of the RP cave and be suitable for being controlled from outside the irradiation site. It has to be appropriate for extensive routine use, which means a reliable control over the irradiation procedure and user-friendly operation. The intrinsic spatial intensity distribution of CR or the distribution after monochromatisation have not yet been studied

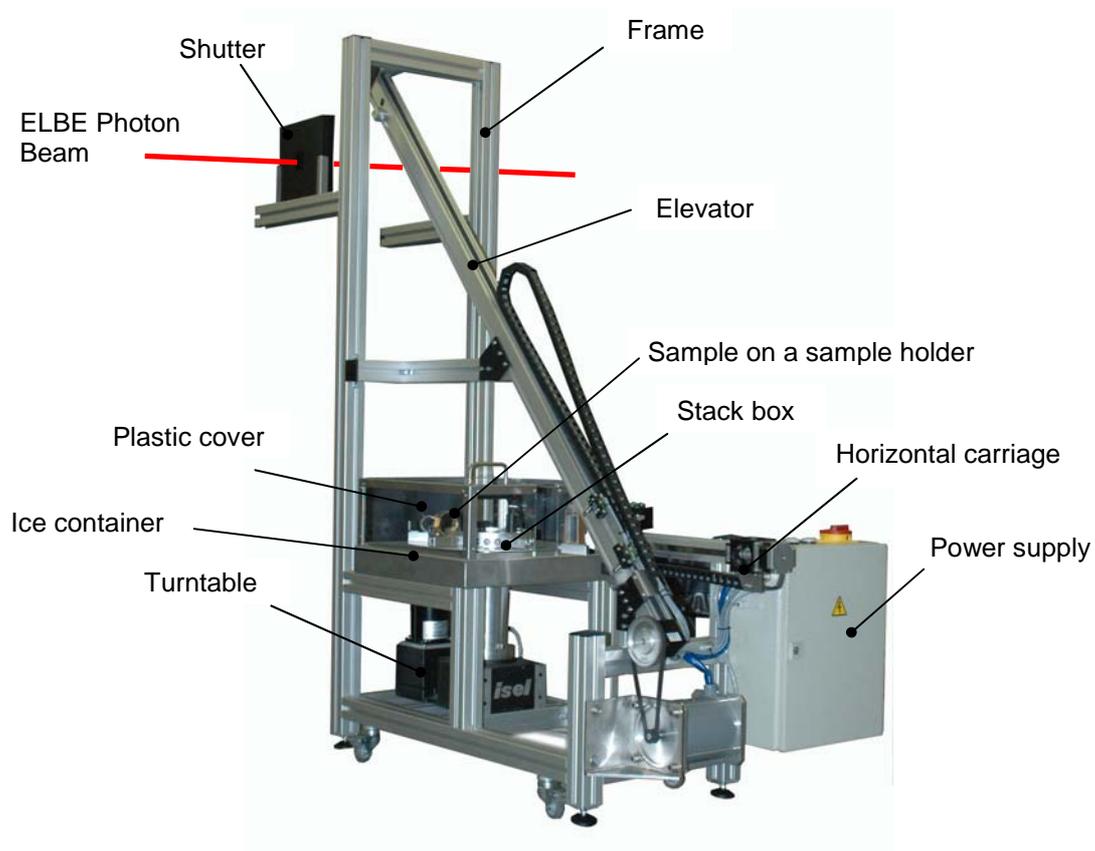


Fig. 5.7 View of the cell irradiation system.

experimentally, therefore a high flexibility in the irradiation geometry has to be considered. This requires a changeable beam aperture, as well as a possibility of probes scanning for achieving dose homogeneity. The scanning movement should be adjustable to a large range of dose rates and probe sizes. The other requirements for the irradiation system follow from the intensity variation of the ELBE photon beam with time, which results in the necessity of an online dose monitoring system. In order to provide radiation shielding from the high-energy bremsstrahlung background, the probes are kept before and after irradiation as far as possible from the X-ray beam. Different shapes of the cell vessels are also desirable, providing easier comparison to previously obtained results at an X-ray tube and variability in the combinations of endpoints and photon energy. The cell irradiation system was built by IfE-Automatisierung (Dresden, Germany), whereas the control hardware and software were produced by Intronik (Dresden, Germany). A view of the irradiation device is shown in Fig. 5.7. The system consists of a probe supply unit, a steering unit and a PC console. The steering unit is placed outside the irradiation site in order to protect the electronics from the radiation background and connected by a 25 m cable to the power supply box. From the PC console, placed also outside the irradiation site, the irradiation procedure is software controlled.

5.3.1 Cell sample holders

As already discussed in Chapter 5.2.3, a minimal total time of about 2 hours is expected before the cells can be returned to the cell laboratory. In order to provide constant environment conditions before and after irradiation, the probes are placed in a stack box, covered with a plastic lid. In the stack box, a vessel is placed below the probes, which can be filled with ice or water at 37 °C, depending on the requirements coming from the studied endpoint. The dishes are fixed in holders, specially formed for their shape, and ordered in the circular holder prior to irradiation. For transport, they are taken out by a pressure lock mounted on the horizontal carriage. The number of positions in the stack box is 27, which is sufficient even if an irradiation series of 9 dose points with 3 replications per dose point are considered. The stack box is positioned away from the beam and space for additional radiation

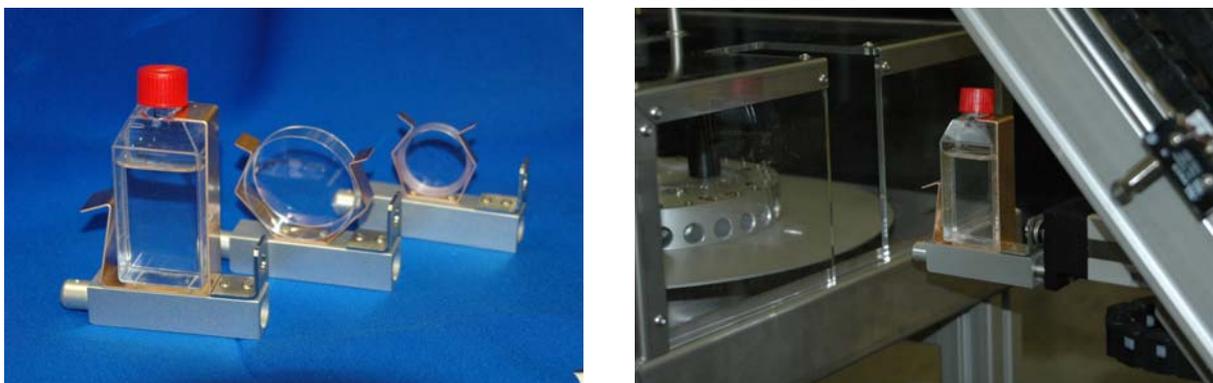


Fig. 5.8 View of the cell sample holders: left: dish holders for different geometries; right: operation of the horizontal carriage.

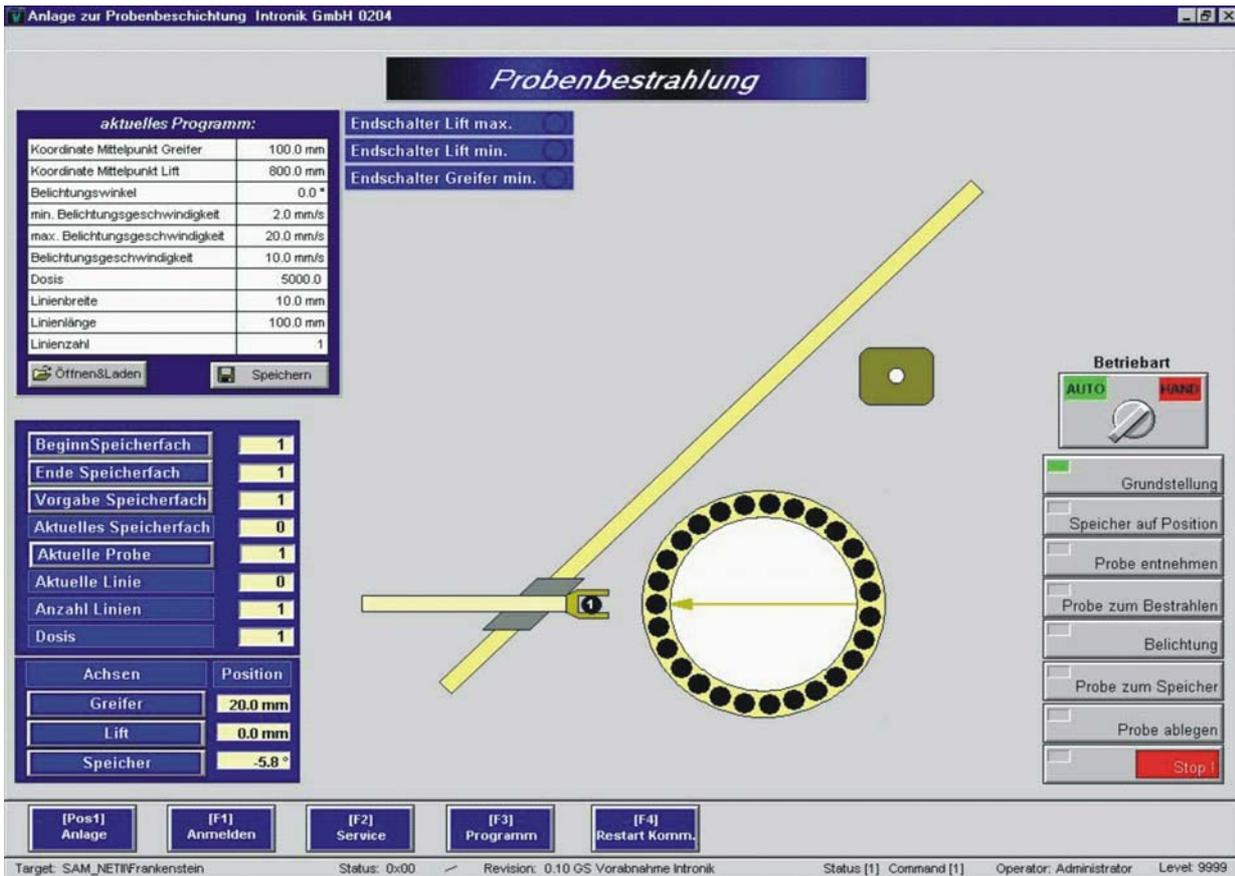


Fig. 5.9 Snapshot of the PC monitor picture.

shielding is provided (see Fig. 5.7). Several irradiation vessel geometries are possible, all of them being able to be transported and irradiated from the same stack box. The holder geometries for a 25 cm² culture flask, a Petri dish and a Biofolie membrane-based culture dish are presented in Fig. 5.8, left. In Fig. 5.8, right, the horizontal carriage of the transporting arm is shown in operation. A snapshot of the control monitor presenting the software in operation with a scheme of the probe holder position and the buttons for changing the parameters is shown in Fig. 5.9.

5.3.2 A scanning system for irradiation in a non-homogeneous field

The scanning irradiation system has to fulfil several tasks with different motion and precision. First, the desired cell probe has to be brought into starting position, taken out of the stack box and transported to the X-ray beam. In order to minimize the handling time, these procedures have to be performed fast, but on the other hand the samples should not be damaged by acceleration. Higher requirements are set for the second part of the motion, which provides the homogeneous dose distribution over the sample area. Depending on the beam characteristics, a scanning movement of the sample or a static position should be possible. First, the dose distribution of the beam spot in a homogeneous target has to be known from a measurement or a calculation. An example is shown in Fig. 5.10, left, where the dose profile in the plane perpendicular to the beam axis has an elliptic shape. Provided that the distribution has at least one symmetry axis and remains constant over time, a homogeneous dose delivery is possible using a meander scan trajectory along the axis. An example of a scanning meander for a round target is shown

in Fig. 5.10, right. A tilt angle of the meander tracks, corresponding to the tilt angle of the symmetry axis of the dose profile, can be additionally specified. The overlapping of the tracks has to be calculated in order to assure the required dose precision. The dose delivered to the cells follows, on one hand, from the scan speed, and on the other hand, from the fluctuations in the electron beam intensity, and correspondingly in the CR intensity. Therefore, a regulation of the speed by a feedback signal from an online dose monitoring system is necessary. After the desired dose over the whole probe is delivered, the transport of the probe back to the original position has to be performed. The requirements to this step are the same as to the initial step.

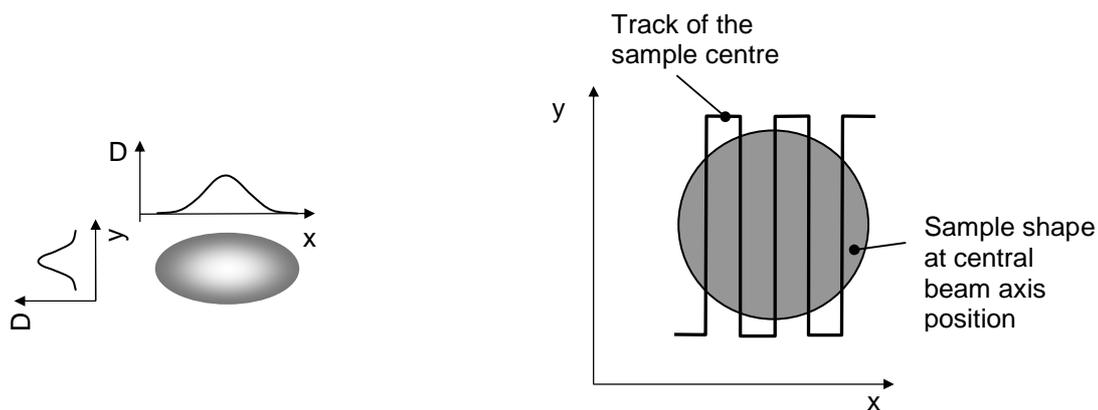


Fig. 5.10 Schematic view of a dose beam profile (left) and the meander-shaped track of the sample centre for dose homogeneity (right) over a circular probe.

In the constructed irradiation system, shown in Fig. 5.7, the movement steps are performed in the following way. Before the irradiation, the stack box is rotated until the desired probe comes in starting position. Then the probe is taken out on the horizontal carriage and transported by a slant elevator to the irradiation position. The motion along the elevator and at the irradiation position is composed of a horizontal component and a component along the elevator, both performed by linear guides. The precision of the positioning and therefore the distance between the single tracks can be varied in steps of 0.5 mm. The scan along the probe can be performed at any angle and is given with 0.1° precision. The speed along the horizontal axis limited to 20 mm/s, whereas along the elevator axis it is limited to 100 mm/s. The maximal acceleration is 30 cm/s^2 . The feedback speed control signal can be voltage or current, and in this case, the direct specification of scan speed is ignored. A suitable online dose monitoring device which provides the feedback signal for the scan speed control is a soft X-ray ionisation chamber. An online monitor of the photon flux e. g. a solid-state detector, or a device for electron current measurement can be also appropriate, provided that there exists a direct correspondence between the dose rate and the detector signal. Also a non-linear dependence between the detector signal and the dose rate could be online corrected by the software. In order to choose the most appropriate solution for the online monitoring system, the dose fluctuation has to be studied and the best practical solution has to be chosen.

6 Determination of RBE of soft X-rays by X-ray tube irradiation

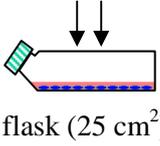
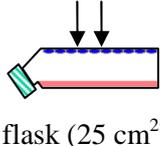
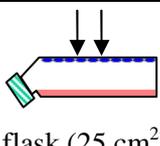
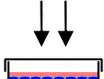
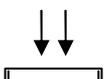
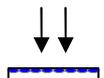
In order to prove and apply the methods developed for experiments with the ELBE photon beam, parallelly to the preparations at the ELBE irradiation site (characterisation of CR, establishment of a cell culture laboratory and an X-ray reference source at ELBE, design of the cell irradiation system), the RBE of polychromatic soft X-rays was determined by X-ray tube irradiation. This allowed to test by extensive experimental studies the dosimetric systems as well as the cell lines and radiobiological endpoints to be used at the ELBE CR beam and to gain radiobiological results. By variation of the tube voltage, different soft X-ray energy ranges were studied. However, due to the wide spectral distribution of the photons delivered by X-ray tube, the delivered dose has a complicated photon energy dependence and therefore, only a limit of the photon energy dependence of the RBE data was obtained.

6.1 X-ray tubes specification and irradiation geometries

The X-ray tube irradiation was performed at the Radiobiology Laboratory of the Medical Faculty of the Dresden University of Technology. For the soft X-ray irradiation, a tungsten target X-ray tube Darpac 150-MC (Forward Raytech, Swindon, UK) was operated at 10 kV or 25 kV. The inherent tube filtration was 2 mm Be. The reference irradiation was performed with a tungsten anode X-ray tube Isovolt 320/13 (Röntgen Seifert, Ahrensburg, Germany) with an inherent filtration of 7 mm Be. The vertical geometry of the X-ray beam in both cases did not allow to apply the same irradiation setup as will be used at the ELBE X-ray beam. The radiobiological results obtained in this work had to be easily comparable with previously accomplished experiments at the same sources and therefore, the same irradiation vessels as previously used were taken.

In order to account for the X-ray energy dependent radiation properties and the radiobiological test requirements, several setups were used, depending on the X-ray tube voltage and biological endpoint. The irradiation geometry for all setups is presented in Table 6.1. In all cases the samples were placed on a horizontal holder and irradiated with a vertical X-ray beam from above. In order to keep the optimal cell environment and sterility in the cell vessel, it had to be closed and, if possible, the cells covered with culture medium during irradiation. Since the low-energy X-rays are strongly attenuated in medium, a small variation in the thickness of the liquid culture medium would result in a large dose variation. Therefore, for the irradiation with 10 kV and 25 kV X-rays, the dishes were turned upside down and the cells were covered only by the remaining thin film of medium during irradiation (setups 2 and 4 in Table 6.1). Since the irradiation times did not exceed 15 min, no effects from the medium depletion have to be expected. For setup 4, the medium was kept in the dish by sealing the Petri dishes with a sterilized parafilm sheet which was removed after the irradiation. However, for the irradiation with 25 kV X-rays, the setup for the MN test (setup 3) was the same as in the previously accomplished experiments with other cell lines [Slo03]. The dose rate in all cases was in the range 0.3 - 1.9 Gy/min.

Table 6.1 Irradiation geometry of the experiments. The cell monolayer is schematically presented in blue and the culture medium layer is shown in red.

Biological endpoint	Setup No	X-ray tube Voltage / Current	Tube filtration	Irradiation geometry	FOD*/cm	Attenuation materials
Cell survival	1	200 kV / 20 mA	0.5 mm Cu	 flask (25 cm ²)	46.0	Polystyrene 1.2 mm Cell medium 2.0 mm
	2	25 kV / 20 mA	0.3 mm Al	 flask (25 cm ²)	25.0	Polystyrene 1.1 mm
		10 kV / 10 mA	no filtration	 flask (25 cm ²)	25.0	Polystyrene 1.1 mm
Micro-nucleus test	3	200 kV / 20 mA	0.5 mm Cu	 Petri dish (20 cm ²)	46.0	Polystyrene 1.0 mm Cell medium 1.4 mm
		25 kV / 20 mA	0.3 mm Al	 Petri dish (20 cm ²)	24.9	Polystyrene 1.0 mm Cell medium 1.4 mm
	4	10 kV / 10 mA	no filtration	 Petri dish (20 cm ²)	25.0	Polystyrene 1.0 mm

* FOD - focus to object distance

6.2 Determination of the X-ray spectral dose distribution

6.2.1 Measurement of the spectral flux distribution of a soft X-ray tube

The experiments with a polychromatic X-ray tube cannot provide entirely energy resolved RBE information, however, knowing the spectral distribution of dose, the contribution of the different energy ranges can be calculated and compared for different tube voltages. In order to calculate the spectral dose distribution, the X-ray tube energy spectrum for the 25 kV and 10 kV irradiation was measured using the PIN photodiode XR-100CR, described in Chapter 3.1. The maximal count rate of the detector, given by the producer, was about 10^4 s^{-1} . For the cell irradiation, a dose rate of about 1 Gy/min was used, which corresponds to a total flux density of $10^9 \text{ ph}/(\text{s cm}^2)$ for a tube voltage of 25 kV. The necessary

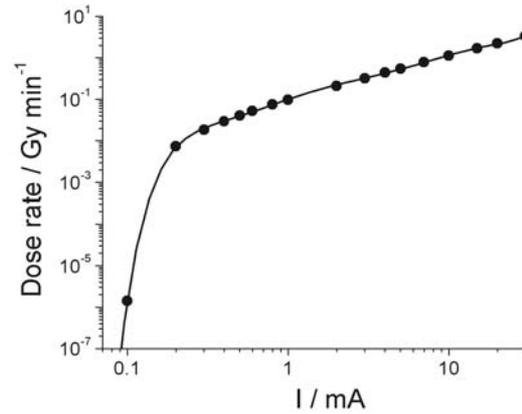


Fig. 6.1 X-ray tube current dependence of dose rate at the cell irradiation position. The tube was operated at 25 kV, with a 0.3 mm Al filter.

reduction of photon flux for the single photon measurement could be achieved by increasing the distance to the focal spot, using a collimator or operating the X-ray tube at low current. Increasing the distance up to 180 cm for the vertical beam geometry used in the measurements was possible, thus resulting in the insufficient photon flux reduction by a factor of 50. Moreover, the considerable attenuation of the low-energy part of the flux at such a distance results in a change of the spectral flux distribution. The use of a 25 μm slit Fe collimator (5 mm thick) results in about 140-times decrease of the detected flux. However, the highest flux reduction is achieved by a decrease of the tube current, due to the nonlinear behaviour at low currents. This behaviour is well illustrated by the tube current dependence of the dose rate and is presented in Fig. 6.1. Here the dose rate was measured with the soft X-ray ionisation chamber, described in Chapter 4.2, at a distance of 25 cm from the focal spot (the cell

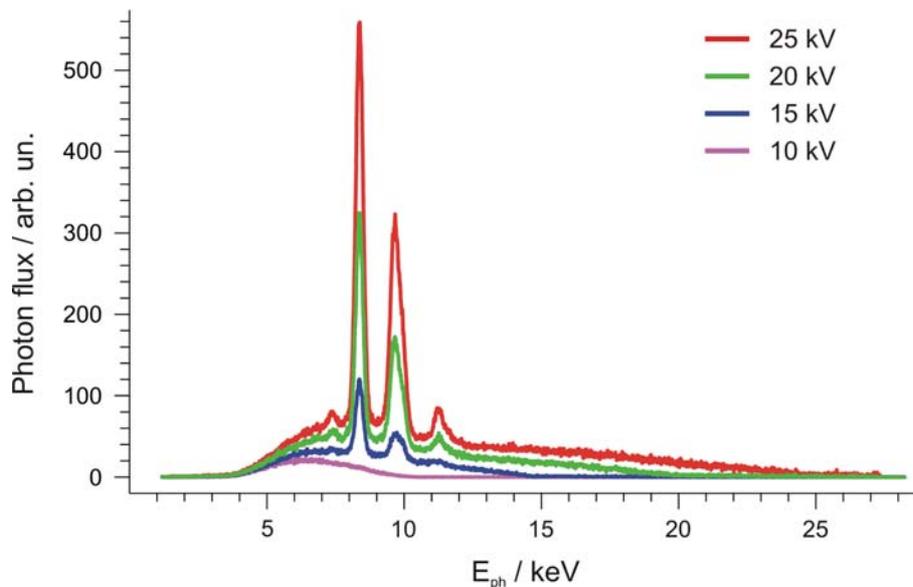


Fig. 6.2 Spectral photon flux distribution at the cell target position of the Darpac 150-MC X-ray tube operated at 10, 15, 20 and 25 kV without filtration. The spectra were measured with a Si PIN detector, smoothed and corrected for detector efficiency.

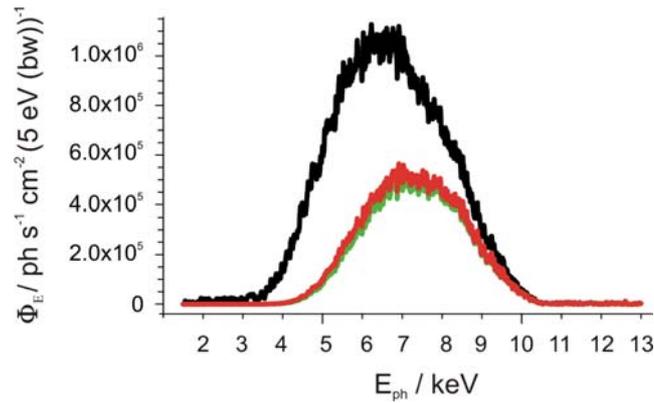


Fig. 6.3 Spectral photon flux density distribution of the Darpac 150-MC X-ray tube operated at 10 kV without filtration at the cell target position, measured with a Si PIN detector, smoothed and corrected for detector efficiency. The black curve presents a distribution normalized to a dose rate of 1 Gy/min. The spectrum after attenuation in 1.1 mm polystyrene (setup 2) is shown by the green curve, whereas the spectrum after attenuation in 1.0 mm polystyrene (setup 4) is shown by the red curve.

target position). The nonlinearity of the dose dependence is observed at a tube current below 0.3 mA. The necessary flux reduction for the spectral flux distribution measurement was achieved at the lowest possible tube current and additionally using the slit collimator. The spectra, presented in Fig. 6.2, were measured at a tube current of 0.1 mA at count rates less than 2000 s^{-1} without the attenuating materials described in Table 6.1. However, since the spectra were measured at the cell target position, the attenuation in air and the contribution of scattering are included. The spectra are corrected for detection efficiency (see Chapter 3.3) and smoothed. The spectral distributions present the expected high voltage dependence of the total flux and of the intensity of tungsten characteristic lines.

In order to calculate the photon flux density distribution from the measured detector count rate, the actually irradiated field size on the detector determined from the collimator size and the distance to the focal spot have to taken into account. From the photon flux density distribution, the spectral dose rate distribution and correspondingly, the absolute total dose can be calculated according to the method presented in Chapter 3.3 and using Eq. (3.19). For all further presented radiation qualities, the mass-energy absorption coefficient for water [Nis98] was used to approximate the dose absorbed in the cell monolayer.

For the cell irradiation with 10 kV X-rays, setup 2 or 4 (see Table 6.1) was used. Since there was no medium covering the cells, the beam was attenuated only in the 25 cm air and in the plastic bottom of the culture dish. The X-ray spectrum, presented in Fig. 6.3, was measured at the position of the cell layer, thus including the attenuation in the air and the scattering contribution. For this measurement, the tube was operated at a current of 0.1 mA, and the $25 \mu\text{m}$ Fe slit collimator was placed in front of the detector, resulting in a count rate of about 100 s^{-1} . The spectral flux density distribution, normalized to a dose rate of 1 Gy/min in a $10 \mu\text{m}$ thick water target representing the cell monolayer, corrected for the detector efficiency and smoothed, is presented by a black curve. The green curve is obtained from the

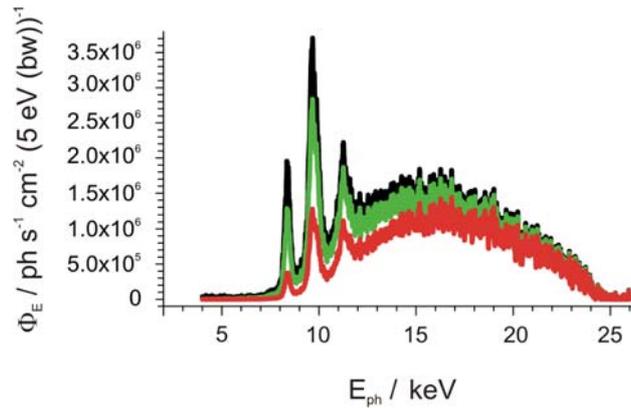


Fig. 6.4 Spectral photon flux density distribution of the Darpac 150-MC X-ray tube operated at 25 kV with a 0.3 mm Al filter at the cell target position, measured with a Si PIN detector, smoothed and corrected for detector efficiency. The black curve represents a distribution normalized to a dose rate of 1 Gy/min. The spectra after attenuation in 1.1 mm polystyrene (green) and in 1.0 mm polystyrene plus 1.4 mm water (red) are also presented.

initial flux density distribution after calculation of the X-ray attenuation in 1.1 mm polystyrene, corresponding to setup 2. The red curve represents the situation in setup 4, where the attenuation was 1 mm polystyrene. For these distributions, the energy dependent mass attenuation coefficient for polystyrene [Nis98] was used. The strong attenuation of the low-energy X-rays in the polystyrene layer leads to a considerable change of the spectrum. The difference in the thickness of the polystyrene flask and the Petri dish results in a very small difference in the spectral flux density distributions.

For the X-ray tube operated at 25 kV with a 0.3 mm Al filter, the spectral photon flux density distribution was again measured at the cell target position, at the lowest possible current of 0.1 mA and using the slit collimator, resulting in a count rate of about 200 s^{-1} . The measured spectrum, corrected for detector efficiency and smoothed, is presented in Fig. 6.4 by a black curve. This spectral distribution is normalised to a dose rate of 1 Gy/min in a $10 \mu\text{m}$ thick water target, representing the cell monolayer. In order to account for the different irradiation setups, the spectra at the cell surface in the case of the different setups are presented in addition (colour lines). For the cell irradiation with 25 kV X-rays, setups 2 and 3 (see Table 6.1) have been used, thus resulting in different attenuating materials included in the X-ray beam. The X-ray flux density distribution at the cell position in setup 2 corresponds to the green curve, calculated from the initial flux density distribution with the energy dependent mass attenuation coefficient for polystyrene [Nis98]. The setup 3 used for the micronucleus test results in a modified photon flux density distribution, presented by the red curve in the same figure. It was calculated from the initial distribution, using the mass attenuation coefficient for polystyrene and water [Nis98] used as an approximation for the 1.4 mm thick layer of culture medium. A change in the low-energy part of the spectrum is observed in the case of setup 3 from the attenuation in 1 mm polystyrene and 1.4 mm water, whereas the inclusion of 1.1 mm polystyrene (setup 2) alone brings no considerable change. However, the dose rate is calculated from the spectral flux density distribution with the mass-energy absorption coefficient of the target material, which has a strong energy dependence at low

photon energies, therefore for both 10 and 25 kV X-rays and in each setup, the influence of the attenuation materials on the dose, and not only on the flux has to be considered.

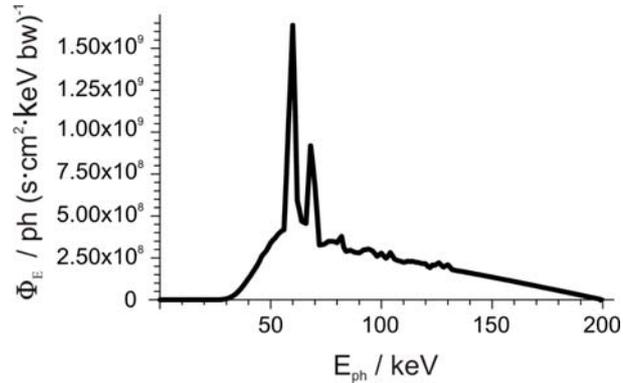


Fig. 6.5 Spectral photon flux density distribution of an X-ray tube with a tungsten anode, operated at 200 kV, with 0.5 mm Cu filtration and 1 mm polystyrene and 2 mm water attenuation. The flux density is normalized to 1 Gy/min dose rate in a 10 μm thick water target.

6.2.2 Calculation of the spectral flux distribution of the reference X-ray tube

For the reference irradiation by a 200 kV X-ray tube, no direct measurement of the photon flux was performed. An X-ray tube, operated at 200 kV and 20 mA with a 0.5 mm Cu filter, emits about 10^{10} ph/(s cm²) for a dose rate of 1 Gy/min at a distance of about 50 cm. In order to perform a spectroscopic measurement, the count rate of the detector should be at least 6 orders of magnitude less, which can be achieved by decreasing the tube current, increasing the distance to the focal spot, using a collimator and using a detector with low efficiency in this X-ray energy range. The minimal tube current was 1 mA, and the maximal possible focal spot-detector distance was about 20 cm, resulting altogether in a decrease factor of the count rate of about 80. The Fe collimator cannot be used, since the hard X-rays are not attenuated in the 5 mm thick wall and would reach the detector. Due to the low detector efficiency, the count rate is decreased less than 50 times. Therefore, even at the minimal current and maximal distance, the count rate would be still far above the maximal count rate allowed by the detector producer. Thus, the photon flux from a tungsten anode X-ray tube was calculated using an approach described by Boone and Seibert [Boo97], based on interpolation of measured spectra. For the generation of a range of X-ray spectra at tube voltages between 40 and 140 kV, the software XOP [Rio03] was used. Using these spectral photon flux distributions, an interpolating function of the dependence of flux values on the tube voltage is built in steps of 1 keV. From the values of the function, extrapolated to 200 kV, the spectral flux distribution was obtained. The cell irradiation with the 200 kV X-rays with a 0.5 mm Cu filter was performed using either setup 1 or 3 (see Table 6.1). The X-ray flux distribution at the cell position was calculated from the initial flux distribution using the energy dependent mass attenuation coefficient for Cu, polystyrene and water, representing the culture medium [Nis98]. Since the influence on the photon flux distribution due to the attenuation in polystyrene and water layers used in all setups was found to be negligible, an example of photon flux density at the cell

surface after attenuation in 1 mm polystyrene and 2 mm water was calculated and is shown by the black curve in Fig. 6.5, normalized to a dose rate of 1 Gy/min. The attenuating effect of the Cu filtration is mostly expressed at photon energy below about 40 keV and completely outweighs the attenuation in polystyrene or water.

6.2.3 Spectral dose distributions

Using the spectral photon flux density distributions presented in Figs. 6.3, 6.4 and 6.5, the spectral dose rate, and correspondingly, the spectral dose distribution for the different radiation qualities was calculated.

Table 6.2 Spectral dose distribution of the X-ray tubes operated at different high voltages.

Tube voltage and filtration	Setup No*	Attenuation materials	Mean photon energy / keV	Dose-weighted mean photon energy / keV	Photon energy range / keV	Dose fraction / %
10 kV	2	1.1 mm polystyrene	7.3	6.9	< 5	4.4
					5 - 10	95.6
10 kV	4	1.0 mm polystyrene	7.3	6.9	< 5	5.1
					5 - 10	94.9
25 kV, 0.3 mm Al	2	1.1 mm polystyrene	15.3	12.9	< 5	0.1
					5 - 10	28.9
					10 - 15	43.3
					15 - 20	22.3
					20 - 25	5.3
25 kV, 0.3 mm Al	3	1.0 mm polystyrene + 1.4 mm water	16.1	14.0	< 5	0.0
					5 - 10	17.4
					10 - 15	45.1
					15 - 20	29.9
					20 - 25	7.6
200 kV, 0.5 mm Cu	1	1 mm polystyrene + 2 mm water	90.0	100.9	< 25	0.0
					25 - 40	1.9
					40 - 60	18.8
					60 - 80	19.8
					80 - 100	13.2
					100 - 150	31.1
150 - 200	15.3					

*See Table 6.1

Table 6.3 Comparison of the dose rate calculated on the base of the spectral photon flux distribution and the dose rate measured by ionisation chamber for the X-ray tube operated at 10 kV and 25 kV.

	Dose rate / mGy min ⁻¹	
	10 kV, no filter	25 kV, 0.3 mm Al
Ionisation chamber measurement	0.077 ± 0.004	0.084 ± 0.004
Calculation	0.163 ± 0.085	0.098 ± 0.050

ed as described in Chapter 6.2.1, using Eq. (3.19). The corresponding contribution of the different energy ranges to the total delivered dose is presented in Table 6.2. The uncertainty of the dose rate is obtained by error propagation. The spectral flux distribution contributes by the statistical error from the detector count number, the uncertainty of the detector efficiency correction, and by the detector area and collimator size uncertainty. The statistical error of the count rate is estimated to be $\pm 7\%$ in the case of 25 kV X-rays, and $\pm 16\%$ in the case of 10 kV X-rays due to the low photon flux below 5 keV. The detector efficiency correction is performed as discussed in Chapter 3.3.3, using the mass attenuation coefficients from the NIST database [Nis98]. Since their uncertainty is less than $\pm 5\%$ in the considered energy range [Hub99], the uncertainty of the detector efficiency correction, which also includes the uncertainty of the Be window and detector thickness, is calculated to be $\pm 8\%$ in the case of the 25 kV, and less than $\pm 1\%$ in the case of 10 kV X-rays. However, the largest uncertainty comes from the detector area ($\pm 28\%$). The contribution of all other uncertainties can be estimated to be about $\pm 8\%$, therefore the final error in the calculated dose is about $\pm 51\%$ and $\pm 52\%$ for 25 kV and 10 kV X-rays, correspondingly.

For verification of the calculated results, dose rate measurements for the 25 kV X-rays and 10 kV X-rays were performed using a soft X-ray ionisation chamber with a 0.02 cm³ sensitive volume and the dosimeter Unidos, described in Chapter 4.2. The ionisation chamber was positioned at the same place where the detector measurement had been performed and the tube was operated with the same parameters and filtration. The determination of absolute dose in water with an ionisation chamber was performed according to Eq. (4.3). The radiation quality correction factor k_Q for the corresponding tube voltage and filtration was determined by a cross check to an identical dosimetric system, but calibrated exactly for the used radiation qualities. Due to the weak photon energy dependence of the chamber response, the consistence between the two systems was found to be better than 0.8%. Since the tube current was minimised, the chamber was operated in the “dose” modus, which allowed a precision for the dose rate calculation better than 0.5% (see also Chapter 4.2). The values for the measured and calculated dose rate for the 25 kV X-rays and 10 kV X-rays are presented in Table 6.3. Due to the large uncertainty, the calculation from the photon flux distribution allows to obtain only rough information

about the absolute dose rate. However, it provides spectral information which cannot be obtained with an ionisation chamber. Since the effect of X-rays depends on the spectral and spatial distributions of the produced secondary electrons, this information is necessary in order to resolve the radiobiological effects and understand their photon energy dependence.

6.3 Experimental results for RBE determination

6.3.1 Determination of plating efficiency

In order to measure the clonogenic survival after irradiation with 10 kV, 25 kV and 200 kV X-rays, the survival at zero dose – plating efficiency (PE) – was determined for both used cell lines NIH/3T3 and MCF-12A by the standard procedure of clonogenic assay, described in Chapter 5.1.2. An example of the PE dependence on the passage number is presented in Fig. 6.6, performed for both lines on 1 or 2 experiments per passage, with 8 - 10 replications per experiment. The correlation between the passage number and the PE was studied by means of Pearson's correlation coefficient, which is used to prove linear correlation between the data. No correlation was found for both cell lines at the 95 % confidence level, the correlation coefficient being -0.207 (NIH/3T3 mouse fibroblasts) and 0.243 (MCF-12A human mammary epithelial cells). Such a behaviour of the PE is expected for these continuous lines. For the NIH/3T3 cells, experiments over more passages were performed, however not on all consecutive passages (see Fig. 6.6, left). It should be nevertheless possible to observe, if present, any monotonic dependence. As seen from the figure, there is no monotonic change of PE, however, a big spread of the PE values is observed. The reason for this was probably the quality of the culture medium components, and mainly of the serum, for which this cell line seems to be especially sensitive. Such behaviour of the PE for the NIH/3T3 was constantly observed over the long time of cell culture in our laboratory. However, in spite of the variation, this fact has no quantitative influence on the clonogenic assay, because the results are expressed in terms of relative survival and not in absolute values of PE.

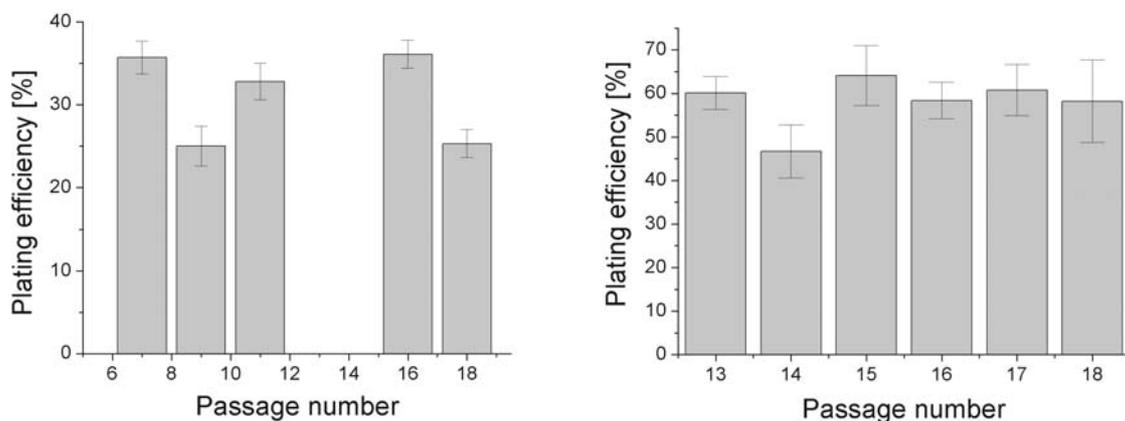


Fig. 6.6 Dependence of the plating efficiency (PE) on the passage number for NIH/3T3 (left) and MCF-12A (right). The mean value from 1 or 2 experiments (8 - 10 repetitions) together with the SEM is shown.

Table 6.4 Surviving fraction after irradiation with 10 kV, 25 kV and 200 kV X-rays. Values given are the mean from 3 - 11 experiments \pm SEM.

Dose / Gy	10 kV		25 kV		200 kV	
	Surviving Fraction	Number of experiments	Surviving Fraction	Number of experiments	Surviving Fraction	Number of experiments
<i>Mouse fibroblasts (NIH/3T3)</i>						
0	1.000 \pm 0.038	6	1.000 \pm 0.092	11	1.00 \pm 0.107	9
0.5	0.848 \pm 0.054	6	-	-	-	-
1.0	0.828 \pm 0.100	6	0.805 \pm 0.086	4	0.842 \pm 0.087	7
1.5	-	-	0.883 \pm 0.170	4	-	-
2.0	0.487 \pm 0.083	6	0.592 \pm 0.062	6	0.642 \pm 0.071	6
2.5	-	-	0.504 \pm 0.066	4	-	-
3.0	0.318 \pm 0.100	6	0.351 \pm 0.038	4	0.392 \pm 0.043	3
3.5	-	-	0.286 \pm 0.029	4	-	-
4.0	-	-	0.238 \pm 0.026	4	0.290 \pm 0.036	3
4.5	-	-	0.114 \pm 0.013	4	-	-
5.0	0.0647 \pm 0.0080	6	0.108 \pm 0.017	4	0.182 \pm 0.023	3
6.0	-	-	0.0389 \pm 0.0067	4	0.128 \pm 0.013	3
7.0	0.0256 \pm 0.0072	6	-	-	0.0574 \pm 0.0081	4
8.0	-	-	-	-	0.0415 \pm 0.0059	3
10.0	-	-	-	-	0.0209 \pm 0.0042	6
<i>Human mammary epithelial cells (MCF-12A)</i>						
0	1.000 \pm 0.080	6	1.000 \pm 0.069	10	1.000 \pm 0.042	11
1.0	0.772 \pm 0.066	6	0.823 \pm 0.082	9	0.839 \pm 0.078	11
2.0	0.402 \pm 0.048	6	0.552 \pm 0.059	10	0.519 \pm 0.056	11
3.0	0.221 \pm 0.048	6	0.244 \pm 0.036	10	0.277 \pm 0.022	11
4.0	0.0901 \pm 0.0035	6	0.133 \pm 0.017	10	-	-
5.0	0.0392 \pm 0.0050	6	0.0440 \pm 0.0017	8	0.0763 \pm 0.0073	11
7.0	0.0101 \pm 0.0017	6	0.00558 \pm 0.00075	10	0.0174 \pm 0.0018	11
10.0	-	-	-	-	0.00168 \pm 0.00034	11

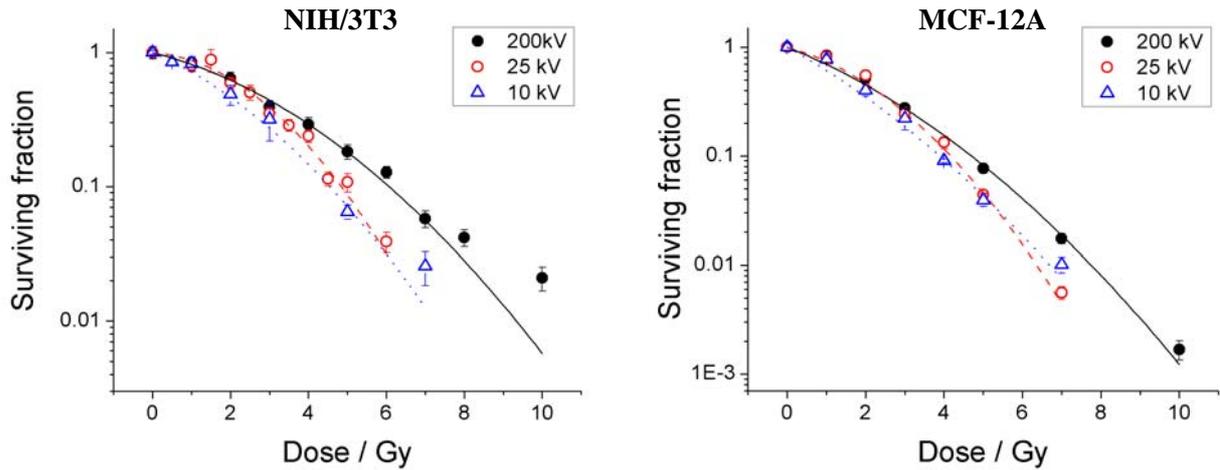


Fig. 6.7 Survival of NIH/3T3 (left) and MCF-12A (right) after irradiation with 10 kV X-rays (open triangles, dotted lines), 25 kV X-rays (open circles, dashed lines) and 200 kV X-rays (filled circles, solid lines). The mean value together with the SEM from 3 - 11 experiments is shown.

6.3.2 Clonogenic Survival

Clonogenic survival was determined for the three radiation qualities studied and the results for both cell lines are presented in Table 6.4 and Fig. 6.7. The dose range used for RBE determination is limited by several factors. Both the low and the high dose limits are set by the radiosensitivity of the cell line. At the lower dose limit, a survival beyond the uncertainty range due to variations in the PE is desirable. The upper dose limit depends on the absolute value of PE as well, since it influences the absolute number of colonies. A very low survival, combined with a low PE, would require a high number of seeded cells per dish. Cell concentrations of more than several thousands per cm^2 can result in specific effects, like the feeder cells effect. In this case, most of the cells are unable to further proliferate, but can still produce substances that influence the proliferation of the surviving cells. In addition, the surviving colonies, which are usually small at high doses, are difficult to distinguish at such cell concentrations, and this could lead to wrong estimation of the surviving fraction. Therefore, the dose range has to be determined individually for each cell line. In addition, the number of dose points is limited by the practical work, since the processing of the cell probes has to start immediately after irradiation and takes up to 1 hour per dose. All probes are processed simultaneously and in order to minimize the stress on the cells, the number of probes has to be limited to about eight (the duplicated control included).

The mean values of the survival for each dose were determined by weighting, if different, by the number of replications in each experiment. The survival data were fitted by the least-squares method to the linear-quadratic model:

$$S = \exp(-\alpha D - \beta D^2) \quad (6.1)$$

where S is the survival at dose D . The meaning of the parameters α and β as well as the application of this model are discussed in the Appendix. No weighting was used in the fitting procedure for the

survival curve after 200 kV and 25 kV irradiation for the NIH/3T3 cell line, since it allows to reduce the influence of the observed scatter of the survival values in the high-dose range. In all other cases the weight of each survival point was set to the standard error of the mean (SEM) from all experiments, which allows to give more weight to the dose points where more experiments were made. For the χ^2 minimisation, the Levenberg-Marquardt method was used, implemented in the software Mathematica 4.1 [Wol01]. The survival of NIH/3T3 after irradiation with 25 kV and 200 kV X-rays has been already published in detail [Pan03], the curve and data summary are shown here for discussion.

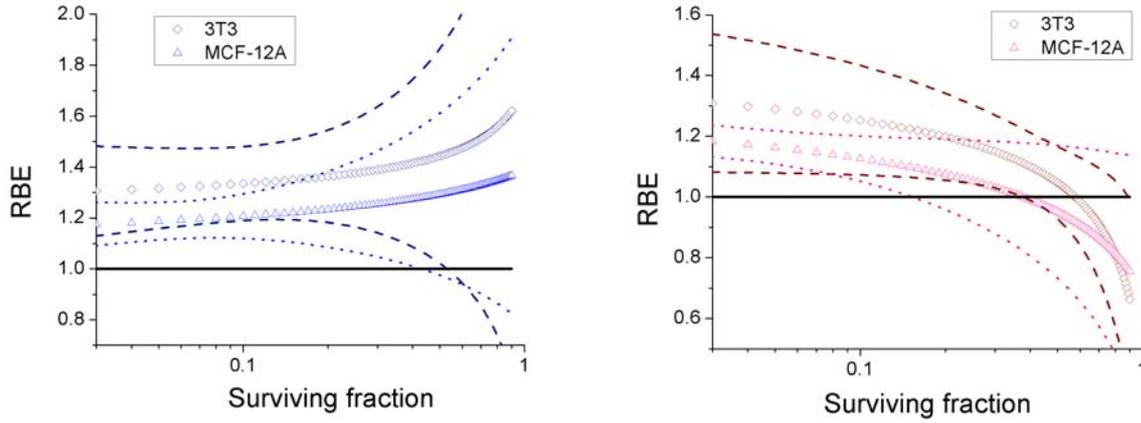


Fig. 6.8 RBE dependence on the survival level for the 10 kV X-rays (left) and 25 kV X-rays (right) relative to the 200 kV X-rays. The dashed and dotted lines correspond to the 95 % confidence intervals for NIH/3T3 and MCF-12A, correspondingly. The black solid lines at $RBE = 1$ are shown for better comparison.

The RBE at a certain survival level was calculated by relation of the doses for the corresponding radiation quality and the 200 kV X-ray reference source, see Eq. (2.6). The error of the RBE is calculated then by error propagation:

$$s_{RBE} = \frac{\sqrt{s_{D_{ref}}^2 D_x^2 + s_{D_x}^2 D_{ref}^2}}{D_x^2} \quad (6.2)$$

Thus the RBE uncertainty includes the uncertainties with which the doses at a particular survival level are determined, and, correspondingly, the uncertainties of the parameters α and β . The uncertainty of the dose $s_D(S)$ has to be determined by error propagation, whereas the parameters α and β for each survival curve are not independent:

$$s_D^2(S) = \left(\frac{\partial D}{\partial \alpha}\right)^2 s_\alpha^2 + \left(\frac{\partial D}{\partial \beta}\right)^2 s_\beta^2 + 2\left(\frac{\partial D}{\partial \alpha}\right)\left(\frac{\partial D}{\partial \beta}\right) \text{cov}(\alpha, \beta) \quad (6.3)$$

where s_α and s_β are the errors of the parameters α and β , obtained from the fitting procedure. The quantity $\text{cov}(\alpha, \beta)$ is the covariance of α and β , which is a measure of the correlation between the two parameters. It is calculated from the non-diagonal elements of the covariance matrix σ :

$$\sigma_{jk} = \chi^2 (a^{-1})_{jk} \quad (6.4)$$

The diagonal elements of the covariance matrix σ_{ii} are the squared errors of the parameters s_α and s_β , and the elements of the a -matrix for the applied linear-quadratic model $D(S_i, \alpha, \beta)$ are determined as the following sum over the N experimental points:

$$a_{jk} = \sum_{i=1}^N \frac{\partial D(S_i, \alpha, \beta)}{\partial \alpha} \frac{\partial D(S_i, \alpha, \beta)}{\partial \beta} \quad (6.5)$$

The RBE dependence on the survival level, calculated according to this method for the NIH/3T3 and MCF-12A, is shown in Fig. 6.8. The resulting fitting parameters to the survival curves for both cell lines together with their uncertainties and the coefficient of determination R^2 are presented in Table 6.5. As a measure of the radiosensitivity of the two cell lines, the surviving fraction after irradiation with 2 Gy (SF2), presented also in Table 6.4, can be used. For 200 kV irradiation, it was found to be $64.2 \pm 7.1\%$ and $51.9 \pm 5.6\%$ for mouse fibroblasts and human mammary epithelial cells, correspondingly. The irradiation with 25 kV or 10 kV X-rays does not change the order in radiosensitivity, resulting in SF2-values of $59.2 \pm 6.2\%$ and $48.7 \pm 8.3\%$ for the mouse cell line and $55.2 \pm 5.9\%$ and $40.2 \pm 4.8\%$ for the human cell line, respectively.

Table 6.5 Coefficients and standard error (SE) of the linear-quadratic model and the $RBE_{0.1}$ at the 10 % survival level together with the SE for the survival after irradiation with 10 kV, 25 kV and 200 kV X-rays for the two cell lines. Also presented are the coefficients of determination R^2 of the curves.

Cell line	α / Gy^{-1}	β / Gy^{-2}	R^2	$RBE_{0.1}$
<i>Mouse fibroblasts (NIH/3T3)</i>				
10 kV X-rays	0.288 ± 0.082	0.048 ± 0.017	0.994	1.34 ± 0.06
25 kV X-rays	0.050 ± 0.048	0.088 ± 0.017	0.978	1.25 ± 0.07
200 kV X-rays	0.169 ± 0.022	0.035 ± 0.006	0.996	
<i>Human mammary epithelial cells (MCF-12A)</i>				
10 kV X-rays	0.460 ± 0.061	0.034 ± 0.014	0.986	1.21 ± 0.03
25 kV X-rays	0.226 ± 0.055	0.078 ± 0.011	0.992	1.13 ± 0.03
200 kV X-rays	0.331 ± 0.037	0.034 ± 0.006	0.993	

6.3.3 Micronucleus test

Data for micronuclei induction in NIH/3T3 after irradiation with 25 kV X-rays relative to 200 kV X-rays have been already published in detail [Slo03]. In the presented work, these results have been completed with the determination of RBE of 10 kV X-rays for the same cell line. Furthermore, the micronucleus test was used to determine the RBE of 25 kV X-rays for the MCF-12A cell line. In both cases, 200 kV X-rays were used as a reference source.

The linear-quadratic model in the form

$$N = \alpha D + \beta D^2 + c \quad (6.6)$$

was applied to approximate the data, where N is the corresponding measure of the damage, and c corresponds to the background level of damage. For determination of the effectiveness of the radiation quality x in this case it is convenient to use the quantity RBE_M :

$$RBE_M = \frac{\alpha_x}{\alpha_{ref}} \quad (6.7)$$

It is obtained from the expression for RBE, cf. Eq. (2.6), at $D \rightarrow 0$ for the linear-quadratic model shown by Eq. (6.6) and corresponds to the maximum RBE. The uncertainties of the α -parameters are obtained from the fitting procedure. The error of RBE is calculated by error propagation. The results for the dose dependence of the fraction of binucleated cells (BNC), fraction of binucleated cells with micronuclei (BNC+MN), the number of micronuclei per binucleated cell (MN/BNC) and the number of micronuclei per binucleated cell with micronuclei (MN/(BNC+MN)) for the two cell lines and all studied radiation qualities have been calculated.

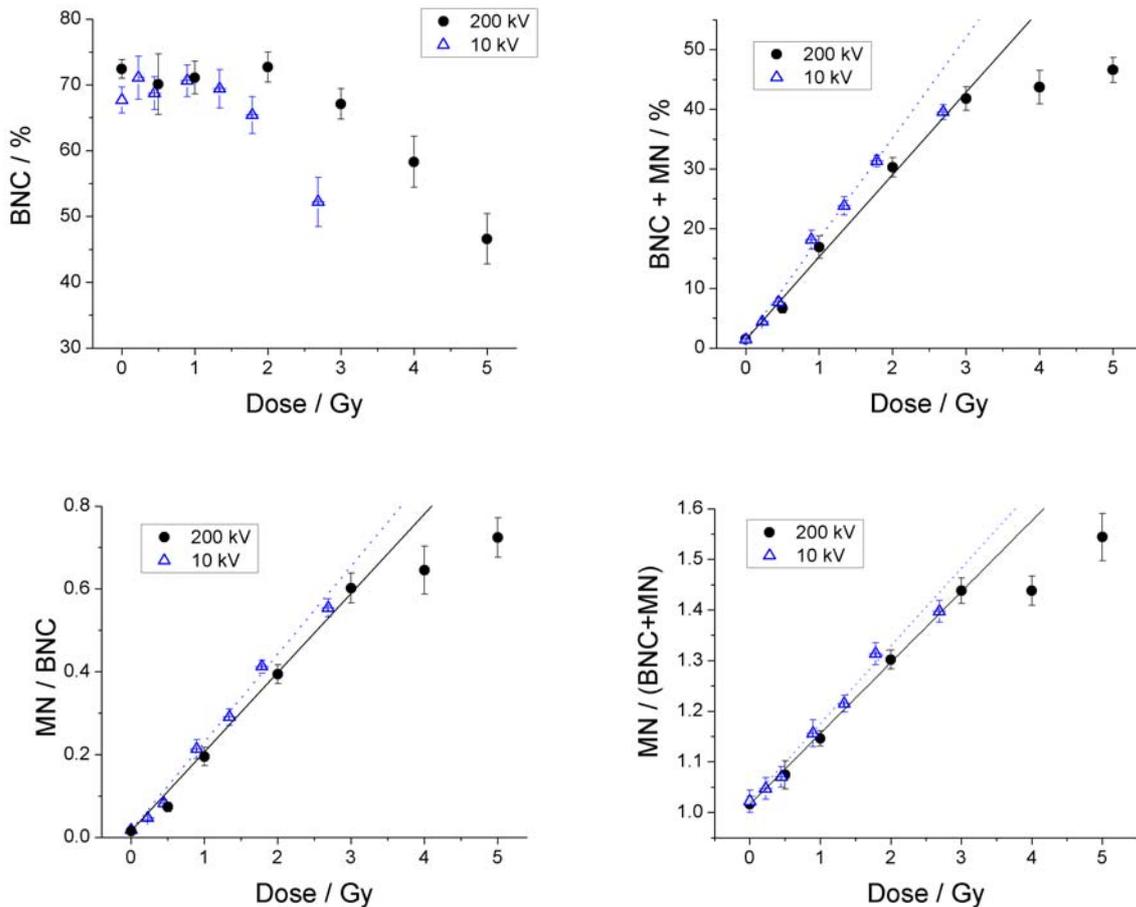


Fig. 6.9 Dose response of micronuclei induction after irradiation of NIH/3T3 cells with 10 kV X-rays (open triangles, dotted lines) and 200 kV X-rays (closed circles, solid lines). The mean value and the SEM from 5 experiments for each radiation quality is shown. The dose values for the 10 kV X-rays are presented together with the dose SEM.

For the determination of RBE of 10 kV X-rays for NIH/3T3, 5 experiments have been performed for each radiation quality. The irradiation with 10 kV X-rays was performed in Petri dishes, placed upside down in a holder (see Table 6.1, setup 4) for all dose points. As shown in Fig. 6.3, the X-ray spectrum is attenuated considerably in the about 1 mm thick plastic dish wall. In order to exclude the influence of the thickness variation on the dose value, the same dish thickness has to be used in the dose measurement and in every cell irradiation. Since this is not practicable, the thickness-dose rate dependence was measured and fitted to a quadratic function by a least-squares fit (coefficient of determination $R^2 = 0.959$). Additionally, after cell staining, the thickness of each dish was measured, and from the thickness dependence of the dose rate, the absorbed dose was determined individually for each Petri dish. This procedure allowed to determine the absorbed dose precisely even if a different dish thickness was used for dosimetry.

Table 6.6 Dose dependence of the fraction of binucleated cells and micronuclei induction in NIH/3T3 after irradiation with 10 kV and 200 kV X-rays. The mean values from 5 experiments together with the SEM are given.

Dose / Gy	BNC / %	BNC+MN / %	MN/BNC	MN/(BNC+MN)
<i>10 kV X-rays</i>				
0	67.7 ± 2.0	1.43 ± 0.16	0.0177 ± 0.0028	1.02 ± 0.02
0.226 ± 0.00080	71.1 ± 3.3	4.42 ± 0.42	0.0465 ± 0.0046	1.05 ± 0.02
0.446 ± 0.0011	68.7 ± 2.5	7.70 ± 0.69	0.0823 ± 0.0075	1.07 ± 0.02
0.894 ± 0.0030	70.6 ± 2.4	18.2 ± 1.6	0.213 ± 0.023	1.16 ± 0.03
1.34 ± 0.0040	69.4 ± 2.9	23.8 ± 1.5	0.290 ± 0.020	1.21 ± 0.02
1.78 ± 0.0059	65.4 ± 2.8	31.4 ± 1.0	0.412 ± 0.016	1.31 ± 0.02
2.69 ± 0.0094	52.2 ± 3.7	39.5 ± 1.3	0.554 ± 0.022	1.40 ± 0.02
<i>200 kV X-rays</i>				
0	72.4 ± 1.4	1.47 ± 0.12	0.015 ± 0.013	1.02 ± 0.02
0.5	70.1 ± 4.6	6.67 ± 0.83	0.073 ± 0.011	1.07 ± 0.03
1.0	71.1 ± 2.5	16.9 ± 1.9	0.195 ± 0.022	1.15 ± 0.02
2.0	72.7 ± 2.3	30.3 ± 1.6	0.394 ± 0.023	1.30 ± 0.02
3.0	67.1 ± 2.3	41.8 ± 2.0	0.602 ± 0.036	1.44 ± 0.02
4.0	58.3 ± 3.9	43.7 ± 2.8	0.645 ± 0.058	1.44 ± 0.03
5.0	46.6 ± 3.8	46.6 ± 2.1	0.724 ± 0.048	1.54 ± 0.05

Table 6.7 Coefficients of the linear-quadratic model fit (\pm SE) for the fraction of BNC+MN, MN/BNC and MN/(BNC+MN) after irradiation of NIH/3T3 with 10 kV and 200 kV X-rays. Also shown are the coefficients of determination of the curves and the RBE_M values together with the SE.

Endpoint	α / Gy^{-1}	R^2	$RBE_M = \alpha / \alpha_{200\text{kV}}$
<i>BNC+MN</i>			
10 kV	16.86 ± 0.42	0.887	1.222 ± 0.045
200 kV	13.80 ± 0.38	0.993	
<i>MN / BNC</i>			
10 kV	0.2123 ± 0.0059	0.869	1.109 ± 0.044
200 kV	0.1914 ± 0.0055	0.993	
<i>MN / (BNC+MN)</i>			
10 kV	0.1537 ± 0.0085	0.628	1.097 ± 0.063
200 kV	0.1401 ± 0.0022	0.998	

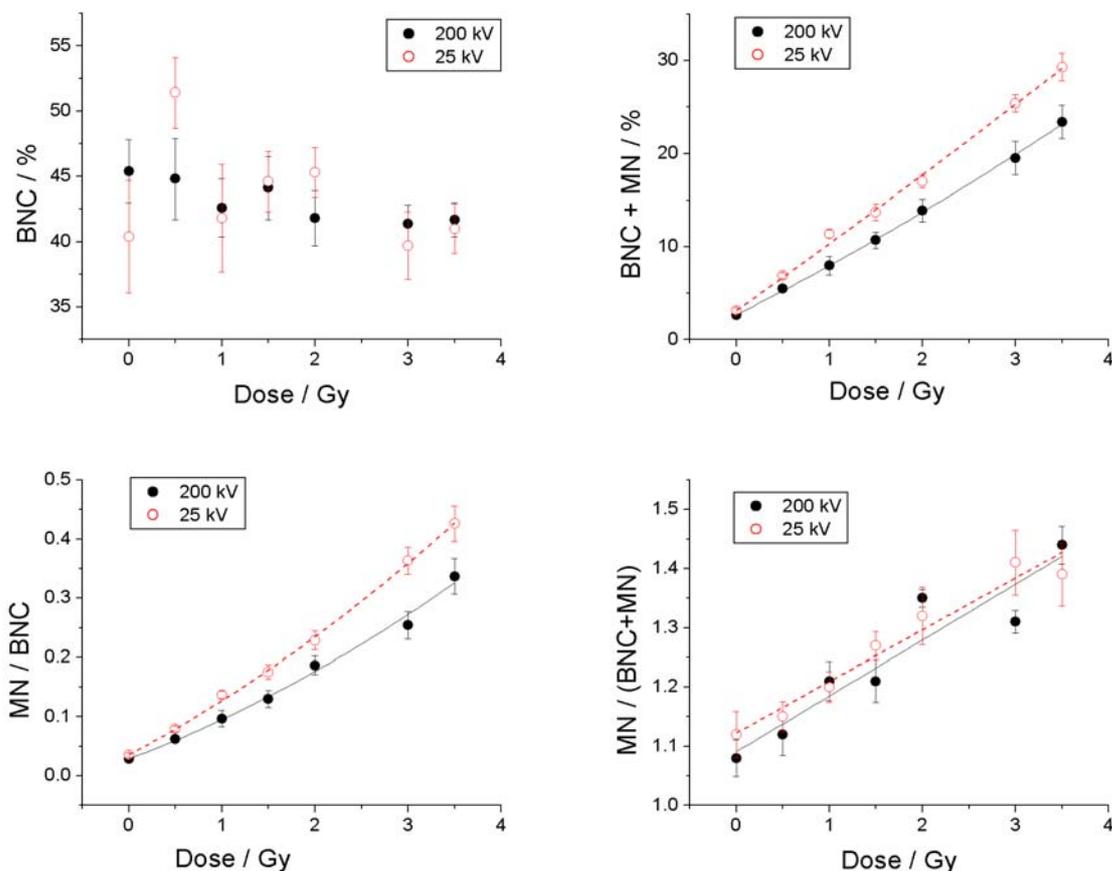


Fig. 6.10 Dose response of micronuclei induction after irradiation of MCF-12A cells with 25 kV X-rays (open circles, dashed lines) and 200 kV X-rays (closed circles, solid lines). The mean values and the SEM from 6 experiments are shown.

However, since the scatter of the dish thicknesses used in the irradiation turned out to be small (the same batch was used in one experiment), it is convenient to present the data by the corresponding means and SEM, together with the mean dose values and the corresponding dose SEM. These results are shown in Fig. 6.9 and Table 6.6. The data for the fraction of BNC+MN, MN/BNC and MN/(BNC+MN) were pooled and have been fitted by the least-squares fit to the linear-quadratic model (Eq. (6.6), where the β coefficient was set to 0). Since the application of higher doses resulted in saturation of response, the values after 4 and 5 Gy of 200 kV X-rays and 2.69 Gy of 10 kV X-rays were not included in the fit. Furthermore, the response at zero dose c (the background level of micronuclei induction) was fixed to the corresponding control value. The resulting linear dependence for both radiation qualities is shown in Fig. 6.9, and the fitting parameters with their SE are listed in Table 6.7. For the determination of RBE of 25 kV X-rays by irradiation of the MCF-12A cells, the mean value from 5 experiments for each radiation quality together with the SEM is presented in Table 6.8. The

Table 6.8 Dose dependence of the fraction of binucleated cells and micronuclei induction in MCF-12A after irradiation with 25 kV and 200 kV X-rays. The mean values from 5 experiments together with the SEM are presented.

Dose / Gy	BNC / %	BNC+MN / %	MN/BNC	MN/(BNC+MN)
<i>25 kV X-rays</i>				
0	40.4 ± 4.3	3.14 ± 0.30	0.0356 ± 0.0039	1.12 ± 0.04
0.5	51.4 ± 2.7	6.92 ± 0.30	0.0794 ± 0.0048	1.15 ± 0.02
1.0	41.8 ± 4.1	11.4 ± 0.41	0.137 ± 0.0064	1.20 ± 0.03
1.5	44.6 ± 2.3	13.7 ± 0.90	0.175 ± 0.012	1.27 ± 0.02
2.0	45.3 ± 1.9	17.0 ± 0.66	0.229 ± 0.016	1.32 ± 0.05
3.0	39.6 ± 2.6	25.4 ± 0.94	0.363 ± 0.023	1.41 ± 0.06
3.5	41.0 ± 1.9	29.3 ± 1.5	0.426 ± 0.030	1.39 ± 0.05
<i>200 kV X-rays</i>				
0	45.4 ± 2.4	2.67 ± 0.30	0.0289 ± 0.0036	1.08 ± 0.03
0.5	44.8 ± 3.1	5.47 ± 0.36	0.0619 ± 0.0052	1.12 ± 0.04
1.0	42.6 ± 2.2	7.97 ± 1.0	0.0969 ± 0.014	1.21 ± 0.03
1.5	44.1 ± 2.4	10.7 ± 0.87	0.130 ± 0.014	1.21 ± 0.04
2.0	41.8 ± 2.1	13.9 ± 1.2	0.187 ± 0.016	1.35 ± 0.02
3.0	41.4 ± 1.4	19.5 ± 1.8	0.254 ± 0.023	1.31 ± 0.02
3.5	41.7 ± 1.3	23.4 ± 1.8	0.337 ± 0.030	1.44 ± 0.03

irradiation was performed on the same passage parallelly for both radiation qualities. The dose dependences for the BNC+MN and MN/BNC have been fitted again to the linear-quadratic model of Eq. (6.6) using the least-squares method, where the response c at zero dose was fixed to the corresponding control value. For the fitting of the dose dependence of MN/(BNC+MN), the β -coefficient was fixed to 0, and the c parameter was left free. The resulting curves together with the mean values are presented in Fig. 6.10. The fitting coefficients together with their SE are shown in Table 6.9.

Table 6.9 Coefficients of the linear-quadratic model fit (\pm SE) for the fraction of BNC+MN, MN/BNC and MN/(BNC+MN) after irradiation of MCF-12A with 25 kV and 200 kV X-rays. Also shown are the coefficients of determination of the curves and the RBE_M values together with the SE.

Endpoint	α / Gy^{-1}	β / Gy^{-2}	R^2	$RBE_M = \alpha / \alpha_{200\text{kV}}$
<i>BNC+MN</i>				
25 kV	7.10 ± 0.43	0.10 ± 0.15	0.997	1.40 ± 0.10
200 kV	5.08 ± 0.18	0.221 ± 0.059	0.999	
<i>MN / BNC</i>				
25 kV	0.0836 ± 0.0041	0.0081 ± 0.0014	0.999	1.42 ± 0.20
200 kV	0.0587 ± 0.0078	0.0075 ± 0.0026	0.992	
<i>MN / (BNC+MN)</i>				
25 kV	0.0871 ± 0.0081	0*	0.889	0.92 ± 0.17
200 kV	0.094 ± 0.015	0*	0.958	

* the β coefficient was set to 0

6.4. Discussion

Recently, there has been initiated an ongoing discussion about the energy dependence of the relative biological effectiveness of X-rays. In order to draw definite conclusions, data for different cells and biological endpoints in wide X-ray ranges are necessary. Up to now, monochromatic X-ray sources are not easily available and the possibilities for extensive studies of RBE are limited. In the present study, one mouse fibroblast cell line and one human mammary epithelial cell line have been used. This allows to look for variability in response for the different cell types. The endpoints studied, clonogenic survival and micronuclei induction, represent two of the characteristic effects of ionising radiation in cells – clonogenic death and chromosomal damage. The sensitivity of both assays depends on the used dose range – for low doses, cell transformation is caused by re-arrangement of genetic material and cell death does not play a considerable role. In the higher dose range, the cell killing entirely superimposes the genetic effects.

The clonogenic assay results, presented in Tables 6.4 and 6.5, can be summarised in an RBE value of 10 kV and 25 kV X-rays in the range 1.1 - 1.3, where for both cell lines 10 kV X-rays are slightly more effective in cell kill. The uncertainties stated above are the SE, but in order to draw conclusions about the significance of the RBE value, confidence intervals have to be used. For the 95 % confidence interval, the standard errors have to be multiplied by 2. At the 10 % survival, this still results in an RBE significantly higher than 1 for both radiation qualities and cell lines, however, this is not the case in the entire studied survival range. From the presented survival level dependence of RBE (Fig. 6.8), the effectiveness of 10 kV X-rays is found to be significantly higher than 1 for surviving fractions in the range $0.03 \leq S \leq 0.6$, increasing with increasing survival, or, equivalently, decreasing dose (see Fig. 6.8, left). The effectiveness of 25 kV X-rays was found to be significantly higher than 1 for surviving fraction in the range $0.03 \leq S \leq 0.2$, but decreasing with increasing survival (see Fig. 6.8, right). Such dependence is rather unusual, since it shows an increase in the shoulder of the survival curve after irradiation with 25 kV X-rays. A complex dependence of the survival curve of mammalian cells in the low dose region has already been reported [Mar97] and shown to be a result of induced repair processes. For the survival of V79 after X-ray irradiation, an increased radiosensitivity in the very low dose range was found, followed by increased radioresistance in the dose range from 0.3 up to 1 Gy. From their LET dependence [Mar97], the low-dose hyperradiosensitivity and the increased radioresistance are expected to be stronger expressed for 25 kV than 10 kV X-rays, and most strongly expressed after 200 kV X-rays. However, the classical survival assay and the number of dose points in the low-dose range in the present work do not allow to prove this presumption in detail. As seen in the Fig. 6.8 for each soft X-ray radiation quality, the behaviour of the curves for the mouse and human cell lines is similar. The obtained survival dependence of RBE can lead to erroneous conclusions about the RBE values, if the results are extrapolated beyond the studied survival range. In the range of high survival (the low-dose region), the uncertainty becomes too large to draw any conclusions about the soft X-rays effectiveness for cell kill. In the high-dose range, an extrapolation is more reasonable, although, as already discussed, one should be aware of the possible artefacts present at high doses.

The micronucleus test results for the RBE of 10 kV X-rays for NIH/3T3, presented in Tables 6.6 and 6.7 and Fig. 6.9, can be summarised in an RBE_M value in the range 1.1 - 1.2. The uncertainty is again stated as SE, therefore, a factor 2 has to be taken into account for calculation of the confidence intervals. As a result, the effectiveness of 10 kV X-rays is found to be higher than 1 both for the fraction of damaged cells, expressed by the fraction of BNC+MN, as well as for quality of damage, shown by the numbers MN/BNC and MN/(BNC+MN). The increased effectiveness of the 10 kV X-rays is observed already in the fraction of BNC. In the low-dose range below about 1 Gy, a non-monotonic dependence of the BNC fraction on dose is observed, however, it is not significant for both radiation qualities. With increasing dose, the irradiation results in a cell cycle arrest, shown in a lower BNC fraction at the fixation point. Over the whole dose range, a linear correlation between the fraction of BNC and dose was found both after irradiation with 10 kV ($p = 0.028$) as well as after 200 kV X-rays, ($p = 0.0087$). For BNC+MN as well as for MN/BNC, a saturation of the effect was observed after

irradiation with doses above 2.5 Gy for both radiation qualities, possibly because of the lacking fraction of heavily damaged cells, delayed in the cell cycle arrest. This could also explain the RBE value close to 1.0 of the 10 kV X-rays for both endpoints, since the fraction of BNC at 2.7 Gy is about 25 % lower after irradiation with 10 kV than after irradiation with 200 kV. The RBE_M of 25 kV X-rays for the micronuclei induction in NIH/3T3 has been determined previously [Slo03]. Again, the higher effectiveness of soft X-rays was found to be expressed in the fraction of BNC, BNC+MN, MN/BNC and MN/(BNC+MN). Similarly, a stronger decrease in the BNC fraction was observed after irradiation with 25 kV than with 200 kV. For the BNC+MN fraction, as well as for MN/BNC and MN/(BNC+MN), an RBE_M value of 1.3 was determined. Following the assumed behaviour of the effectiveness with decreasing photon energy [Sas89, Kru04], a higher value is expected after irradiation with 10 kV X-rays.

The micronucleus test results for the RBE of 25 kV X-rays for MCF-12A are presented in Tables 6.8 and 6.9 and Fig. 6.10. Unlike for the NIH/3T3 cells, for MCF-12A the BNC fraction was found to depend on dose only after irradiation with 200 kV X-rays, where a linear correlation ($p = 0.011$) was found. After 25 kV X-ray irradiation, no significant correlation was found ($p > 0.05$). The BNC fraction for this cell line even in the non-irradiated cells was found to be generally small which could be a result of insufficient incubation time. However, prolongation of the incubation time lead to an increase in the fraction of 3- and 4-nucleated cells, and did not result in a higher BNC fraction. Since the BNC fraction even after irradiation with high doses was still above 40 %, the obtained values are assumed to reproduce well the radiation damage. For the fraction of BNC with MN as well as for the MN/BNC, an RBE_M value of about 1.4 was obtained, significantly higher than 1 also when the 95 % confidence interval is calculated. On the contrary, the RBE_M was found to be not significantly different from 1 when MN/(BNC+MN) was considered. This would mean, that the effectiveness of 25 kV X-rays results from the increase of number of damaged cells, which however do not have higher number of micronuclei. This was not the case for the effectiveness of 10 kV determined for NIH/3T3. The values obtained for the RBE of 25 kV X-rays for the fraction of damaged cells BNC+MN as well as for the severity of damage (MN/BNC) of about 1.4 is in good agreement with the previously published values for other cell lines [Slo03]. The determination of biological effectiveness of soft X-rays by 10 kV X-ray tube irradiation of the MCF-12A cell line would close the experiment series for the two cell lines in choice, however, it would not contribute to the resolving of the RBE energy dependence as much as an irradiation with a monochromatic source would do.

7 Summary

Soft X-rays have specific applications in the medical practice and radiobiology. Due to their strong absorption in the human body, they are useful in certain radiological procedures like mammography and in radiation therapy where positioning of the irradiation device close to the tumour is possible (e. g. superficial tumour irradiation, brachytherapy, photon activation therapy). Additionally, soft X-rays provide a tool for basic radiobiological studies, since a variation in the primary photon energy results in a variation in the secondary electron spectra. Thus the action of short-range secondary electrons, which contribute substantially to the dose delivered by high-energy photons as well, can be studied. Due to the high importance of soft X-rays in practice, their relative biological effectiveness has to be taken into account for risk estimation from radiological procedures as well as for treatment planning calculations. On the other hand, it is an useful tool for testing radiobiological models. However, RBE values depend on the photon energy, dose range, biological object and endpoint. Up to now, investigations have been performed mainly with polychromatic X-ray tubes and no systematic trends could be established. A monochromatic, tunable X-ray source in the soft X-ray region has many advantages in medicine and radiobiology. However, although several studies with synchrotron radiation in the soft X-ray range have been reported in the last years, there is no monochromatic tunable source available for routine use.

A source based on CR has the advantages of being quasi-monochromatic, tunable and self-collimated. In order to prove its feasibility for radiobiological studies, a project for determination of RBE of soft X-rays has been started at the ELBE accelerator of the Forschungszentrum Rossendorf. The purpose of this thesis was to investigate the requirements to such a source from the technical and radiobiological side. The characterisation of the source included calculations of the emitted photon energy and yield as well as spatial and spectral distribution at the target position. The calculated values were compared to the measured CR energy and yield and a reasonable agreement was found. In order to reduce the contribution of the bremsstrahlung background, monochromatisation was found to be necessary. A monochromator based on HOPG mosaic crystals was designed and manufactured, however the verification of the spatial and spectral distribution of CR intensity after monochromatisation has to be still performed. Furthermore, several methods for dose determination have been investigated at the CR source as well as at an X-ray tube at the Medical Faculty of the Dresden University of Technology. Absolute dose measurements using an ionisation chamber and spectral dose distribution determination using semiconductor detectors were performed. In addition, a dosimetrical system prototype based on TSEE detectors was tested due to its applicability in cases of inhomogeneous dose distribution. The detectors showed a good reproducibility of response and applicability in a variable dose range. Provided reproducible laboratory conditions, the TSEE system can be used for dose measurement in the case of inhomogeneous dose distributions as well as in a liquid environment. Further, the biological endpoints cell survival and micronucleus test were optimised for the practically relevant cell lines in choice. An irradiation system optimised for the requirements of the CR source and the biological endpoints was developed and constructed. In addition, the RBE of soft X-rays was determined by X-ray tube

irradiation. The RBE of 10 kV and 25 kV X-rays relative to 200 kV X-rays was determined for cell survival and micronuclei induction in mouse fibroblasts NIH/3T3 and human mammary epithelial cells MCF-12A. The RBE was found to be in the range from 1.0 to 1.4, depending on the used radiation quality, cell line and the biological endpoint. These results support the thesis that systematical studies of RBE depending on photon energy at the ELBE CR source are necessary and feasible.

8 Appendix

Models of cell response to ionising radiation

The oldest theory trying to explain the nonlinearity of the radiation effects was the target theory, introduced by Lea [Lea55]. Its basic assumptions are that (a) events of ionising radiation energy transfers are discrete and independent and (b) the observed effect occurs after a “hit” in the sensitive volume (target) within the object. A hit could be an ion couple creation, excitation to a certain energy level or an energy deposition above a certain level. The mean number of hits m in a volume V is linearly related to the volume and the dose D by the coefficient c :

$$m = cVD = \nu D \quad (\text{A.1})$$

The probability of having exactly n hits is described by the Poisson distribution:

$$P(n) = \frac{m^n e^{-m}}{n!} \quad (\text{A.2})$$

If at least n hits are needed to deactivate the target, the probability of getting less than n hits, or to survive, is, therefore, obtained by summing up the corresponding probabilities:

$$\frac{N}{N_0} = e^{-\nu D} \sum_{k=0}^{n-1} \frac{(\nu D)^k}{k!} \quad (\text{A.3})$$

If $n = 1$, the shape of the survival curve becomes exponential and, with increasing n , the shoulder of the curve becomes more pronounced. In a more general case, the number of targets necessary to inactivate can be also increased. However, the high number of free parameters has to be avoided to produce results of practical application. As most useful for description of mammalian cell survival curves, the single-hit multitarget model has been proved. The predicted survival curve has a shoulder at low doses and is exactly exponential at high doses.

However, the most widely used model is based on the theory of dual radiation action (TDRA) of Kellerer and Rossi. The base of the theory lies on the experimental fact that for many observed effects the dose dependence is quadratic for low LET-radiations, whereas it is linear for high LET radiation. The basic assumption is that the ionising radiation produces sublesions within the cells and the biological effect is observed only if two sublesions combine (this happens with a constant probability). The first formulation of the theory is the site model [Kel72], where a restriction of the interaction distance between the sublesions was postulated. The basic concepts come from the microdosimetric energy deposition model. The specific energy z is defined as the energy imparted to the matter of mass m , and according to the site model, the number of lesions ε in the site is proportional to the square of z :

$$\varepsilon(z) = cz^2 \quad (\text{A.4})$$

Thus, the average number of lesions is

$$\bar{\varepsilon}(z) = cz^2 \quad (\text{A.5})$$

where $\overline{z^2}$ is the expectation value of z^2 for a given dose D . It can be presented in terms of single-event spectra as

$$\mathcal{E}(z) = c(z_D D + D^2) \quad (\text{A.6})$$

where D is the absorbed dose and z_D is the dose average of the specific energy. This relationship can be split into a term of linear dose dependence of the effect (one-track action) with a proportionality coefficient α and a quadratic dependence (two-track action) with a proportionality coefficient β :

$$\mathcal{E} = \alpha D + \beta D^2 + c \quad (\text{A.7})$$

This model was validated in some cases, as e.g. for the slope of the dose dependence of RBE and for the LET dependence of the number of lethal events per track for slow heavy ions. The site model of the TDRA has been widely popular until results of correlated ion irradiation and ultrasoft X-rays experiments came to a contradiction with it [Goo82]. Unlike the predictions of the theory, the effect of spatial correlation of lesions was very small at distances larger than about 0.1 μm . The biological effectiveness of ultrasoft X-rays turned out to be higher than expected and the resulting dose-effect curves were lacking a quadratic component unlike predicted by the theory, although, due to their low-energy, the secondary electrons of such X-rays in tissue have track lengths limited to some tens of nm. In order to account for the structure in which sublesions are formed, as well as to incorporate the geometrical distributions of sublesions, the theory has been developed into the distance model [Kel78], which however requires either difficult to obtain experimental data on the nanometer scale or complex mathematical simulations and is not useful in practice. Another group of models is concentrated on the radiochemical and biological processing of radiation damage in the cell. The threshold-energy repair-saturation model [Goo82] is based on the biological modification of the primary lesions. It does not require an interaction between the lesions and assumes the curvature of the dose-effect relationships to be entirely a repair effect. In the repair-misrepair model of [Tob80], the various possible radiation outcomes such as mutation, lethality or survival as well as their time development are taken into account. Although the model well describes the survival curve, additional assumptions about the repair kinetics have to be made. The lethal-potentially lethal model of Curtis [Cur86] considers the possibility of interaction of the primary lesions as well as the dose rate dependence. Although all these models allow to consider the specific irradiation conditions, cell cycle and repair kinetics, the high number of free parameters makes the survival curve difficult to interpret. Moreover, almost all models can be simplified to the same formulation of single-hit effect, and the low-dose approximation often is similar to the linear-quadratic model. The wide use of the linear-quadratic model is due to the fact that the survival curves for mammalian cell lines have mostly an increasing slope. From here, a simple relation can be established. A linear dose dependence of the slope in the semi-logarithmic scale is mostly enough, thus the survival curve is described by the linear-quadratic model:

$$S = \exp(-\alpha D - \beta D^2) \quad (\text{A.8})$$

Although the theoretical explanation of this model in the sight of the TDRA have been proved to be wrong, it is still the most widely used in the practice.

9 References

- [And77] J. U. Andersen, S. K. Andersen, W. M. Augustyniak (1977) Channeling of electrons and positrons – correspondence between classical and quantal descriptions. *Mat. Fys. Medd. Dan. Vid. Selsk.* 39(10): 1-58
- [And83] J. U. Andersen, E. Bonderup, E. Laegsgaard, A. H. Sorensen (1983) Incoherent scattering of electrons and linewidth of planar-channeling radiation. *Phys. Scripta* 28(3): 308-330
- [And83a] J. U. Andersen, E. Bonderup, R. H. Pantell (1983) Channeling radiation. *Ann. Rev. Nucl. Part. Sci.* 33: 453-504
- [And85] J. U. Andersen, E. Bonderup, E. Laegsgaard (1985) Channeling radiation – quantum theory. In: A. W. Saenz and H. Überall (eds.) *Coherent radiation sources*, Springer Verlag, New York
- [Bay01] S. Bayat, G. Le Duc, L. Porra, G. Berruyer, C. Nemoz, S. Monfraix, S. Fiedler, W. Thomlinson, P. Suortti, C. G. Standertskjold-Nordenstam, A. R. Sovijarvi (2001) Quantitative functional lung imaging with synchrotron radiation using inhaled xenon as contrast agent. *Phys. Med. Biol.* 46(12): 3287-3299
- [Bec95] B. Beckhoff (1995) X-ray focusing with strongly curved HOPG crystals in the energy-dispersive X-ray fluorescence analysis. PhD thesis, University of Bremen, signature DS 1732
- [Bel78] V. V. Beloshitsky, M. A. Kumakhov (1978) Quantum theory of spontaneous and stimulated emission of channeled electrons and positrons. *Zh. Eksp. Teor. Fiz.* 74(4): 1244-1256
- [Bis86] M. Bistrotić, M. Bišćan, T. Viculin (1986) RBE of 20 kV X-rays determined for survival of V 79 cells. *Radiother. Oncol.* 7: 175-180
- [Boo94] J. M. Boone, J. A. Seibert (1994) A comparison of mono- and poly-energetic x-ray beam performance for radiographic and fluoroscopic imaging. *Med. Phys.* 21(12): 1853-1863
- [Boo97] J. M. Boone, J. A. Seibert (1997) An accurate method for computer-generating tungsten anode x-ray spectra from 30 to 140 kV. *Med. Phys.* 24 (11): 1661-1670
- [Bre02] D. J. Brenner, S. G. Sawant, M. P. Hande, R. C. Miller, C. D. Elliston, Z. Fu, G. Randers-Pehrson, S. A. Marino (2002) Routine screening mammography: how important is the radiation-risk side of the benefit-risk equation? *Int. J. Radiat. Biol.* 78: 1065-1067
- [Bur57] P. R. J. Burch (1957) Calculations of energy dissipation characteristics in water for various radiations. *Radiat. Res.* 6: 289-301

- [Bur95] E. Burattini, E. Cossu, C. Di Maggio, M. Gambaccini, P. L. Indovina, M. Marziani, M. Pocek, S. Simeoni, G. Simonetti (1995) Mammography with synchrotron radiation. *Radiology* 195(1): 239-244
- [Car90] F. E. Carroll, J. W. Waters, R. R. Price, C. A. Brau, C. F. Roos, N. H. Tolk, D. R. Pickens, W. H. Stephens (1990) Near-monochromatic X-ray beams produced by the free electron laser and Compton backscatter. *Invest. Radiol.* 25(5): 465-471
- [Cho99] K. Chouffani, H. Überall (1999) Theory of low energy channeling radiation: application to a germanium crystal. *Phys. Stat. Sol. B* 213(1): 107-151
- [Cra72] K. W. Crase, K. Becker, R. B. Gammage (1972) High dose-level response of ceramic BeO. *Health Phys.* 22(4): 402
- [Cre03] P. Crespo, J. Pawelke, W. Enghardt (2003) A CAMAC data acquisition system for multi parameter measurements. *Wiss.-Tech. Ber. FZR-372*: 82
- [Cur86] S. B. Curtis (1986) Lethal and potentially lethal lesions induced by radiation – a unified repair model. *Radiat. Res.* 106: 252-271
- [DFG99] Deutsche Forschungsgemeinschaft, grant number Do 429/4-1 (1999)
- [Dör92] B. Dörschel, V. Schuricht, J. Steuer (1992) *Praktische Strahlenschutzphysik*. Spektrum Akademischer Verlag Heidelberg-Berlin-New York
- [Dur91] J. S. Durham, S. E. Merwin, K. L. Swinth (1991) Skin dose evaluations using exoelectron dosimeters. *Radiat. Prot. Dosim.* 39(1/3): 67-70
- [Dys55] F. J. Dyson, H. Überall (1955) Anisotropy of bremsstrahlung and pair production in single crystals. *Phys. Rev.* 99: 604-605
- [Eic83] H. Eichenmüller (1983) Thermally stimulated exoelectron emission (TSEE) from metal and semiconductor surfaces. *Radiat. Prot. Dosim.* 4(3/4): 281-285
- [Ell00] H. Elleaume, S. Fiedler, F. Esteve, B. Bertrand, A. M. Charvet, P. Berkvens, G. Berruyer, T. Brochard, G. Le Duc, C. Nemoz, M. Renier, P. Suortti, W. Thomlinson, J. F. Le Bas (2000) First human transvenous coronary angiography at the European Synchrotron Radiation Facility. *Phys. Med. Biol.* 45(9): L39-L43
- [Eng03] W. Enghardt, W. Neubert, J. Pawelke, W. Wagner (2003) Radiation shielding of the beam dump of the radiation physics beamline. *Wiss.-Tech. Ber. FZR-375*: 27
- [Fen85] M. Fenech, A. A. Morley (1985) Measurement of micronuclei in lymphocytes. *Mutat. Res.* 147(1-2): 29-36
- [Fen93] M. Fenech (1993) The cytokinesis-block micronucleus technique: a detailed description of the method and its application to genotoxicity studies in human populations. *Mutat. Res.* 285(1): 35-44

- [Fra02] M. Frankenberg-Schwager, I. Garg, D. Frankenberg, B. Greve, E. Severin, D. Uthe, W. Göhde (2002) Mutagenicity of low-filtered 30 kVp X-rays, mammography X-rays and conventional X-rays in cultured mammalian cells. *Int. J. Radiat. Biol.* 78(9): 781-789
- [Fri59] O. R. Frisch, D. N. Olson (1959) Detection of coherent bremsstrahlung from crystals. *Phys. Rev. Letters* 3: 141
- [Gab00] F. Gabriel, P. Gippner, E. Grosse, D. Janssen, P. Michel, H. Prade, A. Schamlott, W. Seidel, A. Wolf, R. Wunsch and the ELBE-crew (2000) The Rossendorf radiation source ELBE and its FEL projects. *Nucl. Instrum. Meth. B* 161-163: 1143-1147
- [Gam95] M. Gambaccini, A. Taibi, A. Del Guerra, F. Frontera, M. Marziani (1995) Narrow energy band X-rays via mosaic crystal for mammography application. *Nucl. Instrum. Meth. A* 365: 248-254
- [Gar90] C. K. Gary, A. S. Fisher, R. H. Pantell, J. Harris, M. A. Piestrup (1990) Channeling of electrons in Si produces intense quasimonochromatic, tunable, picosecond x-ray bursts. *Phys. Rev.* 42(1): 7-14
- [Gar91] C. K. Gary, R. H. Pantell, M. Ozcan, M. A. Piestrup, D. G. Boyers (1991) Optimization of the channeling radiation source crystal to produce intense quasimonochromatic x rays. *J. Appl. Phys.* 70(6): 2995-3002
- [Gar93] C. K. Gary, M. A. Piestrup, D. G. Boyers, C. I. Pincus, R. H. Pantell, G. B. Rothbart (1993) Noninvasive digital energy subtraction angiography with channeling-radiation x-ray source. *Med. Phys.* 20(5): 1527-1535
- [Gen96] H. Genz, L. Groening, P. Hoffmann-Stascheck, A. Richter, M. Höfer, J. Hormes, U. Nething, J. P. F. Sellschop, C. Töpffer, M. Weber (1996) Channeling radiation of electrons in natural diamond crystals and their coherence and occupation lengths. *Phys. Rev. B* 53(14): 8922-8936
- [Goo77] D. T. Goodhead, J. Thacker (1977) Inactivation and mutation of cultured mammalian cells by aluminium characteristic ultra-soft X-rays. I. Properties of aluminium X-rays and preliminary experiments with Chinese hamster cells. *Int. J. Radiat. Biol.* 31: 541-559
- [Goo82] D. T. Goodhead (1982) An assessment of the role of microdosimetry in radiobiology. *Radiat. Res.* 91 (1): 45-76
- [Goo94] D. T. Goodhead (1994) Soft X-ray radiobiology and synchrotron radiation. In: B. Chance, J. Deisenhofer, E. Ebashi, D. T. Goodhead, J. R. Helliwell, H. E. Huxley, T. Iizuka, J. Kirz, T. Mitsui, G. Zaccari (eds.) *Synchrotron Radiation in the Biosciences*, Oxford University Press, New York: 683-705

- [Gou82] M. Gouanere, D. Sillou, M. Spighel, N. Cue, M. J. Gaillard, R. G. Kirsch, J.-C. Poizat, J. Remillieux, B. L. Berman, P. Catillon, L. Roussel, G. M. Temmer (1982) Sharp-line and broad-continuum radiation from electrons channelled in diamond. *Nucl. Instrum. Meth.* 194: 225-228
- [Gou88] M. Gouanere, D. Sillou, M. Spighel, N. Cue, M. J. Gaillard, R. G. Kirsch, J.-C. Poizat, J. Remillieux, B. L. Berman, P. Catillon, L. Roussel, G. M. Temmer (1988) Planar channeling radiation from 54 – 110-MeV electrons in diamond and silicon. *Phys. Rev. B* 38: 4352–4371
- [Hil98a] C. K. Hill, B. E. Nelms, J. F. MacKay, D. W. Pearson, W. S. Kennan, T. R. Mackie, P. M. DeLuca Jr., M. J. Lindstrom, M. N. Gould (1998) Synchrotron-produced ultrasoft X rays: equivalent cell survival at the isoattenuating energies 273 eV and 860 eV. *Radiat. Res.* 150(5): 513-520
- [Hil98b] M. A. Hill, M. D. Vecchia, K. M. S. Townsend, D. T. Goodhead (1998) Production of copper L ultrasoft X-rays for biological and biochemical investigations. *Phys. Med. Biol.* 43: 351-363
- [Hol68] G. Holzapfel (1968) Zur Exoelektronen-Emission (Kramer-Effekt) von Berylliumoxid. Doktorarbeit, Fakultät für Allgemeine Ingenieurwissenschaften, TU Berlin, signature D83
- [Hol69] G. Holzapfel (1969) Analysis of exoelectron glow curves. *Phys. Stat. Sol.* 33: 235
- [Hol03] G. Holzapfel (2003) private communication
- [Hos88] M. Hoshi, S. Antoku, N. Nakamura, W. J. Russel, R. C. Miller, S. Sawada, M. Mizuno, S. Nishio (1988) Soft X-rays dosimetry and RBE for survival of Chinese hamster V79 cells. *Int. J. Radiat. Biol.* 54: 577-591
- [Hub99] J. H. Hubbell (1999) Review of photon interaction cross section data in the medical and biological context. *Phys. Med. Biol.* 44(1): R1-R22
- [ICR91] ICRP Publication 60. The 1990 recommendations of the International Commission on Radiological Protection (1991). *Annals of the ICRP* 21(1-3), Pergamon Press, Oxford
- [Ing98] V. N. Ingal, E. A. Beliaevskaya, A. P. Brianskaya, R. D. Merkurieva (1998) Phase mammography - a new technique for breast investigation. *Phys. Med. Biol.* 43(9): 2555-2567
- [Jac83] J. D. Jackson (1983) *Klassische Elektrodynamik*. Walter de Gruyter, Berlin-NewYork
- [Jai69] J. L. Jainchill, S. A. Aaronson, G. J. Todaro (1969) Murine sarcoma and leukemia viruses: assay using clonal lines of contact-inhibited mouse cells. *J. Virol.* 4(5): 549-553
- [Jen81] R. J. Jennings, R. J. Eastgate, M. P. Siedband, D. L. Ergun (1981) Optimal x-ray spectra for screen-film mammography. *Med. Phys.* 8(5): 629-639

- [Kel02] A. M. Kellerer (2002) Electron Spectra and the RBE of X Rays. *Radiat. Res.* 158(1): 13-22
- [Kel72] A. M. Kellerer, H. H. Rossi (1972) The theory of dual radiation action. *Curr. Top. Radiat. Res. Q.* 8: 85-158
- [Kel78] A. M. Kellerer, H. H. Rossi (1978) A generalized formulation of dual radiation action. *Radiat. Res.* 75: 471-488
- [Kep89] J. O. Kephart, R. H. Pantell, B. L. Berman, S. Datz, H. Park, R. K. Klein (1989) Measurement of the occupation lengths of channeled 17-MeV electrons and 54-MeV electrons and positrons in silicon by means of channeling radiation. *Phys. Rev. B* 40(7): 4249-4263
- [Kin95] Kinetic models of thermoluminescence (Tutorial, 1995) *Radiat. Prot. Dosim.* 60: 5-12
- [Kle85] R. K. Klein, J. O. Kephart, R. H. Pantell, H. Park, B. L. Berman, R. L. Svent, S. Datz, R. W. Fearick (1985) Electron channeling radiation from diamond. *Phys. Rev. B* 31(1): 68-92
- [Knu94] W. Knüpfer (1994) Feasibility study of a channeling radiation source for applications in the X-ray region. *Nucl. Instrum. Meth. in Phys. Res. B* 87: 98-103
- [Kra66] J. Kramer (1966) Exoelektronen-Dosimeter für Röntgen- und Gammastrahlen. *Z. Angew. Phys.* 20: 411-417
- [Kri86] W. Kriegseis, M. Petel, A. Scharmann, C. Wieters (1986) Potentials of TSEE for beta ray dosimetry. *Radiat. Prot. Dosim.* 14(2): 151-155
- [Kri93] W. Kriegseis, K. Rauber, A. Scharmann, K.-H. Ritzenhoff, J. L. Chartier, D. Cutarella, C. Itie, M. Petel (1993) Dependence of the TSEE response of BeO thin films on photon energy and composition of cover materials. *Radiat. Prot. Dosim.* 47(1/4): 143-146
- [Kru04] M. Krumrey, G. Ulm, E. Schmid (2004) Dicentric chromosomes in monolayers of human lymphocytes produced by monochromatized synchrotron radiation with photon energies from 1.83 keV to 17.4 keV. *Radiat. Environ. Biophys.* 43(1): 1-6, Epub Apr. 03, 2004
- [Kum89] M. A. Kumakhov, F. F. Komarov (1989) Radiation from charged particles in solids. American Institute of Physics Translation Series, New York
- [Lar01] C. M. de Lara, M. A. Hill, T. J. Jenner, D. Papworth, P. O'Neil (2001) Dependence of the yield of DNA double-strand breaks in Chinese hamster V79-4 cells on the photon energy of ultrasoft X-rays. *Radiat. Res.* 155: 440-448
- [Lea55] D. E. Lea (1955) Actions of radiation on living cells, 2nd ed. Cambridge Univ. Press, New York
- [Les85] J. Lesz, A. Scharmann, G. Holzapfel (1985) Connected TSEE/OSEE readouts of BeO thin-film detector. *Jpn. J. Appl. Phys.* 24(Suppl. 24-4): 259-261

- [Lin65] J. Lindhard (1965) Influence of crystal lattice on motion of energetic charged particles. *Mat. Fys. Medd. Dan. Vid. Selsk.* 34(14): 1-64
- [Mar90] M. J. Marchese, P. E. Goldhagen, M. Zaider, D. J. Brenner, E. J. Hall (1990) The relative biological effectiveness of photon radiation from encapsulated iodine-125, assessed in cells of human origin: I. Normal diploid fibroblasts. *Int. J. Radiat. Oncol. Biol. Phys.* 18(6): 1407-1413
- [Mar97] B. Marples, P. Lambin, K. A. Skov, M. C. Joiner (1997) Low dose hyper-radiosensitivity and increased radioresistance in mammalian cells. *Int. J. Radiat. Biol.* 71(6): 721-735
- [Mic96] V. Michalik, D. Frankenberg (1996) Two types of double-strand breaks in electron and photon tracks and their relation to exchange-type chromosome aberrations. *Radiat. Environ. Biophys.* 35(3): 163-169
- [Mik04] T. Mikuletz (2004) Dosimetrische Charakterisierung einer für strahlenbiologische Experimente als Referenzstrahlungsquelle dienenden Röntgenanlage. Diplomarbeit, Hochschule Mittweida
- [Nau02] B. Naumann (2002) Calculation of dose rate source terms around the beam dump vessel. *Wiss.-Tech. Ber. FZR-341*: 25
- [Nei89] F. O'Neil, I. C. E. Turcu, G. J. Tallents, J. Dickerson, T. Lindsay, D. T. Goodhead, A. Stretch, C. W. Wahrton, R. A. Meldrum (1989) A repetitive laser-plasma X-ray source for radiobiology research. *Photo-opt. Instrum. Eng.* 1140: 232-236
- [Nel87] R. S. Nelson, R. D. Zach, E. Ziegler, P. J. Papin, Z. L. Barbaric, A. R. Ricci, L. W. Basset (1987) Radiographic imaging using multilayer mirrors. *Proc. SPIE* 767: 116-121
- [Neu01] W. Neubert, W. Enghardt, U. Lehnert, E. Müller, B. Naumann, A. Panteleeva, J. Pawelke (2001) Optimization of a tunable quasi-monochromatic X-ray source for cell irradiations. In: A. Kling, F. Barao, M. Nakagawa, L. Tavora, P. Vaz (eds.) *Proceedings of the Int. Conf. on Advanced Monte Carlo for Radiation Physics, Particle Transport Simulation and Applications*, Lisbon, Oct. 23-26, Springer Verlag Berlin-Heidelberg-New-York: 123-128
- [Nik87] H. Nikjoo, D. T. Goodhead (1987) Physical and biological consequences of high- and low-LET radiations in biological targets. In: E. M. Fielden, J. F. Fowler, J. H. Hendry and D. Scott (eds.) *Proceedings of the Eighth International Congress in Radiation Research*, Vol. 1, Taylor and Francis, London: 80
- [Nik91] H. Nikjoo, D.T. Goodhead (1991) Track structure analysis illustrating the prominent role of low-energy electrons in radiobiological effects of low-LET radiations. *Phys. Med. Biol.* 36(2): 229-238

- [Nis98] NIST Physical Reference Data (1998) X-ray and Gamma-Ray Data
<http://physics.nist.gov/PhysRefData/>
- [Pai92] T. M. Paine, H. D. Soule, R. J. Pauley, P. J. Dawson (1992) Characterization of epithelial phenotypes in mortal and immortal human breast cells. *Int. J. Cancer* 50(3): 463-473
- [Pan03] A. Panteleeva, D. Slonina, K. Brankovic, K. Spekl, J. Pawelke, C. Hoinkis, W. Dörr (2003) Clonogenic survival of human keratinocytes and rodent fibroblasts after irradiation with 25 kV x-rays. *Radiat. Environ. Biophys.* 42(2): 95-100, Epub Jun. 26, 2003
- [Pin84] M. Pincu, D. Bass, A. Norman (1984) An improved micronuclear assay in lymphocytes. *Mutat. Res.* 139(2): 61-5.
- [Pis00] E. D. Pisano, R. E. Johnston, D. Chapman, J. Geradts, M. V. Iacocca, C. A. Livasy, D. B. Washburn, D. E. Sayers, Z. Zhong, M. Z. Kiss, W. C. Thomlinson (2000) Human breast cancer specimens: diffraction-enhanced imaging with histologic correlation - improved conspicuity of lesion detail compared with digital radiography. *Radiology* 214(3): 895-901
- [Puc56] T. T. Puck, P. I. Marcus (1956) Action of X-rays on mammalian cells. *J. Exp. Med.* 103: 653-666
- [Reg83] D. F. Regulla, U. Leischner (1983) Comparing interface dosimetry with conventional methods and TSEE. *Radiat. Prot. Dosim.* 4(3/4): 174-176
- [Rei99] I. Reitz (1999) Untersuchung von Channelingstrahlung an Diamant am S-DALINAC bei einer Elektronenenergie von 9 und 10 MeV. Diplomarbeit, TU Darmstadt
- [Rio03] M. S. del Rio and R. J. Dejus (2003) XOP 2.0 Software Package
<http://www.esrf.fr/computing/expg/subgroups/theory/idl/xop/xop.html>
- [Rob62] M. T. Robinson (1962) Deduction of ion ranges in solids from collection experiments. *Appl. Phys. Lett.* 1(2): 49-51
- [Ros99] L. A. R. da Rosa, M. Seidenbusch, D. F. Regulla (1999) Dose profile assessment at gold-tissue interfaces by using TSEE. *Radiat. Prot. Dosim.* 85(1-4): 433-436
- [Sas89] M. S. Sasaki, K. Kobayashi, K. Hieda, T. Yamada, Y. Ejima, H. Maezawa, Y. Furusawa, T. Ito, S. Okada (1989) Induction of chromosome aberrations in human lymphocytes by monochromatic X-rays of quantum energy between 4.8 and 14.6 keV. *Int. J. Radiat. Biol.* 56: 975-988
- [Slo03] D. Slonina, K. Spekl, A. Panteleeva, K. Brankovic, C. Hoinkis, W. Dörr (2003) Induction of micronuclei in human fibroblasts and keratinocytes by 25 kV x-rays. *Radiat. Environ. Biophys.* 2003 42(1):55-61, Epub Feb. 25, 2003

- [Spa92] I. Spadinger, B. Palcic (1992) The relative biological effectiveness of ^{60}Co γ -rays, 55 kVp X-rays, 250 kVp X-rays, and 11 MeV electrons at low doses. *Int. J. Radiat. Biol.* 61: 345-353
- [Sta12] J. Stark (1912) Zerstreung und Absorption von β -Strahlen und Röntgenstrahlen. *Physik. Zeitschr.* 13: 973
- [Sun99] C. M. Sunta, W. E. Feria Ayta, R. N. Kulkarni, T. M. Piters, S. Watanabe (1999) Theoretical models of thermoluminescence and their relevance in experimental work. *Radiat. Prot. Dosim.* 84(1-4): 25-28
- [Tob80] C. A. Tobias, E. A. Blakeley, F. Q. Ngo, T. C. H. Yang (1980) The repair-misrepair model of cell survival. In: R. E. Meyn and H. R. Withers (eds.) *Radiation Biology and Cancer Research*, Raven Press, New York: 195-230
- [Übe56] H. Überall (1956) High-energy interference effect of bremsstrahlung and pair production in crystals. *Phys. Rev.* 103(4): 1055-1067
- [Ugg66] E. Uggerhøj (1966) Orientation dependence of the emission of positrons and electrons from ^{64}Cu embedded in single crystals. *Phys. Lett.* 22: 382-383
- [Ven01] R. Ventura, T. Dill, W. R. Dix, M. Lohmann, H. Job, W. Kupper, R. Fattori, C. A. Nienaber, C. W. Hamm, T. Meinertz (2001) Intravenous coronary angiography using synchrotron radiation: technical description and preliminary results. *Ital. Heart J.* 2(4): 306-311
- [Ver94] F. Verhaegen, A. Vral (1994) Sensitivity of micronucleus induction in human lymphocytes to low-LET radiation qualities: RBE and correlation of RBE and LET. *Radiat. Res.* 139: 208-213
- [Vir77] R. P. Virsik, D. Harder, I. Hansmann (1977) The RBE of 30 kV x-rays for the induction of dicentric chromosomes in human lymphocytes. *Radiat. Environ. Biophys.* 14: 109-121
- [Wed86] R. Wedell (1986) Theory of Kumakhov radiation. *Radiat. Eff.* 91: 167-178
- [Wol00] Wolfram Research (2000) Mathematica 4.1. <http://www.wolfram.com/>
- [Yaf97] M. J. Yaffe, J. A. Rowlands (1997) X-ray detectors for digital radiography. *Phys. Med. Biol.* 42(1): 1-39
- [Zei77] L. Zeitz, S. H. Kim, J. H. Kim, J. F. Detko (1977) Determination of Relative Biological Effectiveness (RBE) of soft X Rays. *Radiat. Res.* 70: 552-563

10 Table of Abbreviations

ATCC	American Type Culture Collection
BNC	binucleated cell
CAMAC	computer automated measurement and control
CI	confidence interval
CR	channelling radiation
DMEM	Dulbecco's modified Eagle's medium
DNA	deoxyribonucleic acid
dsb	double-strand breaks
EDTA	ethylenediaminetetraacetic acid
ELBE	electron linear accelerator of high brilliance and low emittance
FEL	free electron laser
FOD	foc lus to obj ect dist ance
FWHM	full width at half maximum
HEPES	4-(2- hydroxyethyl)-1- Piperazineethanesulfonic acid
HOPG	highly oriented pyrolytic graphite
ICRP	I nternational C ommission on R adiological P rotection
LET	linear energy transfer
MCA	multichannel analyser
MN	micronucleus
NIH	N ational I nstitutes of H ealth, a part of the U.S. Department of Health and Human Services
NIST	N ational I nstitute of S tandards and T echnology within the U. S. Commerce Department's Technology Administration
OTR	optical transition radiation
PBS	phosphate buffered saline
PE	plating efficiency
PMMA	polymethyl methacrylate
ppm	parts per million
RBE	relative biological effectiveness
RBE _M	maximum RBE
RP	radiation physics
SE	standard error
SEM	standard error of the mean
SF2	surviving fraction at 2 Gy
TDRA	theory of dual radiation action

TL	thermoluminescence, thermoluminescent
TLD	thermoluminescent detector
TSEE	thermally stimulated exoelectron emission

Acknowledgements

It is a pleasure for me to thank the many people who made this thesis possible.

I would like to thank the late Prof. Birgit Dörschel for giving me the opportunity to work on this thesis, which was performed in the Institute of Nuclear and Hadron Physics under the leadership of Prof. Eckart Grosse.

I am very thankful to Dr. Wolfgang Enhardt for proposing me this interesting topic and for the helpful support during all the time. Under the supervision of Dr. Jörg Pawelke I have learned how to organize this puzzle of many different subjects and to combine the activities of a physicist with the work in a cell laboratory. My thank to Dr. Harald Prade is for his inspiration and foundation of the channelling experiments at ELBE. I would like to thank Prof. Wolfgang Dörr for the opportunity to perform the radiobiological experiments in the Radiobiology Laboratory of the Medical Faculty of the Dresden University of Technology, for the helpful discussions and advices.

Toward understanding the channelling process, I received a lot of help from Dr. Ulf Lehnert. I would like to thank Dr. Jörg Pawelke and Dr. Wolfgang Wagner for performing the experimental work on channeling radiation. In the last part of my work, I had the pleasure to discuss these topics with Behnam Azadegan as well. For their support in the field of X-ray optics I would like to thank Dr. Burkhard Beckhoff and Dr. Birgit Kanngießer.

Elisabeth Leßmann I would like to thank for the unquestioned support in the radiobiological experiments, as well as for the readiness to understand, learn and practice the new techniques. The colleagues from the PET-group – Paulo Crespo, Fine Fiedler, Uwe Reichelt, Katia Parodi, Jenny Philipp, Falk Pönisch – which went with me through these years, I would like to thank for the nice atmosphere during and outside work.

I would like to thank my first teacher in the unpredictable field of cell culture at the Radiobiology Laboratory, Dr. Annegret Dörfler. For the valuable advices and the wonderful collaboration I would like to express my gratitude to Dr. Dorota Slonina. In addition, I would like to thank Dr. Katarina Brankovic, Cordelia Hoinkis, Stefan Pieck, Kathrin Spekl, and all the other colleagues at the Radiotherapy Department of the Medical Faculty for the nice work and discussions on biological, physical and other topics.

Manfred Sobiella I would like to thank for giving helpful ideas and assistance for the construction of the HOPG monochromator as well as the iron collimator. I would like to thank the FZR workshop for producing the devices necessary for the experiments.

And in the end I would like to thank all who were beside me in these years. I think I would not be able to come so far without Aneta, Chrisitna, Dancho, Dimitar, Holger, Jörg, Lisa and all the others which were supporting me and giving power. I am grateful to my parents and my sister for believing in me and accepting my decisions. And, of course, to Ulf, whom I owe so much.

Versicherung

Hiermit versichere ich, dass ich die vorliegende Arbeit ohne unzulässige Hilfe Dritter und ohne Benutzung anderer als der angegebenen Hilfsmittel angefertigt habe; die aus fremden Quellen direkt oder indirekt übernommenen Gedanken sind als solche kenntlich gemacht. Die Arbeit wurde bisher weder in Inland noch im Ausland in gleicher oder ähnlicher Form einer anderen Prüfungsbehörde vorgelegt.

Dresden, den 10.02.2005

Erklärung

Die vorliegende Arbeit wurde am Institut für Kern- und Hadronenphysik des Forschungszentrum Rossendorf e. V. (FZR) angefertigt. Die wissenschaftliche Betreuung erfolgte durch Herrn Prof. Dr. E. Grosse seitens der Fachrichtung Physik der Technischen Universität Dresden und durch Herrn Dr. rer. nat. W. Enghardt seitens der Abteilung Strahlungsphysik des Institutes für Kern- und Hadronenphysik des FZR.

Die Promotionsordnung der Fakultät für Mathematik und Naturwissenschaften der Technischen Universität Dresden wird von mir anerkannt.

Dresden, den 10.02.2005